University of Stavanger

Faculty of Science and Technology

MASTER OF SCIENCE THESIS

Study Program/ Specialization: Petroleum Engineering-Petroleum Geology	Spring Semester, 2011 Open
Author: **Yaser Mirzaahmadian**	 (Signature Author)

Faculty Supervisor**: Karl Audun Lehne**

M.Sc. Thesis Title

Application of Petrophysical Logs and Failure Model for Prediction of Sand Production

Credits: 30 ECTS

Key words: Formation Evaluation Well logging Sand Production Failure Mohr-Coulomb Model	Pages: 77 + enclosure: 23 Stavanger, 26th June, 2011

University of Stavanger

Application of Petrophysical Logs and Failure Model for Prediction of Sand Production

by

Yaser Mirzaahmadian

A THESIS

SUBMITTED TO THE FACULTY OF SCIENCE AND TECHNOLOGY

IN PARTIAL FULFILLMENT OF THE REQUIREMENTS FOR THE DEGREE

OF MASTER OF SCIENCE IN PETROLEUM ENGINEERING

Faculty of Science and Technology

Department of Petroleum Engineering

Stavanger, NORWAY

June, 2011

To my lovely Wife

Saghar

Abstract

Prediction of sand production condition and rock failure in petroleum industry has been received lots of interests currently. Calculation of geomechanical elastic rock parameters based on the petrophysical logs is one of the novel methods that can be used for this purpose and is not considered as a research topic at Institute of Petroleum Technology, University of Stavanger.

This thesis addresses two main parts. The first part describes the petrophysical evaluation of well 7121/4-F-2 H drilled in Snøhvit field using Interactive Petrophysics version 3.4 from Schlumberger. A numerical MATLAB code is also developed and explained in the second part to demonstrate the application of well logs and failure model for prediction of sand production and calculation of critical well bore pressure.

Two sets of well log data from Snøhvit and Goliat fields are used to show the applicability of the generated code. It is interesting to see that critical well bore pressure for the Tubåen formation in Snøhvit field is negative indicting the low possibility of sand production while in the Goliat field, it is positive for the same formation. The risk of sand production in Goliat field has been observed during production and confirms the validity of the method and program. The different behavior of the two case studies can be linked to the packing of sand grains and cementation due to the burial depth and considerable overburden pressure. The compaction of Tubåen formation in Snøhvit field is seen from the log data. The presence of gas, oil and water in Well 7122/7-3 in Goliat field results to the diversity of sonic travel times and the rock elastic parameters compared to the corresponding data for the well 7121/4-F-2 H where the formation fluid is only water.

Acknowledgements

Many people have aided in the initiation, progress and achievement of this study, each in their own way. First, I would like to express my appreciation to my supervisor, Associate Professor **Karl Audun Lehne** for his guidance, enlightenments and encouragement through my Master Thesis. His patience, guidance and generosity allowed me to achieve lots of positive experiences at University of Stavanger. I am also indebted to my advisor, **Lykke Gemmer** from Statoil ASA. Without her sincere help and advice, accomplishment of this project was not possible. Thanks are also extended to **Eva Margot Holand** from Statoil ASA, for supporting the data and information.

I would like to appreciate University of Stavanger and HESS Norge for the scholarship to pursue my graduate studies.

The last but not least, I revere my wife, **Saghar**, who has made me flow to this moment. Her inspiration and incessant moral support is undeniable for my success in graduate studies.

26th June, Stavanger

Yaser Mirzaahmadian

Table of Contents

List of Figures

List of Tables

Nomenclature

μ	Coefficient of internal friction(Chapter2)
φ	Friction angle
α	Biot elastic constant
Δt_c	Compressional wave travel time
Δt_s	Shear wave travel time
Δ_s	Area
μ	Poisson's ratio
ρ	Density
ρ_b	Bulk density
Φ	Porosity
σ_h	Total smallest horizontal stress
σ_r	Radial stress
σ_θ	Tangential stress
σ_z	Vertical stress
σ_{ij}	Stress in *ij* -direction
C_B	Bulk compressibility
a	Lithology factor
C_R	Rock compressibility
D	Depth in meters
E	Young modulus
GR	Gamma ray log
G	Shear modulus
K_B	Bulk modulus
K_R	Rock modulus
m	Cementation factor
n	Saturation exponent
NPHI	Neutron log
P_f	Pore pressure
P_{fn}	Normal pore pressure

Pcp	Capillary suction
P_{we}	Pressure in the wetting fluid
P_c	Critical wellbore pressure
P_{nw}	Pressure in the Non-wetting fluid
P_o	Overburden pressure
P_p	Pore pressure
P_m	Mud pressure
RHOB	Density log
R_W	Formation water resistivity
R_t	True formation resistivity
S_{XO}	Invaded zone water saturation
SW	Water saturation
S_0	Inherent shear strength
τ_{max}	Maximum shear stress
τ_i	Initial shear strength
T	Traction (Chapter 2)
T	Temperature (Chapter 4)
TVD	True vertical depth
UCS	Uniaxial compressive strength
VSH	Shale volume
V_{cl}	Clay volume

CHAPTER I
Introduction

Sand production is one of the major challenging issues in different steps of field development planning including wellbore stability during drilling, production and IOR/EOR stages. It poses some disadvantages such as erosion to surface and downhole facilities, fine migration to the gas and oil wells. Since sand control is generally an expensive investment for an oil/gas operator, it is of great interests for the operator to estimate if sand control is needed before production, or when sand control is needed after some time of sand-free production. To provide technical support for sand control decision-making, it is necessary to predict the production condition at which sand production occurs. The source of sand production is related to the unconsolidated grains of the formation or the rock failure during well bore drilling and perforation as well as hydrocarbon production. Accordingly it is of great interest to estimate the critical conditions that the rock failure occurs and sand migration is initiated. In practice, rock failure and sand production can be predicted either from the core laboratory experiments or evaluation of petrophysical logs as an in-situ method. The advantage of evaluation of rock elastic parameters to calculate the rock strength from logs is recognized as the real and original condition of the measurements. In contrast the laboratory analysis is implemented for the cores at simulated field condition.

In this thesis, petrophysical evaluation of well log data is coupled to the Mohr-Coulomb failure criterion to predict the critical well bore pressure and sand production condition. A MATLAB code is developed to calculate the dynamic elastic parameters from well log data and Interactive petrophysics software is used to assess the formations.

1.1. Thesis structure

The present thesis is divided in five chapters and three Appendixes. Chapter two is an overview to the principals of rock mechanics and basic equations. Related published literatures regarding the assessment of rock strength parameters from well logs are cited at the end. Chapter three presents the general geological and reservoir information of the studied two fields. Chapter four pertains to petrophysical evaluation of the studied formations as well as calculation procedures of dynamic rock elastic parameters and prediction of rock failure based on the Mohr-Coulomb method and logs. Finally in chapter five, final remarks including the final conclusions and recommendations for future studies are mentioned. Appendix A includes

the generated MATLAB codes. The graphical elastic parameters generated from the MATLAB code are presented in Appendix B and the raw data used in this study is attached in Appendix C.

CHAPTER II
Background and Literature Review

The fields of study devoted to understanding the basic processes of rock deformation and their technological significance is defined as rock mechanics. The significance of rock mechanics for petroleum engineering is considerable. Prediction of the mechanical behavior of underground formations is the key in rock mechanics to avoid borehole instabilities in drilling, hydrocarbons production and brine/ CO_2 injection during enhanced oil recovery processes. If rock deformation results in a noticeable contraction of the wellbore due to the induced stress in the formation immediately adjacent to the wellbore, the drilling processes may be restricted or the emplacement of the casing, after drilling ceases, may be hampered.

If the deformation results in a large expansion of the wellbore, the rock formation may fracture and result in lost circulation while drilling and sand production during production stages. Consequently, predicting the mechanical behavior of reservoir rock is essential for drilling, well completion and stimulation as well as EOR/IOR programs. Reservoir geomechanics, which may lead to formation fracture and sand production, is a critical factor with respect to design of the well completion and to the overall reservoir performance during production or enhanced oil recovery programs. The production of oil, natural gas and water from underground rock formations or injection of water/CO2 during enhanced oil recovery results in a local change in the stress and strain field in the formation due to the decline in pore pressure. In order to predict the compaction or compressibility behavior of petroleum reservoirs due to this decline in pore pressure, it is necessary to know the compressibility characteristics of the reservoir rock.

Rock mechanical properties, such as Poisson's ratio, shear modulus, Young's modulus, bulk modulus, and compressibility can be obtained from two different sources (Fjær et al. 2008):

(1) Laboratory measurements, which allow for direct measurements of strength parameters and static elastic behavior with recovered core material from discrete depths.

(2) Down hole measurements through wireline logging, which allow the determination of dynamic elastic constants from the continuous measurement of compressional and shear velocities.

However, it is important to remember that, because reservoir rocks are often layered, fractured, faulted and jointed, rock masses sometimes may be controlled more in their reactions to applied loads by the heterogeneous nature of the overall rock mass than by the microscopic properties of the rock matrix. Consequently, the mechanical properties obtained from laboratory core tests may be slightly or considerably different from those existing in-situ. Rock core alteration during and after drilling stage also may influence the geotechnical parameters (Taib and Donaldson 2004).

This chapter reviews the main and essential literatures regarding to petroleum reservoir geo-mechanical rock properties achievable by laboratory measurements or petrophysical logs. In addition the concept of sand production and related mechanisms, linked to the rock failure criteria, has been explained extensively.

2.1. Stress and related concepts

Stress is defined as a force per surface area through which the force is acting, as shown in Figure 2.1 (Mulders 2003). In the left part of a body with a small element on the surface is shown. The external traction T represents the force per unit area acting at a given location on the body's surface. Traction T is a bound vector, which means T cannot slide along its line of action or translate to another location and keep the same meaning. A traction vector cannot be fully described unless both the force and the surface where the force acts, has been specified. Given both ΔF and Δs, the traction T can be defined as (Angelov 2009):

$$T = \lim_{\Delta s \to o} \frac{\Delta F}{\Delta s} = \frac{df}{ds} \tag{1}$$

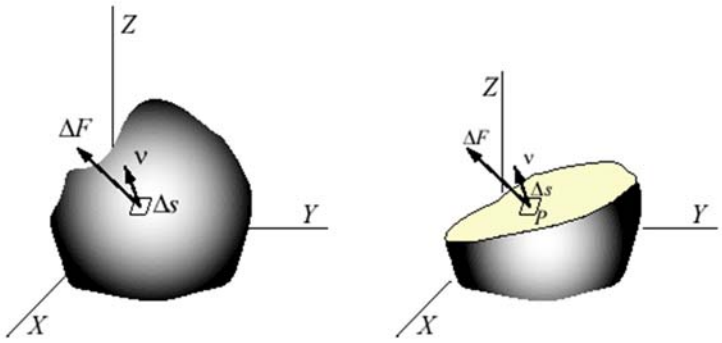

Figure 2.1. Left - force acting on the body surface, Right - force acting inside a solid (Mulders 2003)

The internal traction within a solid (see the right part of Figure 2.1) can be defined in a similar way. Surface tractions would appear on the exposed surface, similar in form to the external

tractions applied to the body's exterior surface. Stress therefore can be interpreted as internal tractions that act on a defined internal plane. Surface tractions or stresses acting on an internal datum plane, are typically decomposed into three mutually orthogonal components. One component is normal to the surface and represents normal stress. The other two components are tangential to the surface and represent shear stresses (see Figure 2.2). The stress state at point P (Figure 2.2) can be represented with an infinite small cube with three stress components on each side of the cube.

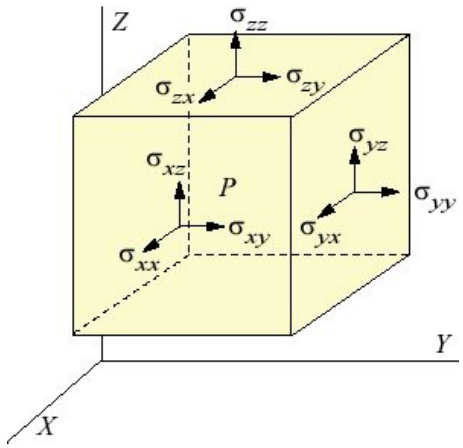

Figure 2.2. Components of stress vectors on coordinate planes (Mulders 2003)

If the body is under static equilibrium, then the state of stress can be represented with nine components from three sides of the cube. These nine components can be organized in one matrix (Fjær et al. 2008):

$$\sigma = \begin{bmatrix} \sigma_{xx} & \sigma_{xy} & \sigma_{xz} \\ \sigma_{yx} & \sigma_{yy} & \sigma_{yz} \\ \sigma_{zx} & \sigma_{zy} & \sigma_{zz} \end{bmatrix} \quad (2)$$

Where shear stress as mirrored across the diagonal of the matrix $\sigma_{ij} = \sigma_{ji}$ are identical as a result of static equilibrium. The matrix in equation (2) is known as the stress tensor. The traction on a plane with normal vector n is related to the stress tensor via $T = \sigma.n$.

2.2. Strain and related concepts

Consider a bar with initial length L which is stretched to a length L_0. (The strain measure ε, a dimensionless ratio, is defined as the ratio of elongation with respect to the original length; the above strain measure is defined in a global sense. The strain at each point may vary dramatically if the bar's elastic modulus or cross-sectional area changes (Angelov 2009).

$$\varepsilon = \frac{\Delta l}{l_0} \tag{3}$$

The components of strain for a solid like in the Figure 2.2 can be organized in a matrix similar to the stress tensor (Equation 4) (Fjær et al. 2008):

$$\varepsilon = \begin{bmatrix} \varepsilon_{xx} & \varepsilon_{xy} & \varepsilon_{xz} \\ \varepsilon_{yx} & \varepsilon_{yy} & \varepsilon_{yz} \\ \varepsilon_{zx} & \varepsilon_{zy} & \varepsilon_{zz} \end{bmatrix} \tag{4}$$

The constitutive equations in mechanics are characterizing the behavior of specific materials. The relationship between internal stress and internal strain can be expressed as a constitutive equation (Tigrek 2004). The mechanical behavior of real materials is very diverse and complex and it would be impossible to formulate equations which are capable of determining the stress in a body under all circumstances (Spencer 2004). The aim is to establish equations which describe the most important features of the behavior of the material in a given situation. Such equations could be regarded as defining ideal materials. One ideal model is based on the assumption of a linear relation between stress and strain which will lead to a linear constitutive equation. The common effect of different strain histories will be equal to the sum of the effects of the individual strain histories. For a locally reacting material the internal stress at a certain fixed position can be related entirely to the strain history of that local material (Tigrek 2004). Materials following the same constitutive equations are building one rheological class.

Depending on the material properties and stress/strain relation the rheological classes can be elasticity, plasticity, or viscosity. In our case study we will discuss only the case of elasticity. Elastic behavior is characterized by the following two conditions: (1) the stress in a material is a unique function of strain, and (2) the material has the property of complete recovery to a "natural" shape upon removal of applied forces (Mase 1999). The behavior of a material can be elastic or not elastic (inelastic). Elastic behavior means that applied stress leads to a strain, which is reversible when the stress is removed. Linear elasticity implies that the relationship

between stress and strain is linear, which is correct only in the case of small strains, or small stress increments. Most rock mechanics applications are based on linear elasticity, although it is well established that most sedimentary rocks exhibit non-linear behavior, plasticity, and even time dependent deformation (creep). However, the linear elasticity is simple, and the parameters required can be estimated from log data and standard laboratory tests. The rocks in the upper lithosphere can be considered elastic for loads with a duration that is short when compared with the age of the Earth (Ranalli 1995). This gives us the ability to consider elasticity as the most important rheological class in geo-mechanical modeling (Tigrek 2004). In three-dimensional case the link between stress and strain is given with the stiffness matrix which has 81 components. Due to the symmetry of the stress tensor, strain tensor, and stiffness tensor, only 21 elastic coefficients are independent. The stiffness and compliance matrices of a solid, isotropic and linearly elastic material have only 2 independent variables (i.e. elastic constants):

2.3. Strength of rock samples

Strength is the ability of rock to resist stress without yielding or fracturing (Fjær et al. 2008). It is influenced by the mineralogy of the rock particles and by the character of the particle contacts (Taib and Donaldson 2004). Figure 2.3 illustrates a typical test specimen, a cylinder with length to diameter ratio 2:1. An (axial) stress to the end faces of the cylinder, while a confining oil bath provides a stress of possibly different magnitude to the circumference (Fjær et al. 2008). If the confining stress is zero, the stress is uniaxial stress test (also called unconfined compression test). When the test is performed with a non-zero confining pressure, a so-called triaxial test is performed. Uniaxial compressive strength tests are used to determine the ultimate strength of a rock, i.e., the maximum value of stress attained before failure. The uniaxial strength is one of the simplest measures of strength to obtain These properties are the result of the various processes of deposition, diagenesis, and catagenesis that formed the rock, later modified by folding, faulting, fracturing, jointing, and weathering. Consequently, the strength of rocks reflects their geological history (Taib and Donaldson 2004). Rock strength is estimated from two common laboratory techniques: uniaxial compressive strength tests, and triaxial or confined compressive strength tests. Uniaxial compressive strength tests are used to determine the ultimate strength of a rock, i.e., the maximum value of stress attained before failure.

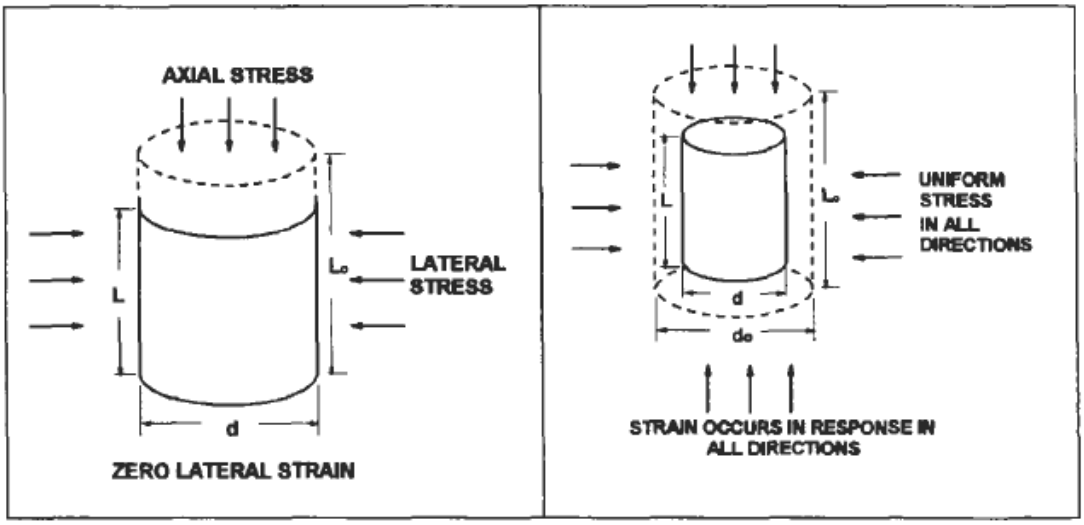

Figure 2.3. Typical samples for uniaxial or triaxial tests (Taib and Donaldson 2004)

The uniaxial strength is one of the simplest measures of strength to obtain. Its application is limited, however, and it is generally used only when comparisons between rocks are needed. Uniaxial compression tests are influenced by several factors: size and shape of the test sample, rate of loading, amounts and types of fluid present in the rock sample, mineralogy, grain size, grain shape, grain sorting, and rate of loading (Taib and Donaldson 2004).

(1) The length-to-diameter ratio, also called the slenderness ratio, of the rock sample should be approximately 2 to 1.

(2) The ends of the sample should be parallel and ground flat to within 0.025 mm; otherwise, low values of compressive strength are obtained.

(3) Size effects are considerable only if flaws exist in the rock sample: The larger the sample, the greater the probability of a flaw existing in the sample. Size effects can be reduced by testing a large number of samples with the same size and calculating the average, preferably the geometric mean, of compressive strength values.

(4) Because fluid content could reduce the compressive strength, it is recommended to perform the uniaxial test under fluid saturations similar to those existing in the reservoir. Reduction in compressive strength due to the presence of fluids could occur in several ways. It is probable; however, that in many rocks the effect of pore pressure is the main cause of reduction in rock strength. The pore pressure could affect the intergranular contact stresses and cause instability along a weakness plane.

(5) High rates of loading should be avoided, as they tend to yield abnormally high compressive strength values. Loading rates in the range of 0.5 MPa/s to 3 MPa/s are considered normal and generally cause negligible change in compressive strength of rock samples.

Uniaxial test in Figure 2.4 has been shown for typical test. The applied axial stress (denoted σ_z) is plotted as a function of the axial strain (ε_z) of the sample. In elastic region the rock deforms elastically. If the stress is released, the specimen will return to its original state. After Yield point, the point beyond which permanent changes will occur. The sample will no longer return to its original state upon stress relief.

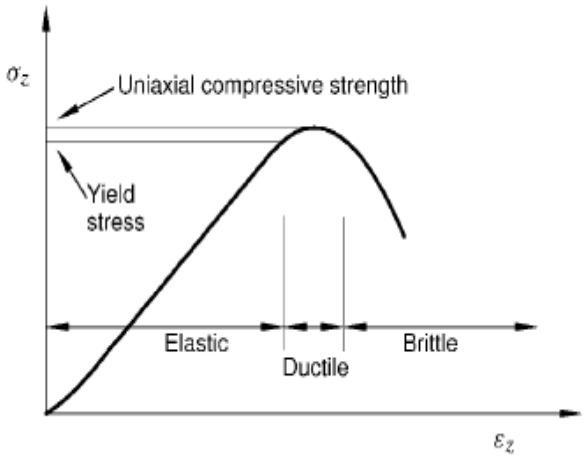

Figure 2.4. Principle sketch of stress versus deformation in a uniaxial compression test (Fjær et al. 2008)

At Uniaxial compressive strength, the peak stress. In ductile region**,** the sample undergoes permanent deformation without losing the ability to support load. In brittle region**,** the specimen's ability to withstand stress decreases rapidly as deformation is increased (Fjær et al. 2008). The relation between the stress and strain is commonly expressed in graphs known as stress-strain diagrams. The rock in Figures 2.5 and 2.6 is under compression. With increasing stress the specimen becomes shorter, and the strain (deformation) is plotted in terms of the percentage of shortening of the rock sample. Curve A represents a typical behavior of a brittle rock, which deforms elastically up to a stress of approximately 20,000 psi (137.9 MPa), shortening 0.5% before rupture. Curve B describes an ideal plastic substance. First it behaves elastically until reaching the proportional elastic limit, which is the point at which the curve departs from the straight line. Then the rock deforms continuously with any added stress.

Curves C and D can represent the more typical plastic behavior of the rock. Once the elastic limit is reached, rock sample C becomes progressively more difficult to deform. With increased stress, rock sample D reaches its ultimate strength point, beyond which less stress is necessary to continue the deformation until rupture. The mechanical behavior of rocks is controlled not only by their inherent properties, e.g., mineralogy, grain size, porosity, width and density of fractures, etc., but also confining pressure, temperature, time, and interstitial fluids. It is evident that the strength of the rock increases with confining pressure. Such experiments indicate that rocks exhibiting very little plastic deformation near the surface of the earth may be very plastic under high confining pressure (Taib and Donaldson 2004).

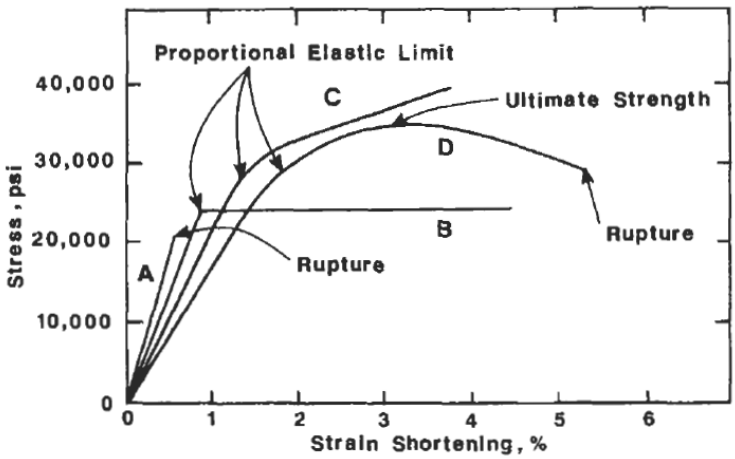

Figure 2.5. Stress-strain diagrams (Taib and Donaldson 2004)

Thus, under a confining pressure of 1,000kg/cm$_2$ or greater, limestone will deform plastically. Heating particularly enhances the ductility-that is, the ability to deform permanently without loss of cohesion-of calcareous and evaporate rocks; however, it has little effect upon sandstones. Much rock deformation takes place while solutions capable of reacting chemically with the rock are present in the pore spaces. This is notably true of metamorphic rocks, in which extensive or complete recrystallization occurs.

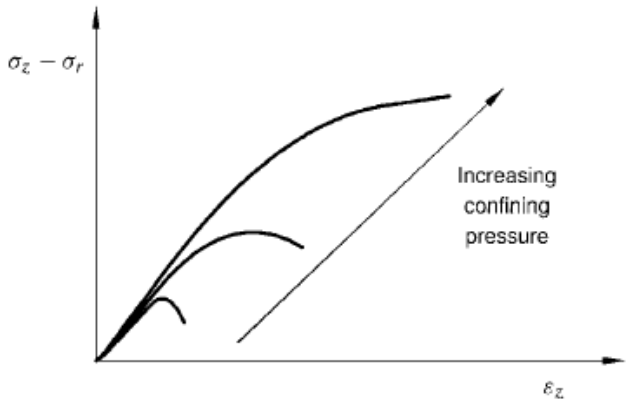

Figure 2.6. Triaxial testing: typical influence of the confining pressure on the shape of the differential stress (axial stress minus confining pressure) versus axial strain curves (Fjær et al. 2008)

A triaxial test is usually performed by increasing the axial and confining loads simultaneously, until a prescribed hydrostatic stress level is reached. The axial loading is normally applied such that it gives a constant axial deformation rate. The most common mode of failure observed in uniaxial and triaxial tests is shear failure. This failure mode is caused by excessive shear stress. Another failure mode is tensile failure, which is caused by excessive tensile stress. Finally, pore collapse is a failure mode that is normally observed in highly porous materials, where the grain skeleton forms a relatively open structure. Pore collapse is usually caused by excessive hydrostatic stress (Fjær et al. 2008)

.

2.4. Tensile failure

Tensile failure is occurring if the effective tensile stress across some plane in the sample exceeds a critical limit. This limit is called the *tensile strength*; it is given the symbol T_0, and has the same unit as stress (Taib and Donaldson 2004). The tensile strength is a property of the rock. Sedimentary rocks have a rather low tensile strength, typically only a few MPa or less. In fact, it is a standard approximation for several applications that the tensile strength is zero. A sample that suffers tensile failure typically splits along one or very few fracture planes, as illustrated in Figure 2.7. The fracture planes often originate from preexisting cracks oriented more or less normal to the direction of the tensile stress. The highest probability of damage for the rock is at the perimeter of the largest of these cracks; hence the largest crack(s) will grow increasingly faster and rapidly split the sample. The tensile strength is sensitive to the presence of cracks in the material. The failure criterion, which specifies the stress condition for which

tensile failure will occur, and identifies the location of the failure surface in principal stress space, is given as(Fjær et al. 2008):

$$\sigma = -T_0 \tag{5}$$

Risnes and Bratli (1981) defined a tensile failure criterion for perforation tunnel inner shell collapse. Risnes and Bratli (1981) used the same parameter to hollow cylinder. Tensile failure is occurring when the effective radial stress is equal to the tensile strength of the formation rock. Based on Risnes and Bratli's work, Vaziri (1995) employed a fully coupled fluid flow and deformation model to consider the effect of transient fluid flow, nonlinear soil and fluid behavior on sand production. It was found that a cavity, tensile zone, plastic zone and nonlinear elastic zone may form around wellbore. Perkins and Weingarten (1988) studied the conditions necessary for stability or failure of a spherical cavity in unconsolidated or weakly consolidated rock. Weigarten and Perkins derived an equation describing tensile failure condition in terms of pressure drawdown, wellbore pressure, formation rock cohesion and frictional angle.

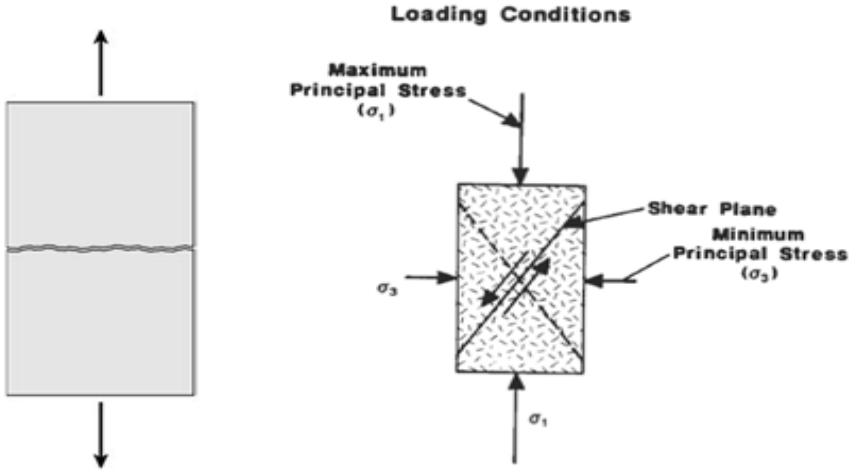

Figure 2.7. Tensile and shear failure (Fjær et al. 2008; Taib and Donaldson 2004)

2.5. Shear failure

Shear failure occurs when the shear stress along some plane in the sample is sufficiently high. Eventually, a fault zone will develop along the failure plane, and the two sides of the plane will move relative to each other in a frictional process, as shown in Fig. 2.8. It is well known that the frictional force that acts against the relative movement of two bodies in contact depends on the force that presses the bodies together. It is therefore reasonable to assume that the critical

shear stress (τ_{max}) for which shear failure occurs, depends on the normal stress (σ') acting over the failure plane. That is (Fjær et al. 2008; Taib and Donaldson 2004)

$$|\tau_{max}| = f(\sigma') \quad (6)$$

This assumption is called Mohr's hypothesis. In the τ–σ' plane, Eq. (6) describes a line that separates a "safe region" from a "failure" region. Eq. (6) can be considered as a representation of the failure surface in the τ–σ' plane. The line is sometimes referred to as the failure line or the failure envelope. An example is shown in Fig. 2.8, where we have also indicated the three principal stresses and the Mohr's circles connecting them. The stress state of Fig. 2.8 represents a safe situation, as no plane within the rock has a combination of τ and σ' that lies above the failure line. Assume now that σ'_1 is increased. The circle connecting σ'_1 and σ'_3 will expand, and eventually touch the failure line. The failure criterion is then fulfilled for some plane(s) in the sample, and the sample fails. Note that the value of the intermediate principal stress (σ'_2) has no influence on this situation. Since σ'_2 by definition lies within the range (σ'_3, σ'_1), it does not affect the outer of Mohr's circles, and hence it does not affect the failure (Fjær et al. 2008; Taib and Donaldson 2004).

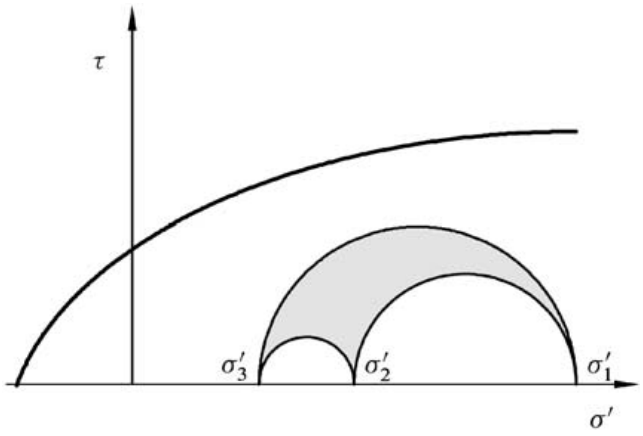

Figure 2.8. Failure curves as specified by Eq. (6), in the shear stress–normal stress diagram (Fjær et al. 2008; Taib and Donaldson 2004)

Several rock strength criteria have been employed to predict well bore stability and sand production in the literature. Laboratory tests may be necessary to know which strength criterion best describes the behavior of the rock studied. Among those strength criteria, the Von Mises criterion is used more in metal than in porous media, the Mohr Coulomb and Hoek-Brown criteria consider only the effect of maximum and minimum principal stresses while

the Drucker-Prager, Modified Lade and Modified Weilbols & Cook criteria involve also intermediate principal stress (EI-Sayed 1991). The systematic comparison of the use of all those criteria has not been made. For rock behaves in the brittle regime, the sand production criterion may be the same as the rock strength criterion. However, for rock behaves in the ductile regime, it may be necessary to simulate the post yield behavior (hardening or softening) and to propose some other sand production criterion. Thus, pure shear failure, as defined by Mohr's hypothesis, depends only on the minimum and maximum principal stresses and not on the intermediate stress.

By choosing specific forms of the function $f(\sigma')$ of Eq. (6), various criteria for shear failure are obtained. The simplest possible choice is a constant. The resulting criterion is called the Tresca criterion. The criterion simply states that the material will yield when a critical level of shear stress is reached (Fjær et al. 2008; Taib and Donaldson 2004):

$$\tau_{max} = 12(\sigma'_1 - \sigma'_3) = S_0 \quad (7)$$

S_0 is the *inherent shear strength* (also called *cohesion*) of the material. In a Mohr τ–σ' plot the Tresca criterion appears simply as a straight horizontal line.

2.6. Pore collapse

During the depletion of the reservoir pressure, the effective stress acting on the formation rock increases. At a certain stress level, pore collapse may occur and this may lead to rock failure. The previous listed criteria are just good to describe failure in the brittle regime and cannot be used to describe failure by pore collapse. As a result, it is necessary to run both triaxial and hydrostatic tests to construct a complete failure envelope. Some efforts have been made to construct a complete failure envelope and apply it in sand production prediction. Through triaxial and hydrostatic tests of a variety of sandstones, a single normalized failure envelope was established by Zhang et al. (1990). The only parameter appears in the normalized envelope is critical pressure, which is correlated to the compression wave velocity. It is not clear if this normalized envelope can be applied universally.

2.7. The Mohr–Coulomb criterion

If a piece of rock is subject to sufficiently large stresses, a failure will occur. This implies that the rock changes its shape permanently, and possibly also falls apart. The condition is accompanied

with a reduced ability to carry loads. Rock failure is an important phenomenon also for petroleum related rock mechanics, as it is the origin of severe problems such as borehole instability and solids production. It is therefore useful to be able to predict under which conditions a rock is likely to fail (Fjær et al. 2008; Taib and Donaldson 2004). A more general and frequently used criterion is the Mohr–Coulomb criterion, which is based on the assumption that $f(\sigma')$ is a linear function of σ':

$$|\tau| = S_0 + \mu\,\sigma' \tag{8}$$

Here μ is the *coefficient of internal friction*. The latter term is clearly chosen by analogy with sliding of a body on a surface, which to the first approximation is described by Amontons' law:

$$\tau = \mu\,\sigma' \tag{9}$$

In Figure 2.8 we have drawn the Mohr–Coulomb criterion, and a Mohr's circle that touches the failure line. The angle φ defined in the Figure is called the *angle of internal friction* (or *friction angle*) and is related to the coefficient of internal friction by

$$\tan\varphi = \mu \tag{10}$$

Note that the Tresca criterion can be considered as a special case of the Mohr–Coulomb criterion, with $\varphi = 0$. The intersection point between the Mohr–Coulomb failure line and the normal stress axis is of no practical interest in itself, as the point is inaccessible due to tensile failure. However, for some purposes it is convenient to make use of the parameter A defined as the distance from the intersection point to the origin (see Figure 2.9). The parameter is called the *attraction*. The attraction is related to the other Mohr–Coulomb parameters by

$$A = S_0 \cot\varphi \tag{11}$$

Figure 2.9 also shows the angle 2β, which gives the position of the point where the Mohr's circle touches the failure line. It can be seen from the figure that the shear stress at this point is:

$$|\tau| = 0.5\,(\sigma'_1 - \sigma'_3)\sin 2\beta \tag{12}$$

In Figure 2.10 the relation between the tangential and normal stress on the cross section plane has been shown graphically.

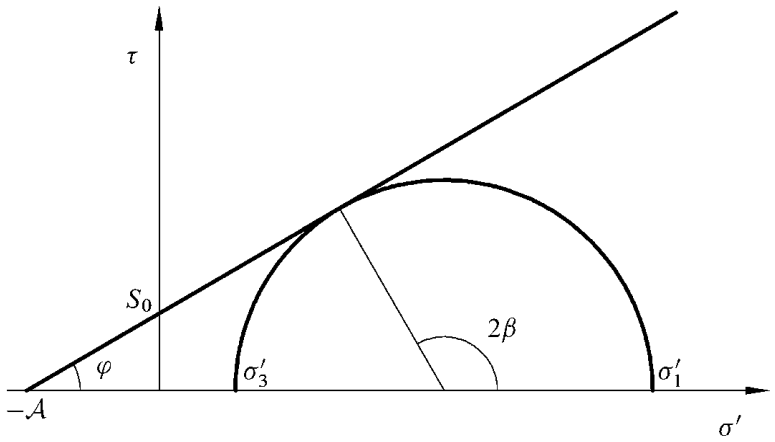

Figure 2.9. Mohr–Coulomb criterion in τ– σ' space (Fjær et al. 2008)

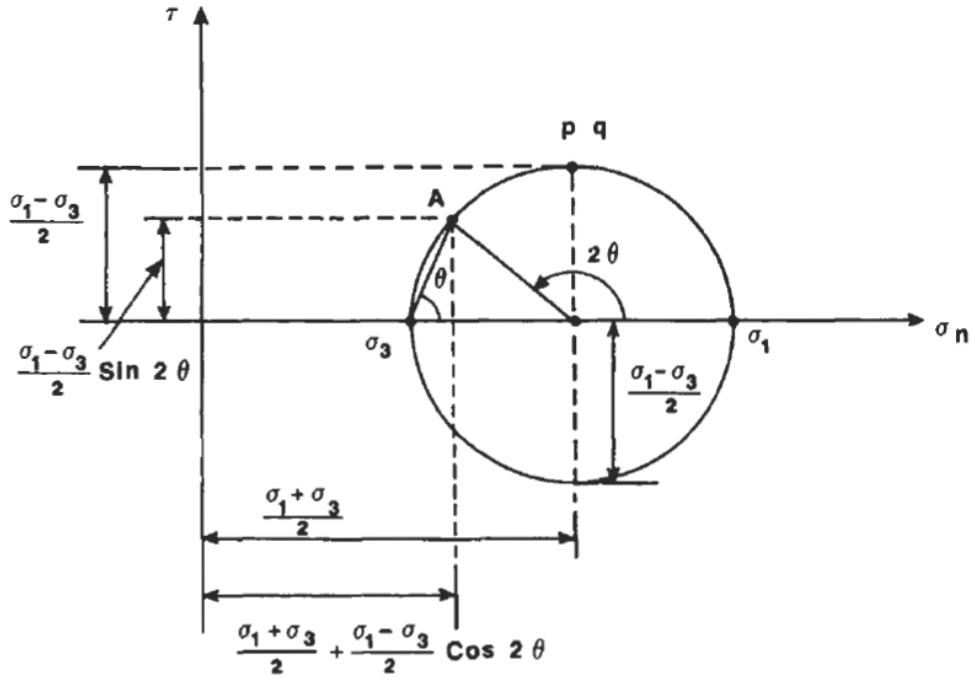

Figure 2.10. Graphical illustration of tangential and normal stress in τ– σ' space (Taib and Donaldson 2004)

While the normal stress is

$$\sigma' = 0.5\,(\sigma'_1 + \sigma'_3) + 0.5\,(\sigma'_1 - \sigma'_3)\cos 2\beta \qquad (13)$$

Also, we see that β and φ are related by

$$\varphi + \pi/2 = 2\beta \qquad (14)$$

Since β is the angle for which the failure criterion is fulfilled, β gives the orientation of the failure plane (see Fig. 2.9). From Eq. (12) we have that

$$\beta = \pi/4 + \varphi/2 \qquad (15)$$

The allowable range for φ is from 0° to 90° (in practice the range will be smaller, and centered on approximately 30°), hence it is clear that β may vary between 45° and 90°. It is concluded that the failure plane is always inclined at an angle smaller that 45° to the direction of σ'. Fig. 2.11 shows schematically how the failure planes may be oriented in a rock described by the Mohr–Coulomb criterion. One important point to note is that β is given solely by φ, which is a constant in the Mohr–Coulomb criterion. Thus the orientation of the failure plane is independent of the confining stress. This is a special feature for the Mohr–Coulomb criterion. Experiments often show that the failure angle decreases with increasing confining pressure, in particular at low confining pressures (Fjær et al. 2008).

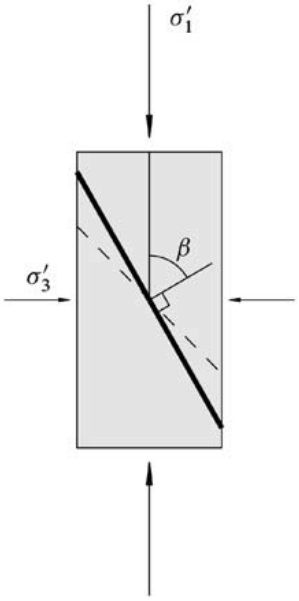

Figure 2.11 Orientation of the failure plane relative to the largest principal stress. (The thick solid line shows the failure plane for a friction angle of 30°. The dashed line shows the maximum inclination of the failure plane relative to σ'_1, according to the Mohr–Coulomb criterion) (Taib and Donaldson 2004)

2.8. Compaction failure

Pore collapse is a failure mode that is normally observed only in high porosity materials, when the material is compressed, grains may loosen or break and then be pushed or twisted into the open pore space, resulting in a closer packing of the material. This process is called compaction. This deformation mode is schematically illustrated in Fig. 2.12. (Fjær et al. 2008) In sandstones where the size of the pores is of the same order of magnitude as the size of the grains, pore collapse typically consists in reorientation of the grains to better fill the void spaces, as indicated in Fig. 2.12. For high porosity chalks, where the size of the individual

grains may be an order of magnitude smaller than the dimensions of the pore space, the pore collapse mechanism becomes very important. Pore collapse may occur under pure hydrostatic loading. Microscopically, however, failure will be due to local excessive shear forces acting through grains and grain contacts. From this point of view, pore collapse may be regarded as distributed shear failure within the material. Another failure mechanism that may occur under hydrostatic loading is grain crushing. If the stresses are sufficiently high, the grains may be partly crushed at the grain contacts, and splitting of the grains may result. Either way, these local failure mechanisms represent permanent damage of the rock framework and causes yielding, with associated reduction in the stiffness of the rock. This type of failure also occurs to some extent under non-hydrostatic stress conditions, and may be observed in triaxial tests at high confining pressure. The process is then referred to as shear enhanced compaction.

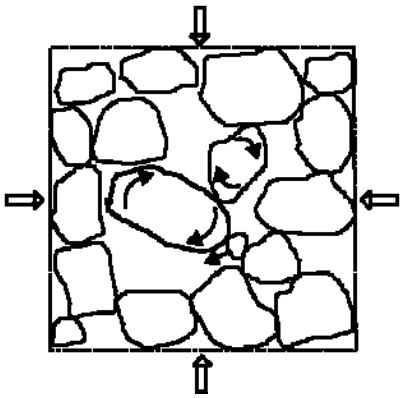

Figure 2.12. Grain reorientation resulting in a closer packing (Fjær et al. 2008)

2.9. Fluid effects

2.9.1. Pore pressure

In the section of failure criteria the pore pressure has appeared only indirectly through the effective stresses. The effective stresses are thought to represent the forces transmitted through the rock skeleton, which in turn causes the deformation of the material, while the remaining parts of the total stresses are carried by the pore fluid. As the pore pressure is equal in all directions, it will affect only the normal stresses. The shear stresses that are due to differences in the principal stresses will be unaffected. In a τ–σ' lot the effect of increasing the pore pressure while the total stresses are kept constant, is to move the Mohr circles to the left and closer to the shear and tensile failure lines, as illustrated in Figure 2.13. Thus, increasing pore pressure may destabilize a rock with respect to shear and tensile failure. The effective stress

concept in terms of the Biot constant α, was derived under the assumption that the rock is linearly elastic, and is not directly applicable for a rock at failure. It is, however, generally accepted that Terzaghi's definition of effective stress appears to be the most relevant definition to be used in failure criteria (Detournay and Cheng, 1988; Boutéca and Guéguen, 1999).

$$\sigma' = \sigma - P_f \quad (16)$$

2.9.2. Partial saturation

Even unconsolidated sand may have some degree of consolidation and water saturation (Fjær et al. 2008). This means that there is a meniscus of water at every grain contact, as shown schematically in Figure 2.13. It is energetically favorable for the grain–water–air system to maintain this constellation; hence a certain force is needed to rip the grains apart. This acts as cohesion, giving the moist sand a finite shear and tensile strength. The strength is fully recovered after a reorganization of the grains; hence the moist sand can be reshaped indefinitely. When the sand becomes completely dry or fully water saturated, the meniscus constellation is destroyed, and the cohesion and strength are gone. The effects of partial saturation occur whenever the pore space is filled with at least two immiscible fluids, like for instance oil and water. Normally, it is energetically favorable that one of the fluids (the wetting fluid) stays in contact with the solid material, while the other (non-wetting) fluid is shielded from the solid to some degree, giving a constellation as illustrated in Figure 2.13. This so-called capillary effect produces a difference in the pressure for the two fluids, given as:

$$P_{cp} = P_{nw} - P_{we} \quad (17)$$

Where P_{we} is the pressure in the wetting fluid, P_{nw} is the pressure in the non-wetting fluid, and P_{cp} is called the capillary suction. The magnitude of the capillary suction depends on the type of fluids, the condition of the solid surface (which determines the degree of wettability for the various fluids) and the size of the pore at the point where the two fluid phases meet. The wetting fluid will always tend to fill the smallest pores, so that the contact between the fluid phases will move to larger pores when the degree of saturation for the wetting fluid is increased.

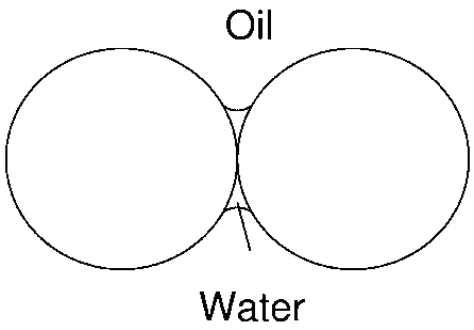

Figure 2.13. Schematic illustration of the distribution of fluids at a grain contact (Fjær et al. 2008)

Thus P_{cp} varies from one pore to the next, and falls off rapidly with the degree of saturation for the wetting fluid. The capillary suction has some effect on the effective stresses in the rock, and we may define a generalized effective stress (Bishop, 1959).

$$\sigma' = \sigma - \alpha(P_{nw} - S_{we}P_{cp}) \qquad (18)$$

*S*we is the degree of saturation of the wetting fluid. The term $S_{we}P_{cp}$ typically has a peak at a low value for S_{we} (≈0.1 or less) and vanishes for $S_{we} = 0$ and $S_{we} = 1$. It is normally quite small, however, typically less than 1 MPa even at its peak value, and can in most cases be ignored with respect to the effective stresses. The capillary suction also affects material properties that can be related to thinner granular cohesion of the rock (Papamichos et al., 1997). This is a more significant effect that may have a large impact on both the strength and the stiffness of the rock, as illustrated in Figure 2.14.

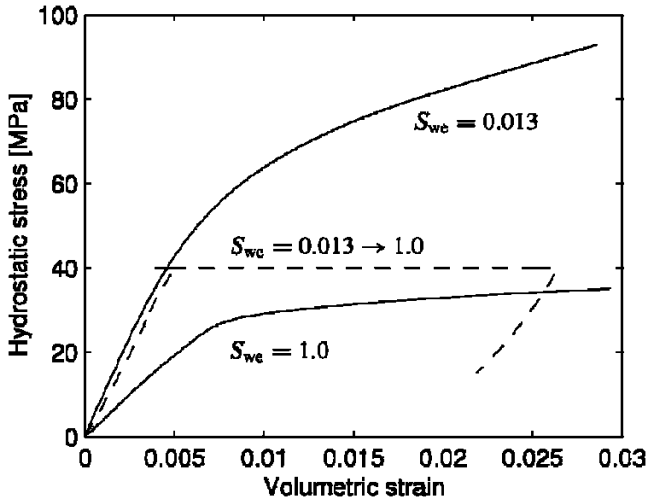

Figure 2.14. Hydrostatic compression tests at different levels of water saturation on chalk (Fjær et al. 2008)

2.10. Sand production

Sanding onset prediction is generally based on sand arch instability, perforation tunnel instability, or vertical, horizontal or deviated borehole instability. Generally, a stress model is established to obtain the stress state near the sand arch, perforation tunnel or borehole, and then a sand production criterion is applied to predict the stress state or fluid flow condition at which sand production occurs. Post-sanding behavior has also been studied to quantify the amount of sand produced. Sand production is a natural consequence of fluid flow into a wellbore from the reservoir. The process may be divided into the following stages the loss of mechanical integrity of the rocks surrounding an open hole or perforation (failure), separation of solid particles from the rocks due to hydrodynamic force (post-failure) and transportation of the particles to the surface by reservoir fluids (transport). The essential condition for sand production in weakly-consolidated and consolidated formations is therefore the failure the rock surrounding the cavity. Sand production from hydrocarbon fields has been a concern for the development. On the one hand, unnecessary down hole sand control not only significantly increases well cost but also impairs well productivity; on the other hand, sudden influx of large amount of sands into the wells damages down hole and surface production equipment and can be a major safety risk. It is therefore critical to accurately assess the likelihood of sand production to decide if down hole sand control is necessary during production life of the multi-fields prior to the development (YI 2003). Numerous factors such as rock mechanical properties, in-situ stress state, wellbore perforation geometry, pressure drawdown, pressure depletion, and water cut may influence sand production. Many efforts have been made to study the effect of those parameters. The final goal of these efforts is to know when sand production occurs and how much sand will be produced. The following paragraphs summarize those methods grouped by the underlying assumptions.

2.10.1 Sand arch stability

The role of arching in sand stability was first treated by Terzaghi in his trap door experiment, which demonstrated that arching was a real and stable phenomenon. Hall and Harrisberger initiated the study of sand arch stability in the oil industry (YI 2003). Their paper describes that “an arch is a curved structure spanning an opening, serving to support a load by resolving the vertical stress into horizontal stresses”. Sand arch is visualized as in Figure. 2.15. Their experiments were designed to determine whether fluid flow or change in load affects the

stability of sand arch. Effects of sand roundness, grain crush, fluid flow and wettability on sand arch formation and stability were studied. It was observed that angular sands are more likely to form sand arch than round sands. Inward fluid flow may help to stabilize sand arch formed by round sands. Slow outward fluid flow does not disrupt sand arch while faster flow does. Water cut tends to destroy the sand arch. Stein and coworkers described an application of sand arch stability theory, which assumes that the maximum sand-free rate an arch can tolerate is proportional to the shear modulus of the sand.

Later Tippie and Kohlhaas (1973) experimentally investigated further the effect of fluid flow rate on sand arch formation and stability. They concluded from their experiments that substantial sand-free producing rates can be maintained through stable sand arches in unconsolidated sands. Arch growth is a function of production rate and initial arch size. An arch may be destroyed and a new arch be formed through gradual increase of flow rate. Cleary *et* al (1973) experimentally studied the effect of stress and fluid properties on sand arch stability in unconsolidated sands. They reported that the arch size decreases with increasing confining stress. They found also that a more stable arch occurs when the horizontal stress is the maximum principal stress and the vertical stress is the minimum principal stress.

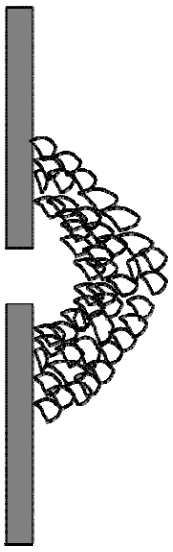

Figure 2.15. Sand arches near perforation (YI 2003)

The data required for the sand prediction study were obtained from laboratory and field measurements. Mechanical properties of the reservoir sandstones were established by conducting a number of unconfined compressive strength and triaxial tests on reservoir cores in conjunction with ultrasonic wave velocity measurements. The laboratory measured mechanical

properties were then correlated with the properties derived from open hole logs. The magnitudes of the in-situ stresses and formation pressure were derived from analysis of open hole logs, standard leak-off test data, coefficient of active earth pressure and qualitative stress information relating to the in-situ stress regime. The likelihood of sand production was assessed by analyzing perforation stability for cased, cemented and perforated wells. The sand production prediction model should be calibrated against laboratory perforation collapse test data on full-size reservoir sandstone core samples. Figure 2.16 shows the process of the sand production prediction study presented on the reported data in research paper by Wu et al.

2.10.2. In-situ stresses and formation pressure

Check shot and density logs should be used to determine vertical (overburden) stress magnitudes. The check shot logs should be used to calculate the stress magnitudes from the seabed to the depth where density logs are available. Bulk densities based on the check shot logs must be computed from a relationship between laboratories measured compressional velocity in a range of rocks and their densities (Wu et al 2004). The bounds for in situ stress estimation were developed by consideration of standard leak-off test data, qualitative stress information relating to recent fault movements in the immediate region and estimates of the coefficient of active earth pressure calculated from the effective angle of internal friction.

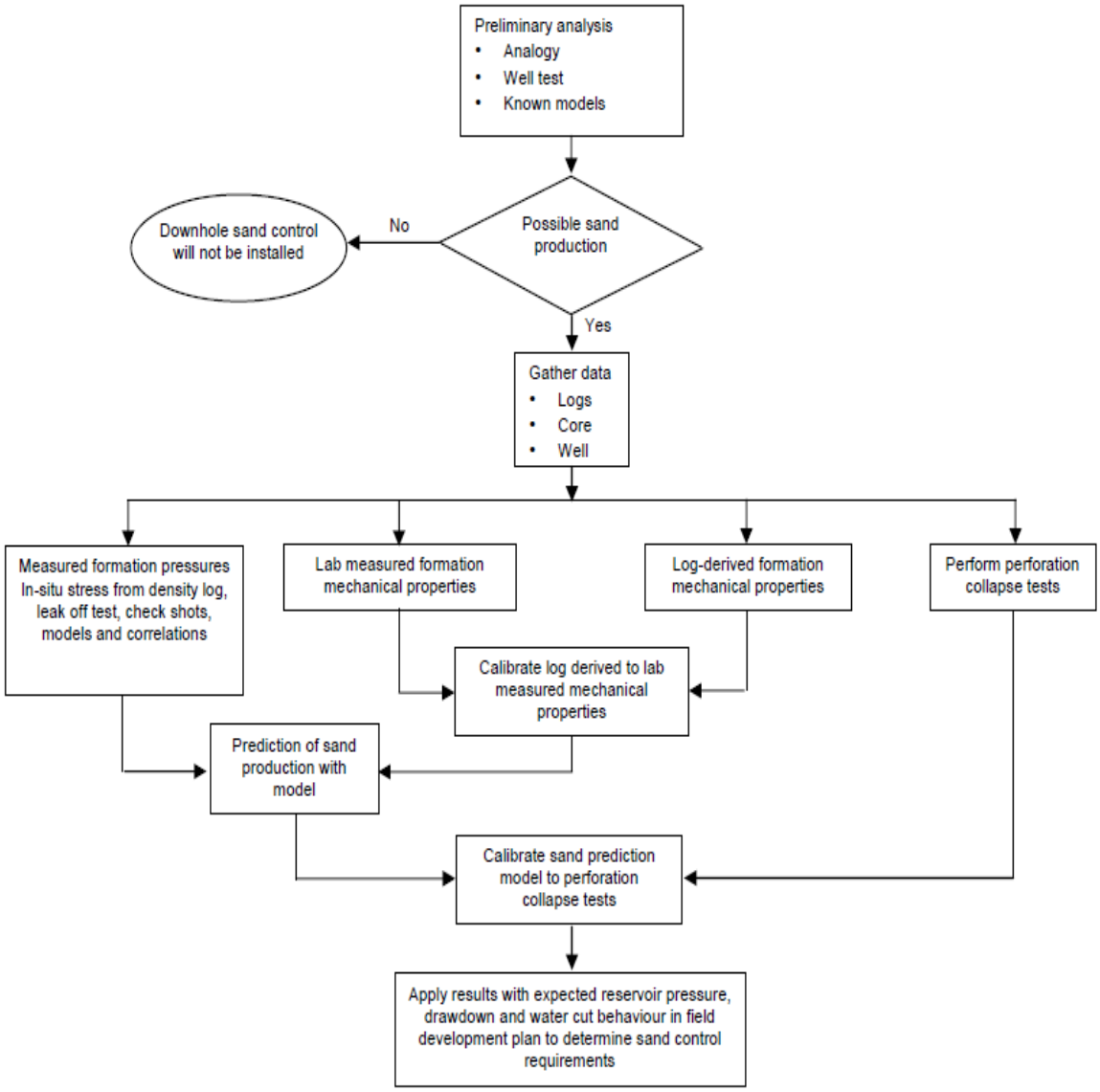

Figure 2.16. Sand production prediction study flow chart (Wu et al 2004)

Information relating to the stress regime being normal fault should be used in the determination of horizontal stress magnitudes. The standard leak-off pressures were assumed to have resulted in hydraulic fracture. The stress bounds determined should be checked for consistency with the occurrence of wellbore breakout and non-hydraulic fracture observed at various horizons in the studied fields. The occurrence of breakouts was inferred from single-arm caliper data. Figures 2.17 and 2.18 respectively show typical horizontal stress bounds determined at a particular reservoir depth, and typical profiles of the horizontal and vertical stresses.

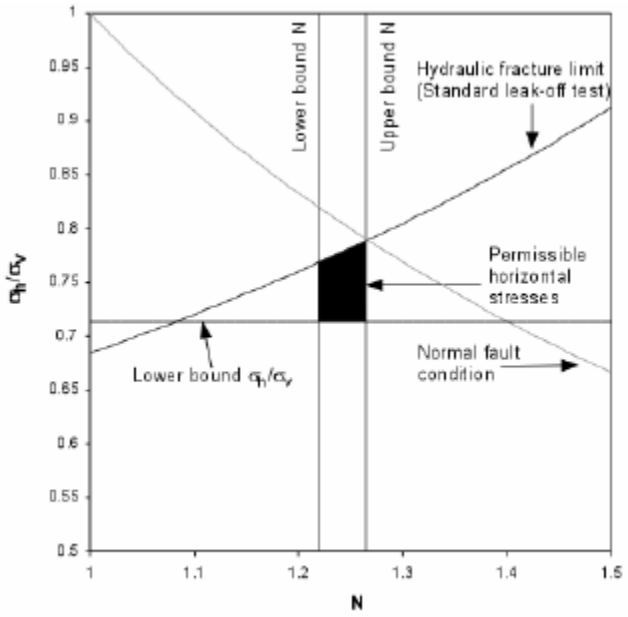

Figure 2.17. Permissible horizontal stress bounds (Wu et al 2004)

Bratli and Risnes (1984) studied in laboratory the sand arch phenomenon due to stresses imposed by flowing fluid. An elasto-plastic stress solution was obtained by simplifying the arch geometry as a hemisphere. They presented a stability criterion describing the total failure of sand, as well as the failure of an individual arch. Good agreement between theory and experimental data was shown. Later Polillo *et al*. studied the same problem with elasto-plastic finite element method (Fjær et al. 2008). Yim *et al*.'s experimental study showed that the ratio of sand grain size to outlet hole size and grain size distribution are important factors. More recently, Bianco and Halleck extended Hall and Harrisberger's work to study the effects of change in wetting phase saturation on arch behavior, morphology and stability. Their main conclusion is that within a defined range, a progressive increase in wetting phase saturation does not impact sand arch stability. As the wetting phase saturation exceeds a critical value, sand arch instability occurs. In the above papers, it is assumed that sand arch is formed around a perforation and the perforation just penetrates the well casing and cement sheath. This theory may also be used assuming there is a sand arch at the perforation tip if the perforation tunnel is long enough. However, no model considered the interaction of multiple arches when the shot density is high.

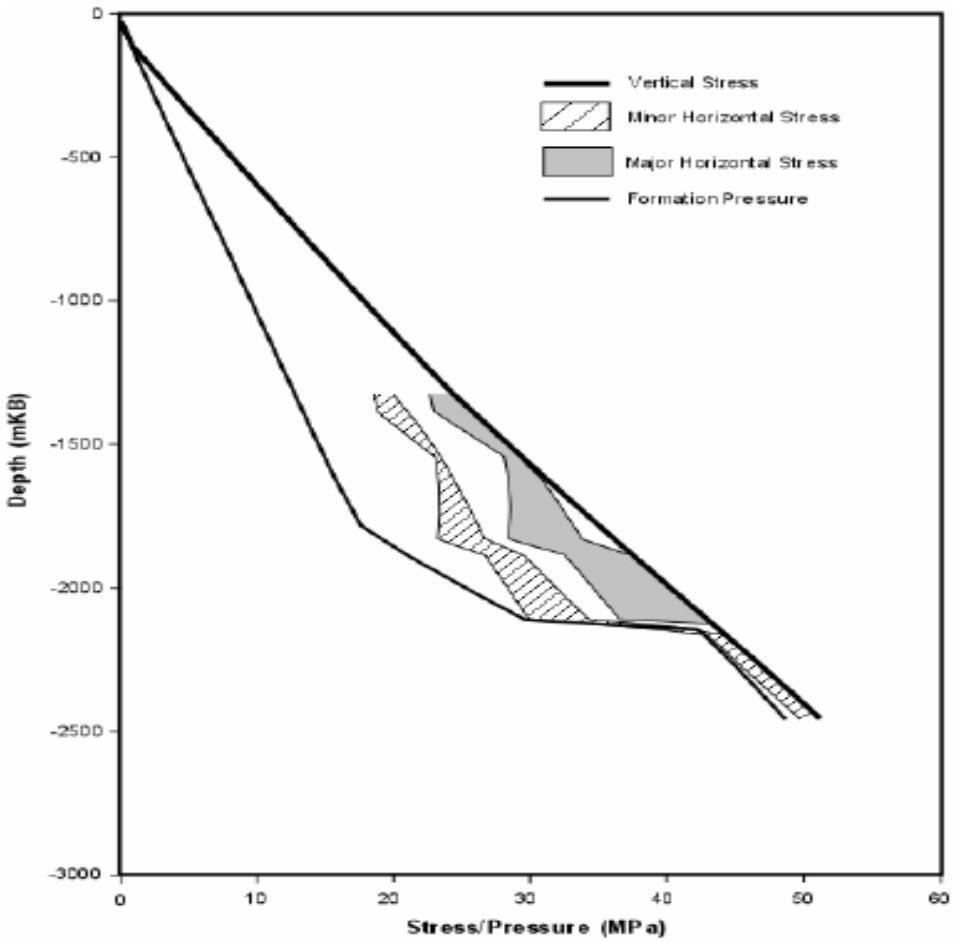

Figure 2.18. Horizontal and vertical stresses and formation pressure profiles. (Wu et al 2004)

2.11. Rock failure criterion from well logs

Relationships between porosity and the mechanical properties of porous media are well established: Wyllie et al. (1956, 1958) introduced a semi empirical relationship between porosity and acoustic velocity to the petroleum industry around the same time. Ryskewitch (1953) reported a relationship between porosity and strength of ceramics. Intuitively, porosity has long been assumed to be a major factor influencing the elasticity and strength of many rock types and has been observed by many researchers to be the best single predictor of strength in sedimentary rocks. Experimental work has revealed several empirical relationships between these properties for sandstones, carbonates, crystalline rocks and synthetic material (ceramics). The strength of sandstones has been reported to decrease in a nonlinear manner with increasing porosity. Similar relationships have been published for carbonates, crystalline rocks and ceramics. Dynamic elastic moduli have been found to decrease linearly with increasing

porosity for a range of silicate rocks and to decrease exponentially with increasing porosity for carbonates. Kamel et al (1991) found very good correlations between porosity determined from neutron and density logs with dynamic elastic moudli and acoustic velocities which they claimed was totally independent of lithology. Figures 2.19 illustrates the relationships which exist between porosity and the mechanical properties of sandstones and carbonates measured under uniaxial loading conditions. These plots have been constructed using data published in the petroleum engineering and rock mechanics literature. Variation in the experimental techniques of the individual laboratories possibly accounts for much of the scatter in the plots, however, it is readily apparent that relationships do exist between porosity and the elastic and rupture characteristics of these sedimentary rocks. Simple exponential functions of porosity, φ, of the general form:

$$M = A\exp(B\phi) \tag{19}$$

Where M is some mechanical property and A and B are constants have been favored by many researchers to describe this type of experimental data.

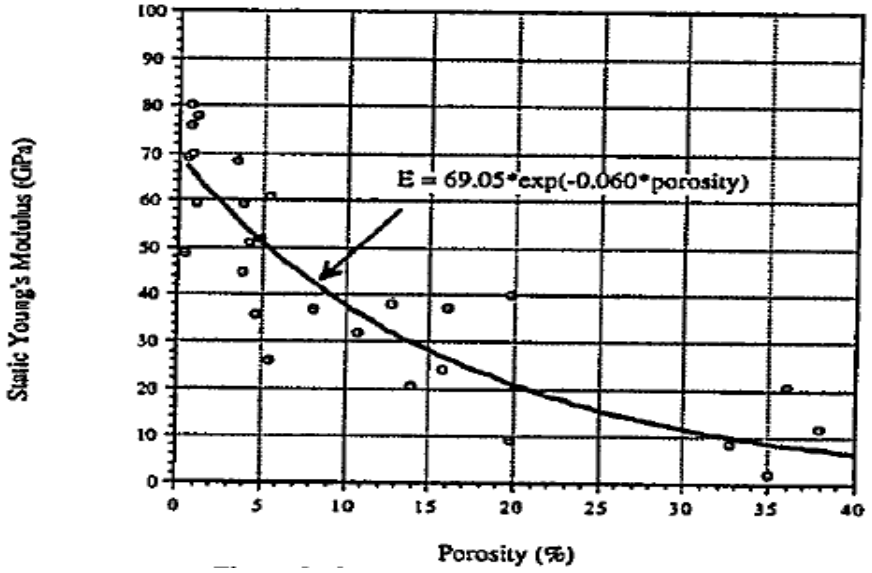

Figure 2.19. A relationship between Static Young Modulus and Porosity (Farquhar 1994)

2.12. Failure criteria relationships with porosity

Most of the work to date in this field has concentrated in relating porosity to absolute values of mechanical properties such as Young's modulus, and uniaxial compressive strength,. Both rock strength and elasticity are known to be stress sensitive properties. Both are observed to increase with increasing confining pressure. It has been shown that the porosity-strength relationship for

sandstones is preserved at elevated confining pressures. However, it would not be very practical to generate sufficient correlations to cover all possible confining stresses likely to be encountered. The development of the failure strength of rock as a friction of confining pressure can be represented by a relationship in terms of principal stresses termed a failure criterion. Several criteria have found popularity in petroleum related rock mechanics. The theoretical, linear Mohr-Coulomb criterion can be expressed in principal stress space as:

$$\sigma_1 = \sigma_0 + K\sigma_3 \tag{20}$$

Where σ_0 is the intercept which is taken to be an estimate of the uniaxial compressive strength and k is the triaxial stress factor which defines the rate of increase in axial stress at failure with confining pressure. The empirical Hock-Brown criterion is expressed as:

$$\sigma_1 = \sigma_3 + (m\sigma_0\sigma_3 + S\sigma_0{}^2)^{1/2} \tag{21}$$

Where the parameters m and s are constants (for intact rock s=l). Several researchers have noted that the influence of porosity extends to the development of rock strength with increasing confining pressure. This observation has prompted the search for correlations between porosity and the coefficients of the failure criteria.

The Mohr-Coulomb and Hock-Brown criteria were employed to fit experimental data generated on a range of sandstones .Axial stress at failure was determined .as a function of confining pressure from multi-failure state tests over a range of confining pressures from 6.9 MPa to 41.4 MPa. The porosity values reported were determined using Boyle's law Helium porosi-metery on unconfined samples.

The results show that the uniaxial compressive strength predicted from both failure criteria also yields good correlations with porosity. Both correlations indicate that uniaxial compressive strength decreases as porosity increases, although the correlation using-Gofrom the Hock-Brown criterion predicts lower values at the same porosity. The Hock-Brown criterion is generally accepted to provide a better estimate of the uniaxial compressive strength since it can better describe the non-linear increase in strength often observed in sedimentary rocks at low confining pressures. Significantly, both the triaxial stress factor from the Mohr-Coulomb criterion and the Hock-Brown parameter "m", which indicate the rate of increase in strength due to increasing confining pressure correlate with porosity (Figure 2.20). The strength of low porosity rocks increases at a greater rate with increasing confining pressure than in high porosity rocks, confirming the result observed in figure 2.20. For the porosity range encountered in our work on UK North Sea sandstones it is found that a simple linear

relationship adequately fits our data. The existence of these correlations with porosity measured in an unstressed state probably stems from the generally low stress sensitivity reported for porosity. These correlations demonstrate that the potential exists to predict the strength of sandstones over a practical range of confining pressures using porosity data. It is a simple matter to generate either a Mohr-Coulomb or Hock-Brown failure criterion for sandstone of a particular porosity.

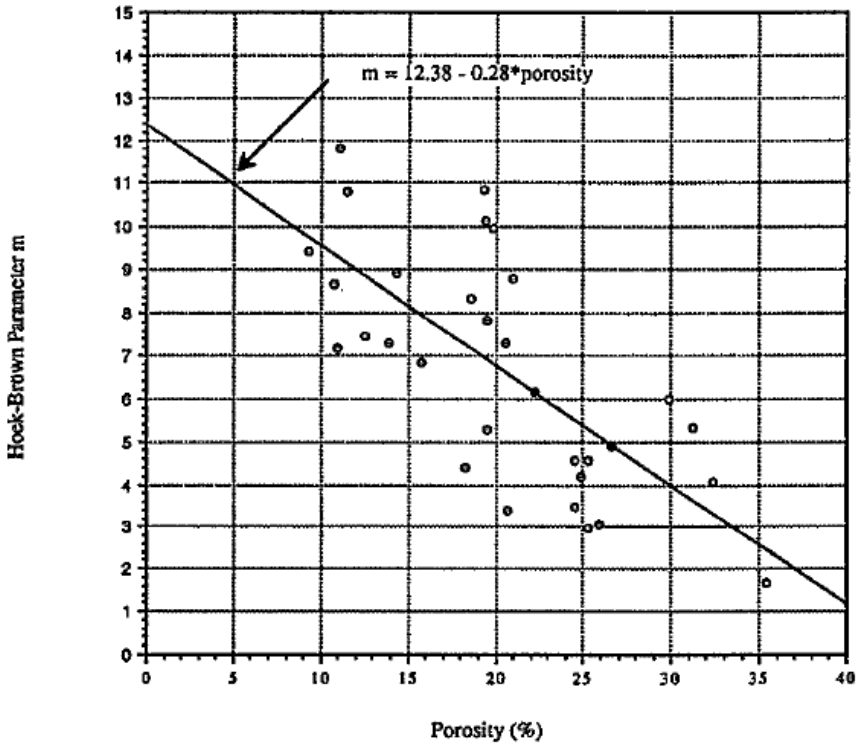

Figure 2.20. Linear correlations between porosity and the Hock-Brow failure criterion parameter for North Sea (UK) sandstone (Farquhar 1994)

2.13. The density log (overburden stress)

The density tools are active gamma ray tools that use the Compton scattering of gamma rays to measure the electron density of the formation. By appropriate lithology corrections, the electron density is converted to mass density with reasonable accuracy (Fjær et al. 2008). The density is useful for determining mechanical properties in two manners: first, the density is needed to convert from acoustic velocities to dynamic elastic moduli. Second, the density integrated over the vertical depth of the well is usually considered to give a good estimate of the vertical stress, at least in areas of low tectonic activity. In such areas, the vertical stress is

also considered to be a principal stress. When the density log is available, the problem of determining the full *in situ* stress field is then reduced to determining the magnitude and orientation of the horizontal stresses. However, the density log is rarely available in the first few hundred metres of a well. Then it is necessary to make estimates of the density to obtain the total vertical stress. In areas which have not been subjected to tectonic activity it is common to assume a density in the range 1.8–2.0 g/cm3. This bulk density corresponds to a porosity in the range 50–38% in a rock with a mineral density of 2.6 g/cm3.

Offshore Mid-Norway, bulk densities above 2 g/cm3 have been logged at very shallow depths. One plausible explanation to this unusually high density is that this area has also been exposed to ice loads. Thus the geological history should be taken into consideration when making estimates in non-logged intervals. Geotechnical data from site surveys may in some cases be available and provide additional information (Fjær et al. 2008).

2.14. Borehole logs (horizontal stress directions)

Determination of horizontal stress directions is based on the possibility of failure at the borehole wall which can be detected by borehole logging tools. To be detectable, the failures must occur in the period after drilling and prior to logging. In a vertical borehole which penetrates layers of significantly different horizontal stresses ($\sigma_H > \sigma_h$), two distinct failure modes can be detected: compressive and tensile failure. The directions of these two failure modes in an idealized situation are uniquely given by the directions of the two principal horizontal stresses, as illustrated in Figure.2.21 Compressive failure or shear failure will be induced in the direction parallel with the smallest horizontal stress (σ_h) if the well pressure is low enough to induce shear failure. This is commonly referred to as. Tensile failure will occur in the direction parallel with the largest horizontal stress (σ_H) if the well pressure is large enough to induce fracturing. Note that in situations with large variations in equivalent circulating density (ECD) of the drilling fluid it may be possible to observe both failure modes at the same depth. Once a failure has occurred on the borehole wall, it is tempting to try to back-calculate also stress magnitudes, especially the magnitude of the largest horizontal stress by using elastic theory and appropriate failure criteria. However, a number of assumptions are required for such analyses, rendering the results uncertain. Such estimates can at best be considered upper or lower bounds on the stress magnitudes. The large amount of information

that can be acquired by new tools, such as the Sonic Scanner, may eventually reduce some of the uncertainty, and allow for more reliable estimation of the *in situ* stresses.

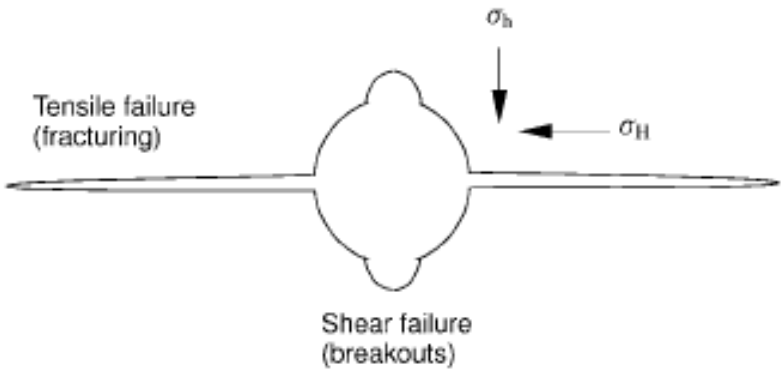

Figure 2.21. Illustration of directions for compressive and tensile failure around a vertical borehole (Fjær et al. 2008).

2.15. Caliper logs

The caliper log (four-arm) has commonly been used to estimate horizontal stress directions from breakout orientations. This tool provides two diameters of the borehole cross-section. To be able to identify stress induced borehole breakouts, a set of identification criteria has to be implemented. It is quoted here the criteria published by Plumb and Hickman (1985):

1. The tool is rotating above and below a borehole breakout.
2. The rotation stops over the breakout zone.
3. The borehole elongation is clearly seen in the log. One pair of pads must show a relatively sharp ascent and descent of the borehole diameter.
4. The smaller of the caliper readings is close to bit size, or if the smaller caliper reading is greater than bit size it should exhibit less variation than the larger caliper.
5. The direction of elongation should not consistently coincide with the high side of the borehole when the hole deviates from vertical.

2.16. Image logs

Image logs include both electrical (resistivity) and acoustical borehole imaging logs. The electrical image log operates with a large number of electrodes in contact with the formation, usually distributed over several pads on independent arms (four or six). This shallow electrical

investigation is well suited for investigation of fine structures like bedding planes, natural fractures and also drilling induced fractures.

The acoustical imaging tool (often referred to as borehole televiewer, BHTV) is based on reflection of acoustic waves from the borehole wall, recording the travel time and amplitude of the reflected pulses. The pulses are generated by a rapidly rotating piezo-electric crystal, thus creating a helix-shape logging path with a short distance between each revolution. This tool is best suited for detection of borehole breakouts, as drilling induced fractures do not create significant changes in borehole radius or reflectivity. Since these tools provide a full image of the borehole wall, it is possible to distinguish between stress induced breakouts and key seats. An example of an electrical borehole image log is shown in Figure 2.22. Examples of the use of image logs for determination of horizontal stress directions and magnitudes are given by Brudy (1998). If drilling induced fractures are found at an inclination with respect to the borehole axis, this implies that none of the principal stresses are parallel with the borehole axis. This can be the situation in an inclined borehole, or in a vertical borehole where the vertical stress is not a principal stress, as for instance close to faults (Brudy et al., 1997).

The only fully reliable method for determination of the smallest horizontal stress (σ_h) is to fracture the formation and record the pressure at which the fracture closes. This requires that the fracture has penetrated far enough into the formation to feel only the resistance of the in situ horizontal stress. In a vertical well this is achieved wellbore diameters away from the borehole. In a deviated wellbore, the fracture may have to travel farther away from the borehole, due to the twisting of the fracture and the principal stresses close to a deviated borehole. Determination of the largest horizontal stress (σ_H) is not trivial, and there is no straightforward method available for this. In an idealized linear elastic situation, the largest horizontal stress could be determined from a repeated fracture test. However, in practice, the fracture initiation pressure can vary considerably, rendering such an approach highly uncertain. Normally, the fracture initiation pressure is lower than predicted from linear elastic theory. This is probably the reason why field studies utilizing such an approach consistently predict a strike-slip stress regime ($\sigma_H > \sigma_v > \sigma_h$) (Fjær et al. 2008).

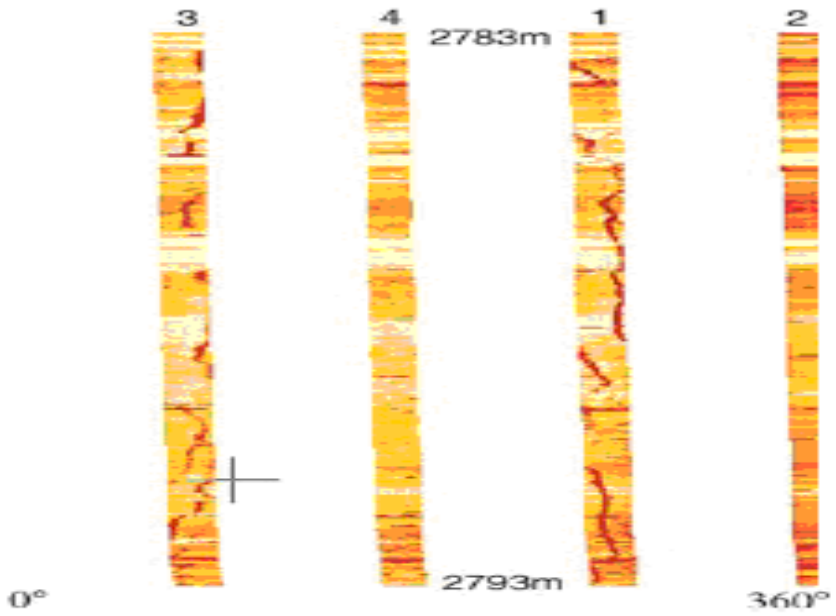

Figure 2.22. A resistivity image of a 10 m borehole wall section recorded with 4 arms in a North Sea well. Dark regions represent low resistivity. Intermittent dark traces on arm 1 and 3 indicate drilling induced fractures. Notice that these drilling induced fractures are 180° apart at the borehole wall and are not interconnected around the borehole like traces of natural fractures or bedding planes (Fjær et al. 2008).

2.17. Leak-off tests and extended leak-off tests

Leak-off tests (LOT) are performed during the drilling phase of a well, in the formation immediately below each casing shoe. The purpose of this test is to determine the maximum well pressure the new borehole section can sustain without fracturing and loss of drilling fluid. After a casing string has been cemented, the casing shoe is drilled out and a few metres of new formation is penetrated. A leak-off test is then performed by pressurizing this open-hole section. The principle of a leak-off test is shown in the first cycle in Figure 2.23.

The pressure in the hole is increased by pumping at a constant volume rate, typically 50–250 l/min. This yields a straight line of pressure versus volume (time), with the slope of the line given by the compressibility of the system (primarily the drilling fluid). The point where the pressure response starts to deviate from this straight line is defined as the leak-off point. This is actually the point where a fracture is starting to initiate. Normally, a leak off test is stopped shortly after this, even if the pressure continues to increase above the leak-off pressure.

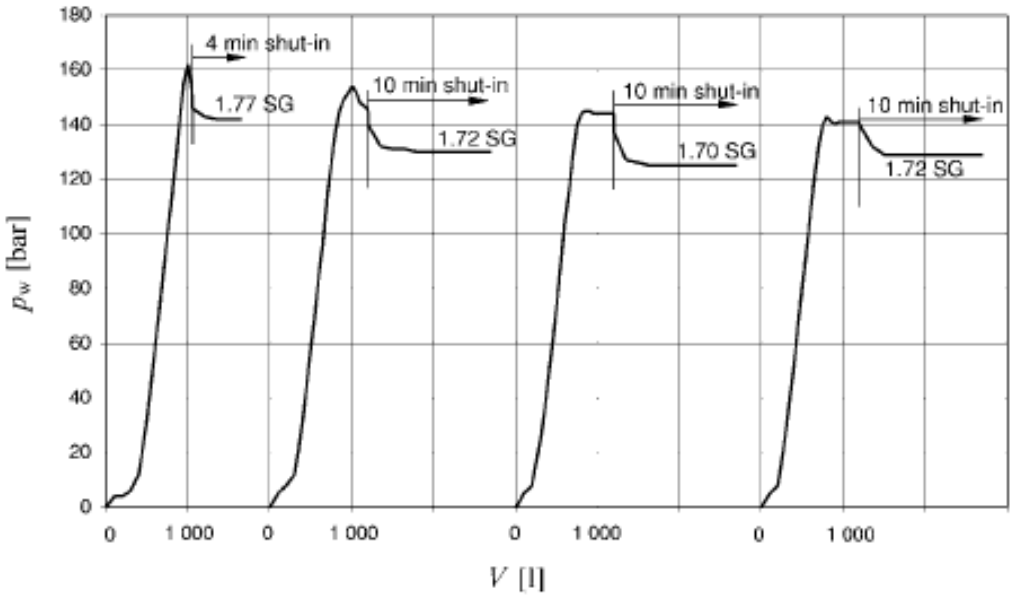

Figure 2.23. An example of a conventional leak-off test (first cycle) followed by three extended leak-off test cycles. The first cycle is shut in after 14 min of pumping at 75 L/min. The following cycles are shut in after 4.8 min of pumping at 250 l/min. The vertical lines indicate the shut-in point, after which the curves are a function of time, as indicated by the total shut-in period of each curve (Fjær et al. 2008).

The slope and the shape of the pressure versus volume line can be affected by a number of operational aspects (equipment performance, cement channels, pump rate etc.). For a discussion of how these factors may affect LOT-interpretation, see e.g. Postler (1997). It is also important to note that if the test is stopped shortly after the leak-off point, the generated fracture is very short, and even if the shut-in phase is recorded, this shut-in pressure may significantly overestimate the smallest horizontal stress. Examples given by Raaen and Brudy (2001) and Raaen et al. (2006) demonstrate that using the leak-off pressure as an estimate of the smallest horizontal stress can cause significant errors. At the very best, the smallest horizontal stress will be a lower bound to a large population of leak-off pressures (Addis et al., 1998).

To make the leak-off test applicable also to stress determination, modifications have to be made. This has lead to the so-called *extended leak-off* test (XLOT, ELOT) (e.g. Kunze and Steiger, 1992). The main difference from the standard leak-off test is that pumping continues well beyond the leak-off point and also beyond the breakdown pressure. To get a reliable stress estimate, pumping should continue until stable fracture growth is obtained (see third and fourth pump cycle of Figure 2.23). After shut-in, the shut-in/decline phase should be

recorded. As illustrated by Figure 2.23, it is recommended to pump several cycles to obtain repeatable test results.

Since these casing shoe tests are normally performed in low-permeability formations like shale, and with drilling mud in the hole, very little leak-off from the fracture is expected. This implies that fracture closure may be slow in a shut-in/decline test, resulting in an almost flat pressure versus time response. The pressure recorded as the closure pressure is thus still an upper bound estimate of the smallest horizontal stress. Better estimates can then be obtained by including a flow back phase in the test.

2.18. Mini-fracture tests

A mini-fracture test is a fracture test where a relatively small volume is injected (typically around 10 m^3). Small in this sense relates to conventional fracture stimulation jobs which commonly involve hundreds or even thousands of cubic metres. A mini-fracture test is normally run prior to a fracture stimulation job, in order to obtain values for fracturing pressure, closure pressure, fluid loss parameters etc. which are then used in the design of the fracturing treatment (e.g. Tan et al., 1990). This implies that mini-fracture tests are normally run in reservoir sections which require stimulation. Since the reservoir section may already be completed, it is not uncommon to run mini-fracture tests in cased and perforated wells. Again it is recommended to use a down hole pressure gauge to improve the accuracy. A typical fluid used in a mini-fracture test is 2% KCl brine. Gel may be added to reduce fluid loss and to make the test more similar to the main treatment.

2.19. Wireline tools

Wireline tools are also available for performing fracture tests in open holes (Kuhlman et al., 1993; Thiercelin et al., 1996; Desroches and Kurkjian, 1999). The basic principle here is to isolate a small section of the hole, typically 1 m, by inflating two rubber packers against the formation. A relatively small volume (typically less than 400 l) of fluid is used during pumping at rates in the range 1 l⁄min to 100 l⁄min. Due to the small volume, these tests are often referred to as *micro-fracture* tests. The pressure is measured with a downhole gauge.

As with other fracture tests, several cycles are usually performed. When run in an open borehole, good borehole quality is essential, i.e. a smooth hole surface and close to circular shape. Otherwise it will be problematic to obtain good sealing by the packers. To provide sealing, the packer pressure should exceed the pressure in the isolated interval. This implies

that under certain conditions a fracture will be generated first behind the packer. However, in low permeability formations, a fracture may be generated first behind the packer (sleeve fracturing). An alternative procedure in this situation is to do this deliberately and subsequently move the packers so that the generated fracture is within the isolated zone and then proceed as in a standard test (Desroches and Kurkjian, 1999). The azimuthal direction of the fracture and hence also the direction of the horizontal stresses can also be estimated, provided the test is performed in a vertical well. The method used to obtain the fracture direction varies somewhat with the type of tool, either using an imaging tool after fracturing or back calculating from measurements of borehole deformation during fracturing.

2.20. Empirical relations based on well data

Breckels and van Eekelen (1982) developed empirical correlations for estimation of the smallest horizontal stress as a function of depth. These relationships were based on hydraulic fracture data from different regions around the world. The relationships for the US Gulf Coast are:

$$\sigma_h = 0.0053D - 1.145 + 0.46(P_f - P_{fn})(\mathrm{D} < 3500\ m) \quad (22)$$

$$\sigma_h = 0.0264D - 31.47 + 0.46(P_f - P_{fn})(\mathrm{D} \geq 3500\ m) \quad (23)$$

In these equations, D is depth in meters, P_f is the pore pressure in MPa, P_{fn} is the *normal* pore pressure and σ_h is the total smallest horizontal stress in MPa. The last term in these relations reflect abnormal pore pressures. The predicted horizontal stress will hence reflect changes in the pore pressure gradient. It is argued that these relationships can be used with a fair degree of confidence also in other tectonically relaxed areas of the world such as the North Sea. Note that these relations were developed at zero or shallow water depths. These authors' experience is that the relation for depths down to 3500 m gives fairly good estimates in most parts of the North Sea (down to about 2500–3000 m), even at water depths up to approximately 300 m. As the water depth increases, predictions at shallow formation depth should be avoided. Thus these relations may provide reasonable estimates, but should only be considered as a first estimate and should always be checked and/or calibrated against proper test data from each field (Fjær et al. 2008).

Santana et al. (2001) presented the description of a methodology for the treatment of data aiming at the study of the correlations between sonic log and resistivity log. The

methodology, implemented through a simple computer program in a spreadsheet, shows efficiency in filtering background noise and revealing the trend between sonic slowness and resistivity data. The data are then used to generate correlations between resistivity and sonic slowness by a simple fitting-curve method. Although the final correlation is approximate in most of the analyzed wells, a good improvement is observed in most of them. The low value of Squared-R in some cases is a result of a great dispersion of data and remaining outlier data points, although a trend appears evident. Figure 2.24 shows the cross-plot obtained from original data (above) and for filtered data along with the fitted curve (below).The sonic log, resulting from a correlation derived from the presented methodology is invalid for zones affected by local changes in pore fluid salinity and the presence of hydrocarbon, since the response of resistivity log and sonic log are expected to deviate mutually. The zones of high or low porosity possibly affected by these effects must be evaluated individually, as the correlation will result in underestimated slowness in zones of hydrocarbon saturation. Crawford et al. (2010) provided sandstone-to-shale siliciclastic rocks including detailed petrographic and petrophysical characterization. The database comprises around 80 distinct lithologies and in excess of around 600 discrete triaxial compressive strength measurements. The database is subdivided into three generic lithotypes (classes displaying common petrophysical properties resulting from shared compositional and textural attribute) on the basis of fine-grained matrix volume "V_{matrix}" as determined from thin-section point counting: clean sandstones (arenites) $\leq$ 15% V_{matrix}; 15% V_{matrix} < shaly sandstones (wackes) <37% V_{matrix}; shales $\geq$ 37% V_{matrix}. The schematic diagram of this calcification is shown on Figure 2.25. The concept of the ideal packing model is illustrated schematically in Figure 2.26. Two possible geometrical configurations exist for this bimodal distribution: a framework of coarse grains with the intergranular space filled with the finer matrix particles; coarse grains entirely supported within a finer matrix. Note that a porosity minimum "φ_{min}" occurs when the volume of fine-grained particles is equal to the porosity of the coarse-grained component. When matrix volume fraction exceeds "φ_{min} "expansion of the coarse-grained framework is a geometric requirement in order to accommodate more matrix material. For such matrix supported. Additional predictive algorithms relate Mohr-Coulomb cohesion and internal friction angle to fractional porosity and total clay weight fraction from "XRD" analysis. All predictive algorithms generated from the mechanical strength database require only basic petrographic and petrophysical data as model input (porosity and fine-grained matrix or total

clay content) such that siliciclastic rock strength is potentially predictable from routine measurements on core or cuttings or remote sensing associated with geophysical wireline logs and seismic inversion. Log-based case studies from geographically and geologically diverse reservoir environments demonstrate that rock strength is predictable with sufficient accuracy to impact business decisions in data-sparse areas where no acoustic logs or associated core mechanical measurements are available for calibration purposes.

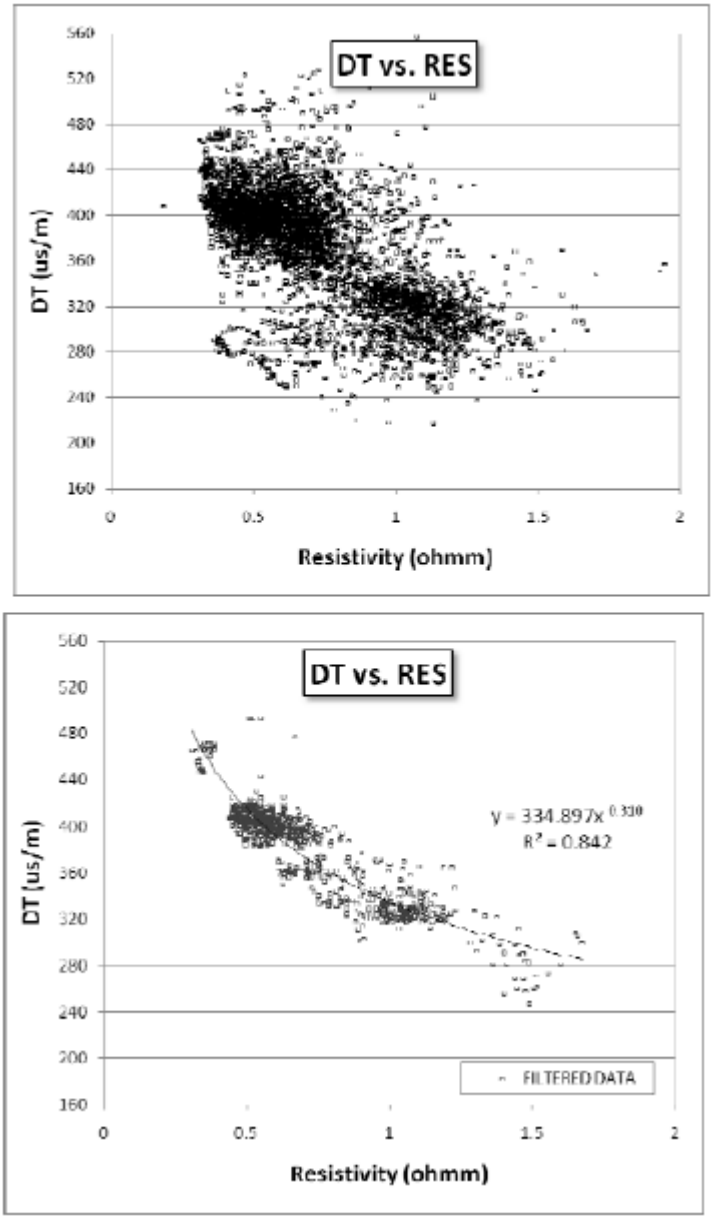

Figure 2.24. Cross-plot obtained original data (above) and for filtered data along with the fitted curve (below). The filtered data comprises all categories of rocks that together present a clear trend of co variation between logs (Santana et al. 2001)

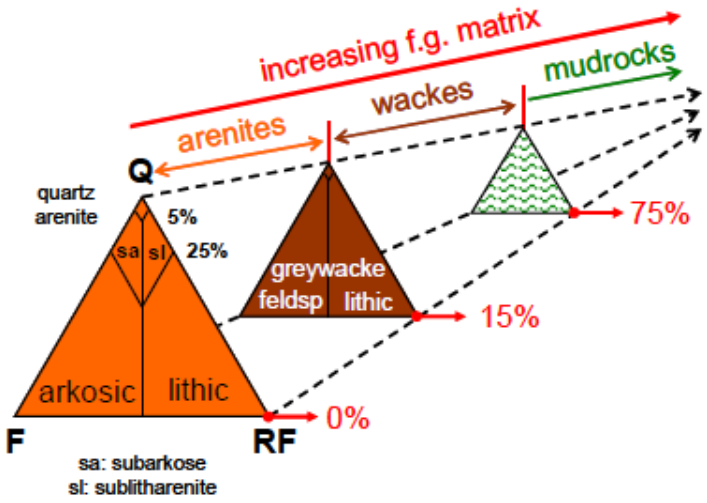

Figure 2.25. Petrographic classification of sandstones, Coarse-grained mineralogy: Q = quartz; F = feldspar; RF =rock fragments (Crawford et al. 2010)

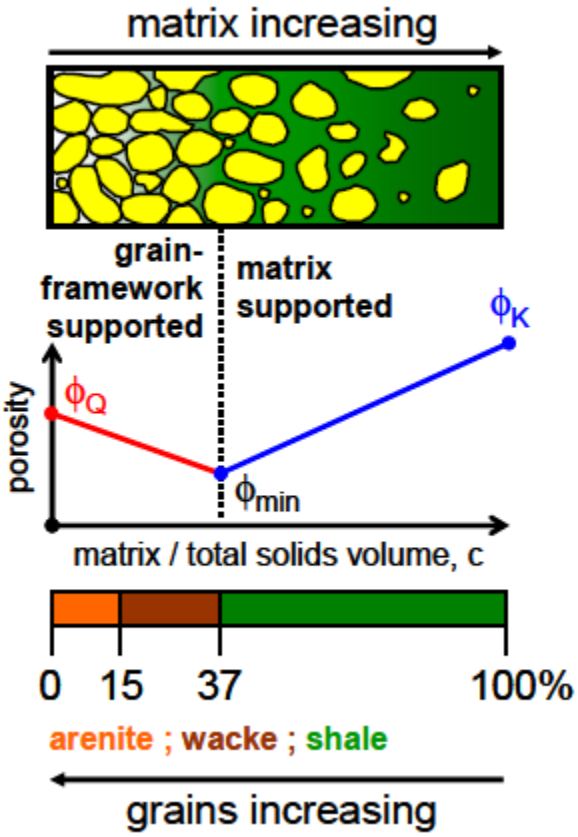

Figure 2.26. Schematic of geometrical packing for bimodal mixing of coarse and fine-grained particles (Crawford et al. 2010)

The bimodal mixing law therefore defines the transition from grain-framework supported wackes to matrix-supported shales at C =φ_Q and "critical porosity" concept can be used to further quantify this petrophysical threshold. Nur *et al* (1998) suggested that the critical porosity "fC" separates load bearing sediments at lower porosities $\varphi<\varphi_C$ from suspensions at higher porosities ($\varphi>\varphi_C$). Therefore, one might reasonably expect a maximum (critical) porosity $\varphi_C \sim 37\%$ for coarse-grains (equivalent to unconsolidated sand prior to fluidization) and a maximum (critical) porosity $\varphi_C \sim$ 60% for shales (equivalent to flocculated clays). The *maximum* matrix content for grain-framework supported microstructures is therefore c = 37% when $\varphi_C = \varphi_Q$ at which point $\varphi_{mix}= \varphi_{min} =$ 0.37*0.60 ~ 22%.

From the empirical observations depicted graphically in Figure 2.27, it is apparent that shear strength "τ" increases systematically with increasing porosity difference ($\varphi_C - \varphi$) for constant values of normal stress "σ_n" within a given generic lithotype. As the critical porosity fraction is fixed ($\varphi_C = 0.37$ for sandstones and $\varphi_C = 0.60$ for shales) it is evident that ambient porosity " φ_C " (increasing from right to left) has first order control on rock strength for a given value of normal stress, despite the fact that other petrographic parameters such as mineralogy, grain-size and cementation are also varying within each petrophysical subclass as illustrated by the thin-section photomicrographs in Figure 2.28. Interestingly, sandstones (arenites and wackes) appear to exhibit a transition in the rate of change of shear strength with porosity difference at an ambient porosity fraction, = 0.06, while shales exhibit a similar transition but at an ambient porosity fraction, $\varphi=$ 0.10.

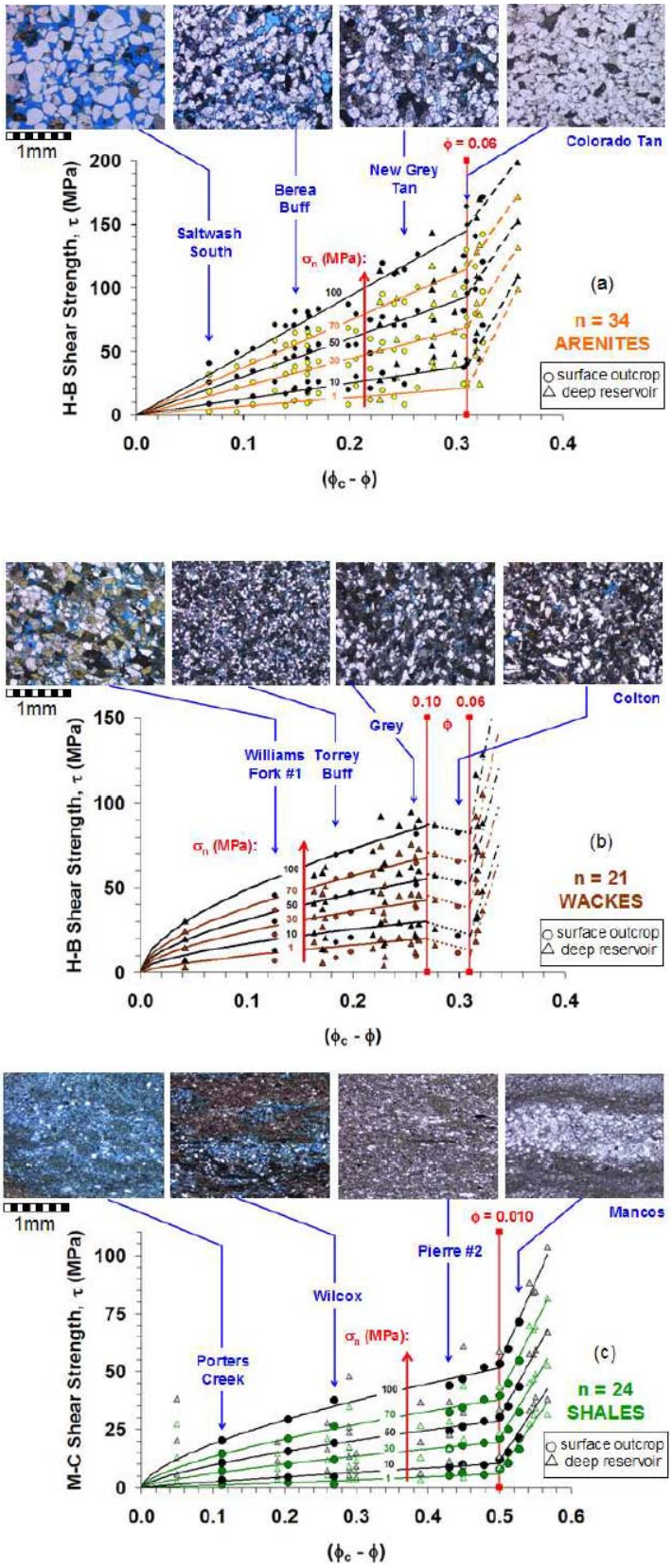

Figure 2.27. Shear strength "τ" versus porosity difference (critical minus ambient) for constant normal stress "sn" conditions: (a) n = 34 arenites; (b) n = 21 wackes; (c) n = 24 shales (Crawford et al. 2010)

CHAPTER III
Field Data and Characteristics

In this chapter the field data and geological characteristics of the two wells which have been used for petrophysical evaluation and geomechanical prediction of sand production, have been reviewed. The petrophysical evaluation has been done for well 7121/4-F-2 H which is located in Snøhvit field for disposal/reinjection of at least 1.2 Mill.Sm^3 CO_2/day into the Tubåen formation for the entire project life span. It has been shown in next chapter that the calculated critical well bore pressure based on petrophysical well logs and Mohr-Coulomb criterion is negative and sand production problem is unlikely in this well. The second well which has been used for prediction of sand production is Well 7122/7-3 and is located in Goliat field. The well has been drilled to appraise the hydrocarbon potential of the Early Jurassic / Late Triassic. In contrast to well 7121/4-F-2-H, the geomechanical evaluation of well logs demonstrates that the critical well bore pressure is positive and accordingly, sand production is expected. This is consistent to the real observations of production wells in Goliat field.

3.1. Snøhvit field

The Snøhvit Unit Area, including the Snøhvit, Albatross and Askeladd fields is located in the south western Barents Sea in the central part of the Hammerfest Basin, about 140 km northwest of Hammerfest (Figure 3.1).

In the period 1970-1991 several 2D seismic surveys were acquired in the Barents Sea. Exploration drilling started in 1980, when limited acreage in the south-western part of the Barents Sea was awarded to groups with Norwegian oil companies as operators. 17 exploration wells have been drilled in the Snøhvit Area (Figure 3.1). The Askeladd Field (gas) was discovered in 1981 followed by the discovery of the Albatross Field (gas) in 1982. In 1983 3D seismic survey was acquired over the Askeladd field. The Snøhvit Field was discovered and tested for both oil and gas in 1984. In the Snøhvit Field discovery well 7121/4-1, the gas-oil or oil-water contacts could not be determined in certainty, mainly because the oil was located in a shaly lithology in the lower part of the Nordmela Formation. In the second Snøhvit well, 7120/6-1, the oil is situated in the best part of the Stø Formation and the oil-water contact is interpreted at 2417.3m MSL, and the gas-oil contact at 2402.8m MSL. These give an oil column of 14.5 meters. The main objective of the eastern most well,

7121/5-1, in the Snøhvit Field was to test for additional oil below the oil water contact found previously. The OWC was found close to the top of the Nordmela Formation (2418.2m) and the GOC was determined to be at 2404.7m MSL from static pressure measurements and log analysis. This gives an oil column of 13.5 meters. The two Snøhvit appraisal wells were successful in testing the huge gas cap, whereas the oil leg tests gave disappointingly low oil rates. The eastern and north-western parts of the field were delineated by these to wells. In the western part of the Snøhvit Field there is a gas chimney area where the seismic data are badly affected by gas. The seismic reflectors sag and loose continuity, so the western extent of the field has not been well defined. A structure west of the gas chimney was tested by well 7120/5-1 in 1985, but it was dry. Two other exploration wells were on two separate structures north and north-east of the Snøhvit Field. Well 7121/4-2, located on the Snøhvit Nord structure proved a 37.4 meter thick gas column in the Stø Formation and well 7121/5-2, located on the Beta structure proved a 32 meter thick gas-column and a 3 meter thick oil column in the Stø Formation. In 1997 3D seismic surveys were acquired over the Snøhvit Field and the Delta structure. The latest exploration well in the area, 7121/5-3, was drilled in 2001 on the Delta structure. The well proved dry with only residual hydrocarbons in the reservoirs of the Tubåen and Stø Formations (Snøhvit Statoil report No. RA-SNØ-00126).

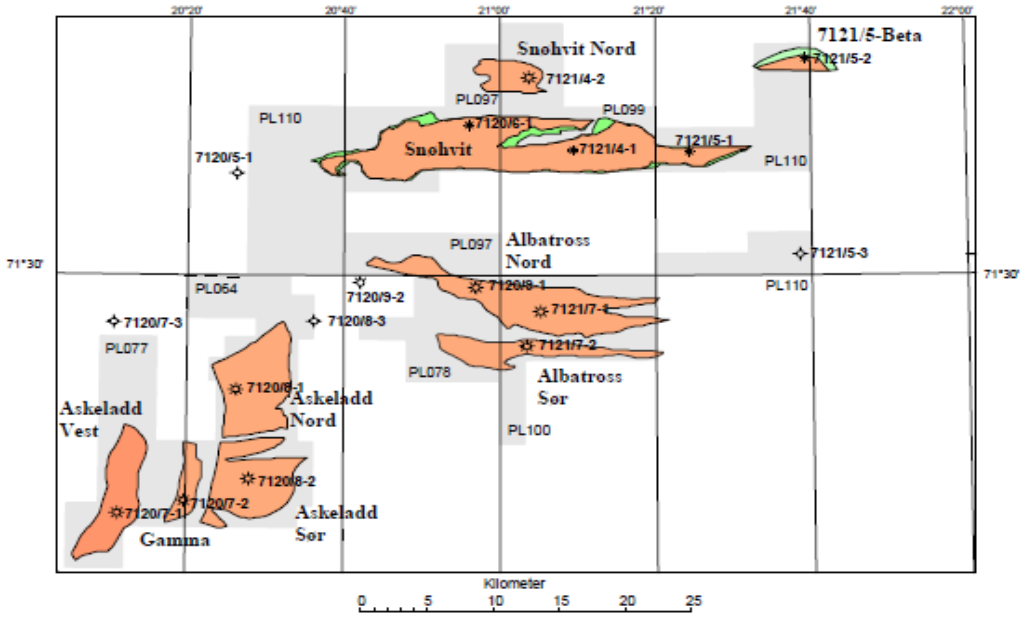

Figure 3.1. Snøhvit Unit with exploration wells (Snøhvit Statoil report No. RA-SNØ-00126).

3.1.1 Regional geology

The structural elements of Snøhvit Unit Area in the Hammerfest Basin are the result of the late Kimmerian tectonic phase its present day geometry reflects its structural evolution where continued tectonics and reactivation of older structural elements has occurred. The main subsidence in the area took place during the Cretaceous, whereas large parts of the region were uplifted during Tertiary times. The Hammerfest, Nordkapp and Bjørnøya Basins form the basin province of the Barents Shelf complementing the Svalbard Platform to the north. The Hammerfest Basin is an east-north-east to west-southwest trending, symmetrical structure that widens and deepens westwards and is bordered to the north and south by the *Southern Loppa High* and the *Troms Finnmark Fault* complexes respectively (Figure 3.2).The intersection and reactivation of early basement related faults is characteristic of the basin. The post-Caledonian development of the south-western part of the Barents Sea probably started with deposition of terrestrial sediments in fault bounded extensional basins (Snøhvit Statoil report No. RA-SNØ-00126).

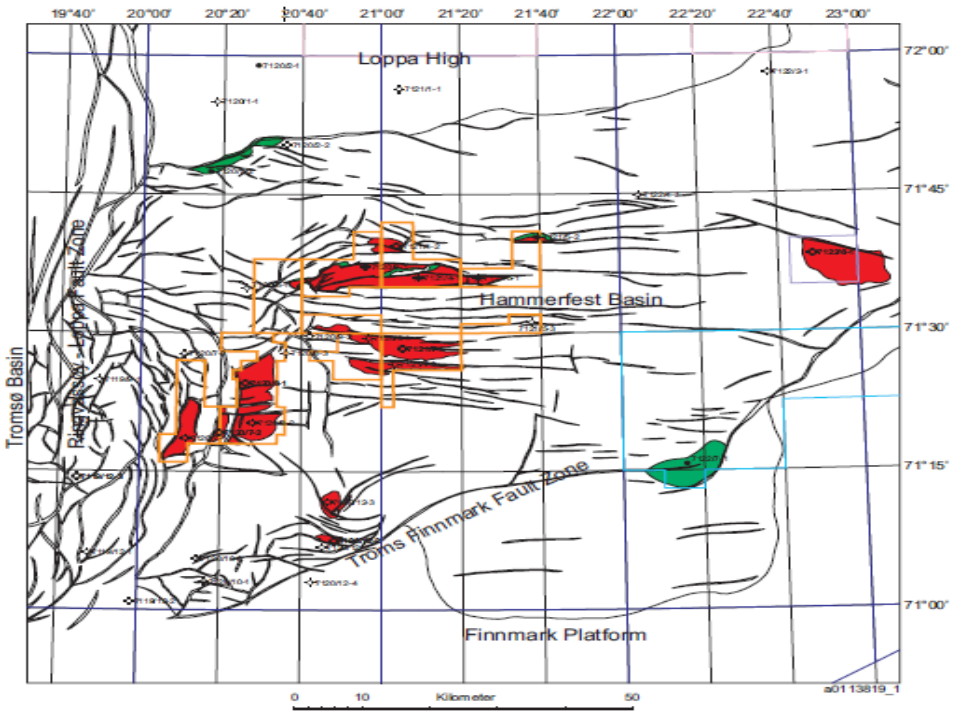

Figure 3.2. Structural setting of the Snøhvit Area in the Barents Sea
(Snøhvit Statoil report No. RA-SNØ-00126)

After post-Caledonian rifting, in a north-south system, a thick salt sequence of Permian age was deposited in the *paleo-Troms Basin* and the *paleo-Loppa High* was partly eroded along

the eastern margin of the basin. Marginal carbonates and clastics were deposited in the Hammerfest Basin. Fault activity ceased during Middle Permian and the entire area became part of an intracratonic basin until the Middle Jurassic. The only indication of structural movement is an Early Triassic unconformity on the *Loppa High*. The Late Triassic to Middle Jurassic was a tectonically quiet period, and the sand prone *Realgrunnen Group* was deposited (Figure 3.3). The *Realgrunnen Group* constitutes sediments associated with tectonic subsidence, and thickens north-westwards, probably infilling a more extensive basin than is evident now. This deposition culminated in major transgressions and the initiation of a rift phase in the area.

In Middle Jurassic to the Early Barremian times, the Hammerfest Basin was affected by doming. The uplift of the central part of the basin created a series of east-west oriented faults. A majority of these faults dip toward the basin axis, where horsts and grabens formed along the crest of the dome. A major hiatus and eventually marine transgression defines the base of the rift phase sedimentation comprising the argillaceous *Teistengrunnen* and *Nordvestbanken Groups*. Extension and subsequent collapse of the uplifted area created E-W oriented fault grabens forming the Albatross, Askeladd, Snøhvit and related structures. The main subsidence of the basin occurred along the northern and southern margins during the Cretaceous. The Nordvestbanken *Group* was succeeded by the *Nygrunnen Group* in the Late Cretaceous (Campanian), bounded by basal and upper unconformities. Cretaceous sedimentation continued until uplift and erosion occurred in Maastrichtian times. During the late Paleocene to early Eocene, subsidence and argillaceous sediments of the Sotbakken Group were deposited in the Hammerfest Basin in the western part of the Barents Sea, whereas uplift and erosion affected the area after the early Eocene opening of the Norwegian-Greenland Sea. The basin was subjected to external structural events such as initial Atlantic sea floor spreading, which temporarily halted sedimentation in the Eocene. Eocene to Oligocene deposition was finally terminated as a passive margin that was created after separation of Greenland and Svalbard in mid Oligocene times. The Hammerfest Basin was uplifted and deeply eroded and provided clastic sediments to the basins that were developing to the west. Tertiary tectonism caused fault activation along old lineaments.

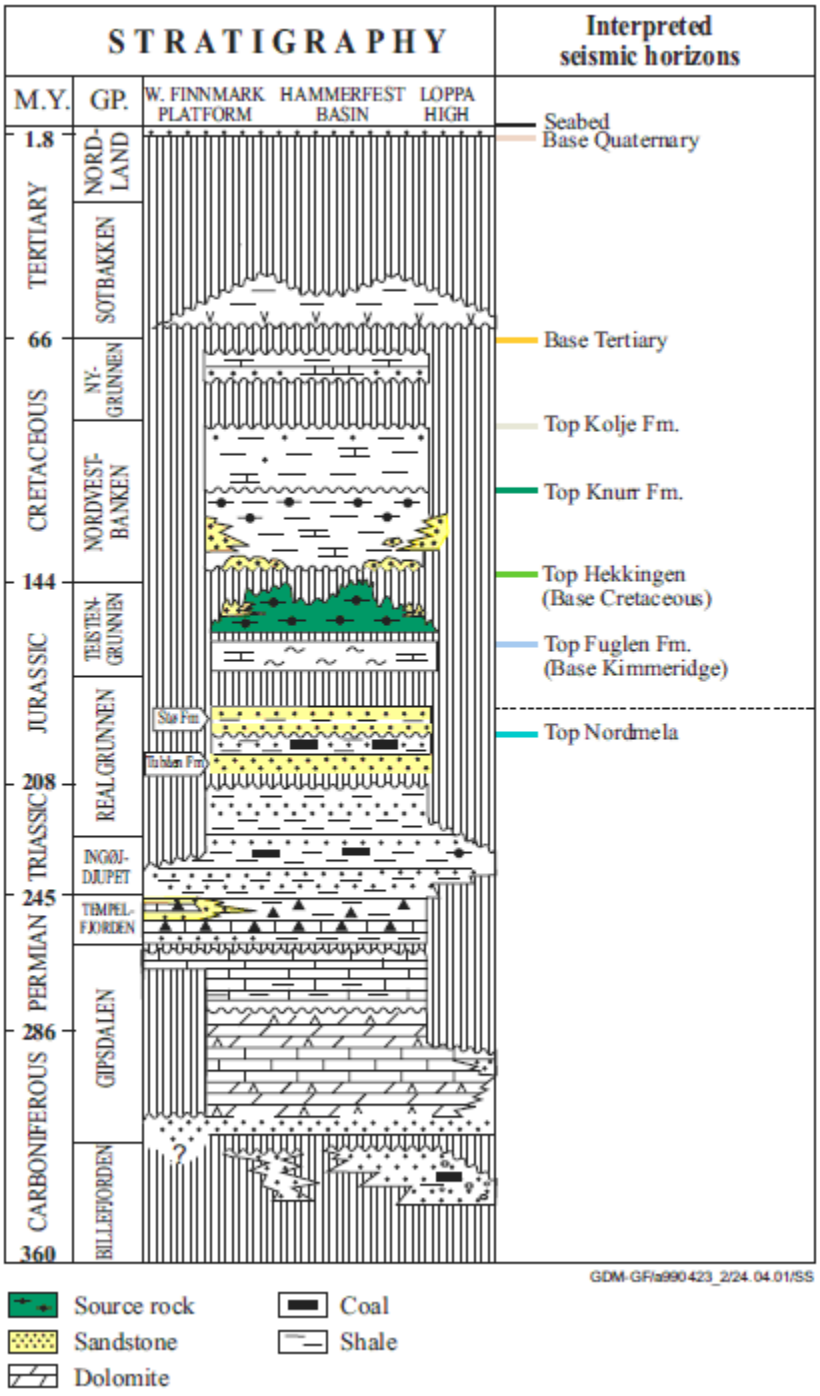

Figure 3.3. Stratigraphy for the Snøhvit Area and the Hammerfest Basin

(Snøhvit Statoil report No. RA-SNØ-00126)

Several observations point to the conclusion that much of the sequences in the Hammerfest Basin has been buried deeper than its present depths suggest; e.g. higher shale densities than expected for today`s depth, the sonic log transit time is generally lower than in the North Sea, reduction in porosity due to compaction is relatively large and studies of vitrinite reflectance

also indicate deeper burial. Collectively these observations strongly indicate that the Snøhvit Area has been buried approximately 1000m deeper than it is today.

3.1.2 Stratigraphy

The lithostratigraphic nomenclature of the Snøhvit Area (Figure 3.3) follows the official lithostratigraphic scheme defined in the NPD-Bulletin no 4, 1988. One of the wells from the Snøhvit Field (7121/5-1) is used as a reference well/type section in the NPD-Bulletin for the log definition of the Late Triassic - Middle Jurassic lithostratigraphic formations named Fruholmen, Tubåen, Nordmela and Stø of the Realgrunnen Group.

The Middle and Upper Triassic (*Ingøydjupet Group*) strata are characterised by a lower sequence of interbedded shales and sandstones that occasionally are carbonaceous and contain coal fragments, overlain by a shaly and silty unit that has increasingly more interbedded sandstones upward. These sediments are interpreted as having been deposited in a deltaic environment. During the Late Triassic to Middle Jurassic thick sand dominated clastic sequences of the *Realgrunnen Group* were deposited across the Hammerfest Basin. The Lower to Middle Jurassic strata consists mainly of sandstones interbedded with thin shale layers, deposited in a shallow marine to coastal plain environment with fluctuating coastlines. The lower part, the *Tubåen Formation*, has thick sandstone bodies with thin shale beds, which in part are carbonaceous and may contain coal layers. The conformably overlying *Nordmela Formation* has silty shales and very finegrained sandstones in the lower part, and finegrained sandstones in the upper part. The fine- to coarse-grained sandstones of the Stø Formation were deposited above the *Nordmela Formation*. There is a major hiatus between the Middle and Upper Jurassic, and Bathonian strata are missing in five of the six wells drilled in the Snøhvit Field area.

Above the hiatus, the Upper Jurassic consists of shales (the Fuglen and Hekkingen Formations) that are very organic-rich in the upper part. The depositional environment was a marine shelf with anaerobic bottom water conditions. The organic-rich shales also form the cap rock for the Snøhvit reservoirs.

There is a hiatus between the Upper Jurassic and the Lower Cretaceous strata and another between the Lower and Upper Cretaceous rock units. The Cretaceous strata consist mainly of claystones with thin sandstone and siltstone stringers in the middle part. Limestone and dolomite stringers mainly occur in the lower and middle parts, whereas limestone

interbedded with claystones are found in the upper part. Traces of tuff and tuffaceous claystones occur in the middle and uppermost parts of the sequence. The 1200m Cretaceous sediments were deposited in a marine shelf environment. There is another hiatus between the Cretaceous and the Tertiary strata.

The 600m of Paleocene and Eocene claystones contains stringers of sand, siltstone, limestone and dolomite and traces of tuff occur at the base of the Tertiary sequence. The depositional environment was a marine shelf with restricted bottom water conditions. There is a major hiatus in the upper part of the Tertiary sequence, and the Pliocene to Pleistocene sequence is represented by only 100m of soft claystones. A detailed high resolution biostratigraphic study of the Jurassic interval of six wells in the Snøhvit Area was reported by Statoil in 2000.

3.1.3 Reservoir zonation

Based on biostratigraphy, sedimentology and petrophysical characteristics, a common reservoir zonations and correlation has been established for all wells in the Snøhvit Area (Figure 3.4). This correlation approach is supported by the flat nature of the seismic reflectors, the expected lateral correlatability of the marginal marine sediments of the Nordmela and Stø Formations and the lack of active faulting during deposition.

3.1.4. Sedimentology and petrology

The purpose of this section is to review the sedimentological and stratigraphical aspects of the various fields in the Snøhvit Area. The hydrocarbon bearing reservoirs in the Snøhvit Area are assigned to the Tubåen, the Nordmela and the Stø Formations, with the Fuglen and the Hekkingen Formations as the cap rock. A sedimentological core description of the Nordmela and Stø Formations is given in Figure 3.4. Petrographical analyses show that the Stø Formation comprises quartz arenites, with detrital components limited to traces of clay clasts, muscovite, plant fragments, the heavy minerals and trace amounts of detrital clay. Quartz overgrowths form the volumetrically important diagenetic phase, although traces of diagenetic kaolinite and pyrite, minor patchy dolomite have been identified. Quartz cement volumes range from 6% to almost 25%, probably including a few per cent inherited quartz overgrowths from older sandstones. Porosities are generally in the range 15-22%. Grain sizes are between 0.15mm and 0.37mm, and practically no grain coatings are present in the reservoir sandstones. Measured homogenization temperatures (Th) for aqueous inclusions

within quartz overgrowths located close to the boundaries between quartz clasts and overgrowths are dominantly in the range 80-106 ºC. Such homogenization temperatures suggest a maximum burial depth of up to 3500m. The only significant internal source of quartz cement within the sandstones is dissolution of quartz clasts at stylolites evolved from clay-rich or organic-rich clay laminae, although interpenetration of individual quartz grains has also been identified. The connection between stylolite content and clay-rich laminae, suggests that quartz cementation in the Stø (and Nordmela) Formation is a sedimentologic issue. Some stylolites are very thin and laterally restricted and can be difficult to detect macroscopically. Laterally continuous stylolites are inclined to influence on the hydrocarbon flow through the reservoir.

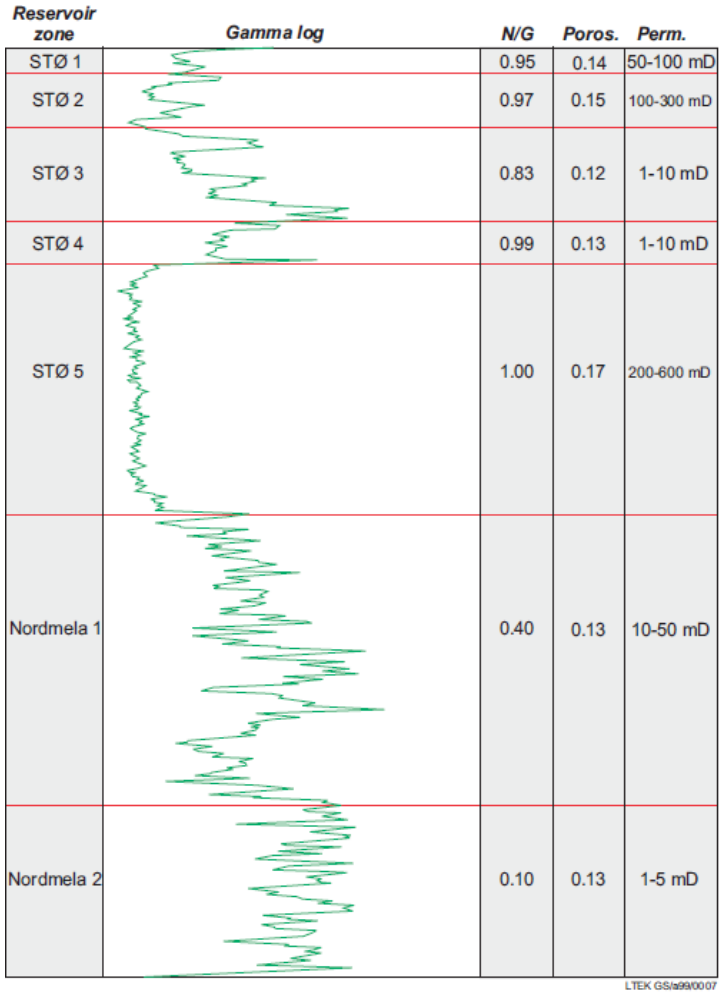

Figure 3.4 Snøhvit Area - reservoir zonation and typical rock properties. (Snøhvit Statoil report No. RA-SNØ-00126)

3.2. Goliat field

Goliat was discovered in 2000 and is located 50 kilometers southeast of Snøhvit in the Barents Sea. The Goliat structure is located on the crestal part of a major northeast-southwest trending roll-over anticline situated in the southeastern part of the Hammerfest Basin, along the Troms-Finmark Fault. The sea depth in the area is 360 – 420 metres. Goliat will be developed with eight subsea templates with a total of 32 well slots. These will be tied to a circular, fixed floating production facility with an integrated storage and loading system. The reservoir comprises Triassic sandstones. There is oil and a thin gas cap in the Kapp Toscana Group and the Kobbe Formation. The reservoir lies at a depth of 1 100 metres, and the quality is variable. Well 7122/7-3 was drilled on the Goliat Field, which is located approximately 55 km to the south-east of the Snøhvit Field. The primary purpose of the well was to appraise the hydrocarbon potential of the Early Jurassic / Late Triassic (the 7122/7-1 Goliat Discovery). The secondary purpose was to test the potential throughout the Triassic and Late Permian. The well was drilled with seawater/high viscous sweeps with pre-hydrated bentonite mud down to 538 m and with K/Na Format Polymer mud from 538 m to TD. The top of different formations for this well is shown in Table 3.1.

Table 3.1.Top of different formations for Well 7122/7-3 in Goliat field

Top depth [m]	Name
368	NORDLAND GP
634	NYGRUNNEN GP
634	KVITING FM
650	ADVENTDALEN GP
650	KOLMULE FM
865	KOLJE FM
960	KNURR FM
1018	HEKKINGEN FM
1073	FUGLEN FM
1087	KAPP TOSCANA GP
1087	TUBÅEN FM
1180	SNADD FM
1808	SASSENDALEN GP
1808	KOBBE FM
2044	KLAPPMYSS FM
2212	HAVERT FM
2595	TEMPELFJORDEN GP

The top of the Tubåen reservoir was found at 1087 m, 5 m deeper than prognosis. The reservoir had a gas cap with a GOC at 1145.6 m and oil below. No OWC was found. Top Snadd Formation reservoir was encountered at 1180 m, 23 m shallower than prognosis. The reservoir was oil bearing with a true OWC at 1199.5 m and was in a pressure regime different from the Tubåen reservoir pressure. The third reservoir was found in the Kobbe Formation at 1808 m, 29 m shallower than the prognosis. The reservoir was oil bearing. Oil was confirmed down to 1875.3 m by MDT fluid scanning, and the oil water contact was interpreted to be at 1878 m based on intersection between oil and water gradients.

The Kobbe Formation oil differs from the upper Tubåen and Snadd oils, which are geochemically very similar. The Kobbe oil is not biodegraded while the upper oil reservoirs are slightly biodegraded (removal of C8 – C15 n-alkanes, but intact C15+ nalkanes). Other geochemical differences, such as a very light stable carbon isotope composition in the Kobbe oil compared to the upper oils, indicate that the Kobbe oil and the upper oils have different source rocks. Seven cores were cored in the well. Cores 1 and 2 were cut from 1082 to 1104 from the Late Jurassic Fuglen Formation and into the Late Triassic Kap Toscana Group, core 3 was cut from 1146.5 to 1156 m in the Kap Toscana Group, core 4 was cut from 1187 to 1192 m in the Late Triassic Snadd Formation, cores 5 and 6 were cut from 1812 to 1836m in the Middle Triassic Kobbe Formation, and core 7 was cut from 2519 to 2521 m in the Early Triassic Havert Formation MDT fluid samples were taken at 1095.3 m (Tubåen Formation ; gas), 1148.5 m (Tubåen Formation; oil), 1202.1 m (Snadd Formation; water), 1812 m (Kobbe Formation; oil), 1874.5 m (Kobbe Formation; oil), and at 1931.2 m (Kobbe Formation; water). The well was permanently abandoned on 8 January 2006 as an oil and gas appraisal and discovery well.

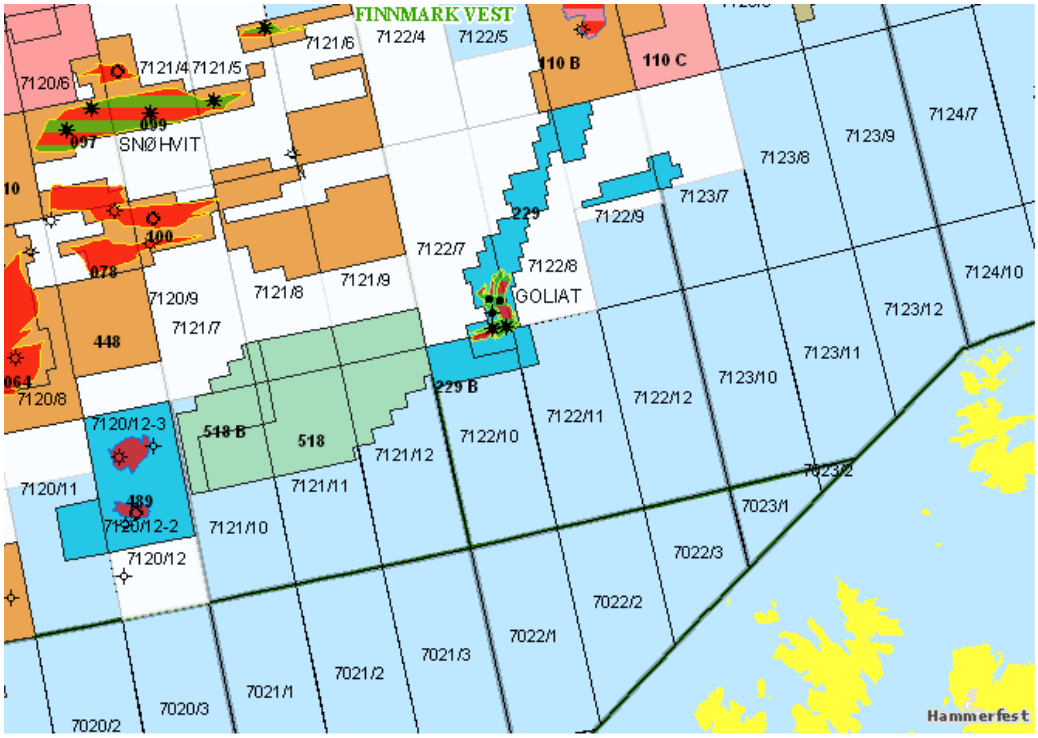

Figure 3.5. Goliat unit with exploration wells (NPD)

CHAPTER IV
Result and Discussion

4.1. Petrophysical evaluation of well 7121/4-F-2-H

The petrophysical evaluation of Well 7121/4-F-2 H has been perfumed using Interactive Petrophysical version 3.4 from Schlumberger. The quality of pure well log data is assessed based on calliper log and consistency between density, neutron, sonic, resistivity and gamma ray logs. The well log data are not affected by well bore conditions (wash out) and the quality are good. The general well and mud data properties of well 7121/4-F-2 H is illustrated in Table 4.1. From this table, the density of mud, mud and mud filtrate resistivity and bottom hole temperature have been imported to the petrophysical model. Required data for reservoir zonation and water saturation calculation of different models are extracted from Table 4.2 and 4.3 respectively (Statoil Report No. 07Y97*103272).

The temperature gradient is taken from the Snøhvit support documentation provided by Statoil giving a gradient of

$$T\ (C^{o}) = 0.0269 * \text{TVD MSL (m)} + 28.1 \qquad (4.1)$$

4.1.1. Shale volume

Evaluation of shale volume is estimated from gamma ray (GR), neutron log (NPHI) and density (RHOB) log. Shale and sand values are determined by visual inspection of the logs and by neutron- density cross plot. Shale volume (VSH) is estimated by the minimum of Gamma ray and Density-Neutron, based on clean sand and shale picks.

$$VSH = MIN\left\{\frac{NPHI_{env} - \phi \cdot H_f}{\phi_{shale}}, \frac{GR - GR_{sand}}{GR_{shale} - GR_{sand}}\right\} \qquad (4.2)$$

GR is the actual reading, while GR_{sand} and GR_{shale} is estimated reading in clean sand and shale. The Density-Neutron shale volume is estimated from ϕ_{shale} as the estimated total porosity in shales and H_f as the hydrogen index. The input parameters for GR_{sand}, GR_{shale} are 15 gAPI and 155 gAPI respectively for whole interval.

4.1.2. Porosity

An effective porosity model has been used for the evaluation. The bulk density has been used from porosity log as Eq. (4.3).

$$\phi_{Density} = \frac{RHOB_{Matix} - RHOB}{RHOB_{Matix} - RHOB_{Fluid}} - VSH \cdot \frac{RHOB_{Matix} - RHOB_{Shale}}{RHOB_{Matix} - RHOB_{Fluid}} \tag{4.3}$$

In this equation, VSH is the shale volume, $RHOB_{Matrix}$ represents the matrix density, RHOB represents the bulk density from log and $RHOB_{Fluid}$ represents the fluid density. $RHOB_{Shale}$ is found from VSH/RHOB cross plotting. Fluid density is calculated in an iterative process using, pressure, temperature, mud filtrate salinity, hydrocarbon density and calculated flushed zone saturation as inputs, given by:

$$\rho_{Fluid} = S_{XO} \cdot \rho_{Mudfiltrate} + (1 - S_{XO}) \cdot \rho_{Hydrocarbon} \tag{4.4}$$

S_{XO} describes the invaded zone water saturation. The density of mud filtrate is determined from chart below.

4.1.3. Saturation

The water saturation has been calculated using a standard Archie relation, given by:

$$SW = \left(\frac{a}{(\phi)^m} \cdot \frac{R_w}{R_t} \right)^{\left(\frac{1}{n}\right)} \tag{4.5}$$

In this equation, Φ describes the porosity, a is the lithology factor and is taken as 0.23, n is the saturation exponent and is taken as 2.64, m is the cementation exponent and is taken as 1.95, Rw is the formation water resistivity and Rt is the true formation resistivity. The formation water resistivity is calculated using a formation water salinity of 144.000 ppm NaCl. The resistivity is 0.068 ohm.m at 15.6 deg C. The same lithology factor, saturation and cementation exponents are taken from the Snøhvit development wells (a= 0.23, m=2.64, n=1.95).

Table 4.1.General well and mud data, 7121/4-F-2 H

SNØHVIT	7121/4-F-2 H	19.12.2004 – 10.02.2005

WELL DATA	
Well Type	Injection Well
Block	7121/4
Template Slot	F-2 H
Rig	Polar Pioneer
Slot centre, UTM East	501 998.41 m E
Slot centre, UTM North	7 945 754.16 m N
Geo East	21° 03` 24.36`` E
Geo North	71° 36` 39.41`` N
RKB	23 m
Water Depth	318 m
Max Deviation @ Depth	27,29 ° 2638.11 m MD
Average Dev in Reservoir	25 °
Average Azim in Reservoir	288°
TD driller	2908 m MD / 2793.65 m TVD RKB
TD logger	-
Csg shoe Driller	2482 m MD / RT 2480 m TVD RT
Csg shoe Logger	-
Csg	9.625

MUD DATA	
Type	Glydril WBM
Density	1.28 g/cm3
Viscosity	70 s
Fluid Loss [HTHP]	2.8 cm3
pH	8
Other, KCl	155.0
Ca^{++}	360.0
Mg^{++}	0.0
Solids	3.7 vol %
Rm	0.067 ohm.m @ 19 C^0
Rmf	0.056 ohm.m @ 17 C^0

Bottom hole Temperature	
T [deg C]	86
Depth	2894 m MD
Time	24.01.2005 16:31

Table 4.2. Formation tops

7121/4-F-2 H	Prognose				Actual			Diff
	Depth	Uncertainty	Depth	Thick.	Depth	Depth	Depth	
Formation and/or Seismic Marker	m TVD MSL	m(+/-)	m TVD RT	m TVD	m TVD MSL	m TVD RT	m MD RT	m TVD
Seabed	318	+/- 1 m	341					
Kviting					1018.04	1041.04	1047.94	
Kolmule					1052.43	1075.43	1082.73	
Kolje	1829	+/-20 m	1852	349	1830.43	1853.43	1873.97	-1.4
Knurr	2178	+/-20 m	2201	127	2176.76	2199.76	2244.61	1.2
Hekkingen	2305	+/-20 m	2328	85	2301.43	2324.43	2383.62	3.6
Fuglen	2390	+/-20 m	2413	14	2391.52	2414.52	2484.1	-1.5
Stø 6	2404	+/-20 m	2427	77	2404.59	2427.59	2498.68	-0.6
Stø 5					2406.69	2429.69	2501.02	
Stø 4					2419.39	2442.39	2515.24	
Stø 3					2432.97	2455.97	2530.43	
Stø 2					2440.82	2463.82	2539.21	
Stø 1					2479.21	2502.21	2582.30	
Nordmela 2	2481	+/- 25 m	2504	77	2484.74	2507.74	2588.52	-3.7
Nordmela 1					2532.36	2555.36	2642.08	
Tubåen	2558	+/- 25 m	2581	147	2564.76	2587.76	2678.41	-6.8
Fruholmen	2705	+/- 30 m	2728	13	2674.34	2697.34	2800.00	30.7
TD	2718	+/- 30 m	2741				2908	

Table 4.3. Physical properties for formation water properties

Structure	Rw at room temp. (ohmm)	Equivalent salinity (ppm eq. NaCl)	Rw at reservoir temp. (ohmm)
Snøhvit	0.068 @ 15.6 oC	144000	0.021 - 0.023

4.1.4. Formation characteristics

The formation evaluation of different intervals is determined based on gamma ray, density, sonic, neutron, resistivity and PEF (photoelectric absorption). The CPI plots for Stø, Nordmela, Tubåen and Fruholmen formations are demonstrated in Figure 4.1 until Figure 4.4, respectively. Description of the different tracks in the CPI plots is shown as Table 4.4. In the following subsections the lithology and reservoir quality of each formation is described.

Table 4.4. CPI plot description

Track Number	Description
1	Depth (MD RT)
2	Geological Zonation
3	GR (green), calliper (black), BS (gray), Clay
4	Resistivities: Rxo (black), Rt (red)
5	PEF (black), NPHI (blue), RHOB (red)
6	DT (red), DTS (blue)
7	SW (blue)
8	Log derived porosity PHIT (navy), PHIE (blue), Residual hydrocarbon (green), Movable hydrocarbon (yellow), Water (white)
9	Volume clay, calcite, quartz, mica, coal, gas and water

4.1.4.1. The Stø formation

The Stø Formation is of Late Toarcian to Bathonian age. It consists of thick sandstones alternating with thin shales and mudstones. It has been subdivided into 6 reservoir zones, Stø1-Stø6, in which Stø 3, 4, 5 and 6 are hydrocarbon pay zone. Among different zones, the Stø5 is the lowermost, thickest and best reservoir zone. Stø1 comprises from sandstones with a moderate reservoir quality. The porosity is varying between 6% to 13% and the water saturation is changing from 40% to 100%. The Stø2 is an interval comprising fine to coarse grained sandstones with small volume of limestone patches with porosity between 12% until 18% and water saturation between 60 % to 100%. The Stø3 consists of very fine-grained sandstones, interbedded with thinner mudstones and shales. Three main shale intervals have been identified in this zone wells in the area. The reservoir quality of the Stø3 is moderate with average porosity of 10% and average water saturation of 60%. The Stø4 consists of fine to medium-grained, sandstones, of good reservoir quality. The gamma ray log suggests the often fining upward for this zone. The average porosity is around 12% and average water saturation is near 40%. The Stø5 consists of medium and fine grained sandstones with interbedded limestone according to consistency of neutron and density which are equal to 19 V/V and 2.4 g/cc, respectively and photoelectric log which is 5 (B/E). The reservoir quality is good with average porosity of 13% and average water saturation of 20%. The Stø6 is thin layer of fining

up ward sandstone and shale. The reservoir quality is good with average porosity of 12% and water saturation of 40% (Figure 4.1).

4.1.4.2. The Nordmela formation

The Nordmela Formation is of Late Hettangian to Pliensbachian age, and consists of alternating very fine to fine grained sandstones and mudstones. These sediments can be organized in both fining and coarsening upward sequences. The Nordmela Formation is divided into a lower unit with very poor reservoir characteristics and an upper, unit with reservoir qualities ranging from poor to moderate. The average water saturation is near to 80% (Figure 4.2).

4.1.4.3. The Tubåen formation

The Tubåen Formation is of Late Rhaetian to Early Hettangian in age. The formation is dominated by sandstones with subordinate shales and two minor layers of coals near the base of the formation. From this reason and due to the fact that it is important to have a consistent and uniform mapping of sand in connection with CO2 deposition, the base of the formation has been picked for the CO2 sequestration in Snøhvit Area. Gamma ray shows the Tubåen formation has clean sandstones with both a blocky appearance and slightly fining or coarsening upward log pattern. The average porosity is around 12% and the ware saturation is near to 80% (Figure 4.3).

4.1.4.4. The Fruholmen formation

The base of this formation is shale with interbedded sand stone and the middle part is mostly sandstone while the upper part is mostly shale. The mica patches is observed in the whole formation according to mineral identification tables. The reservoir quality is poor with average porosity of 5% and average water saturation of 80%. The effective porosity is very low since the formation is compact (Figure 4.4).

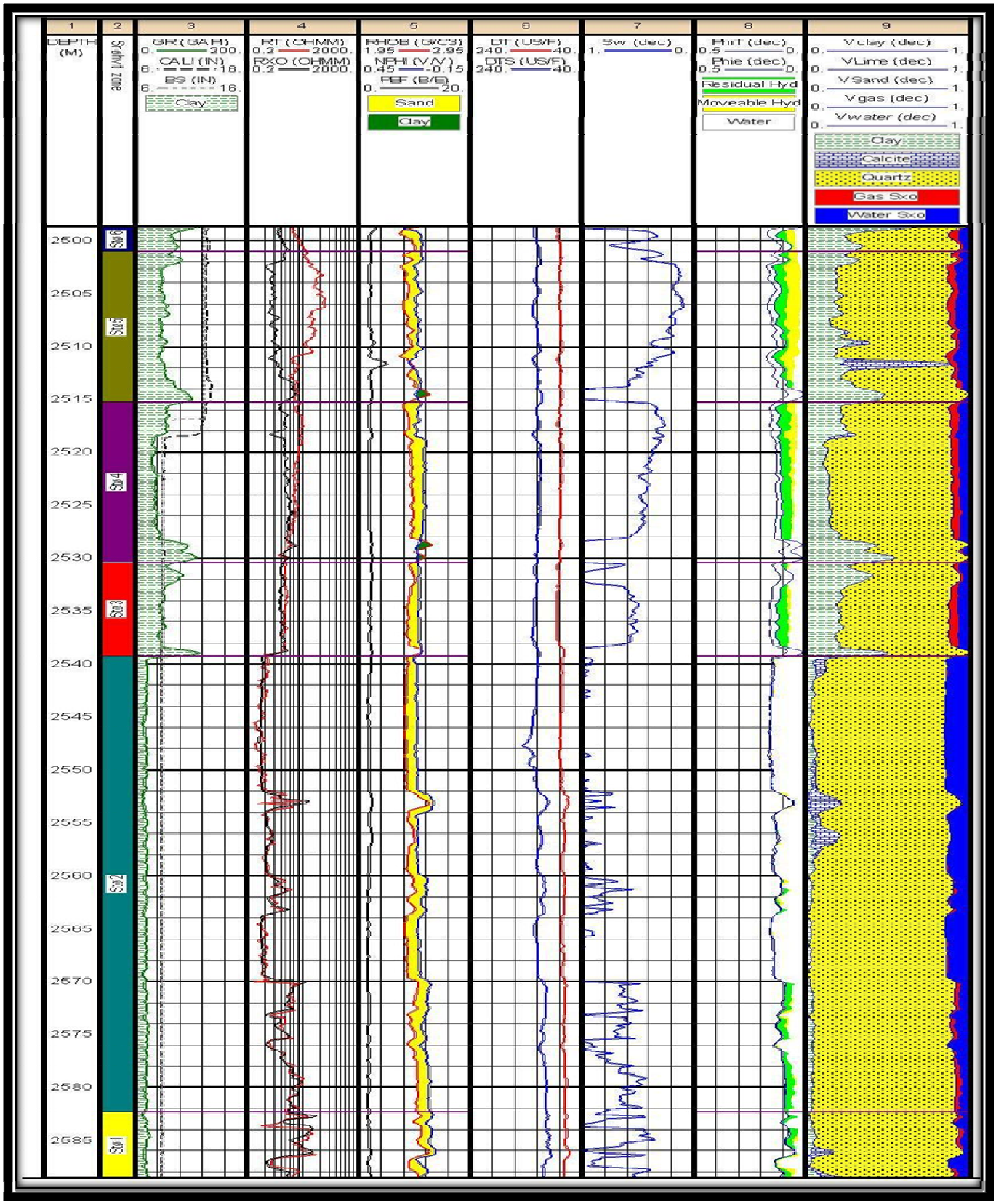

Figure 4.1. CPI plot Stø formation, 1:500 scale

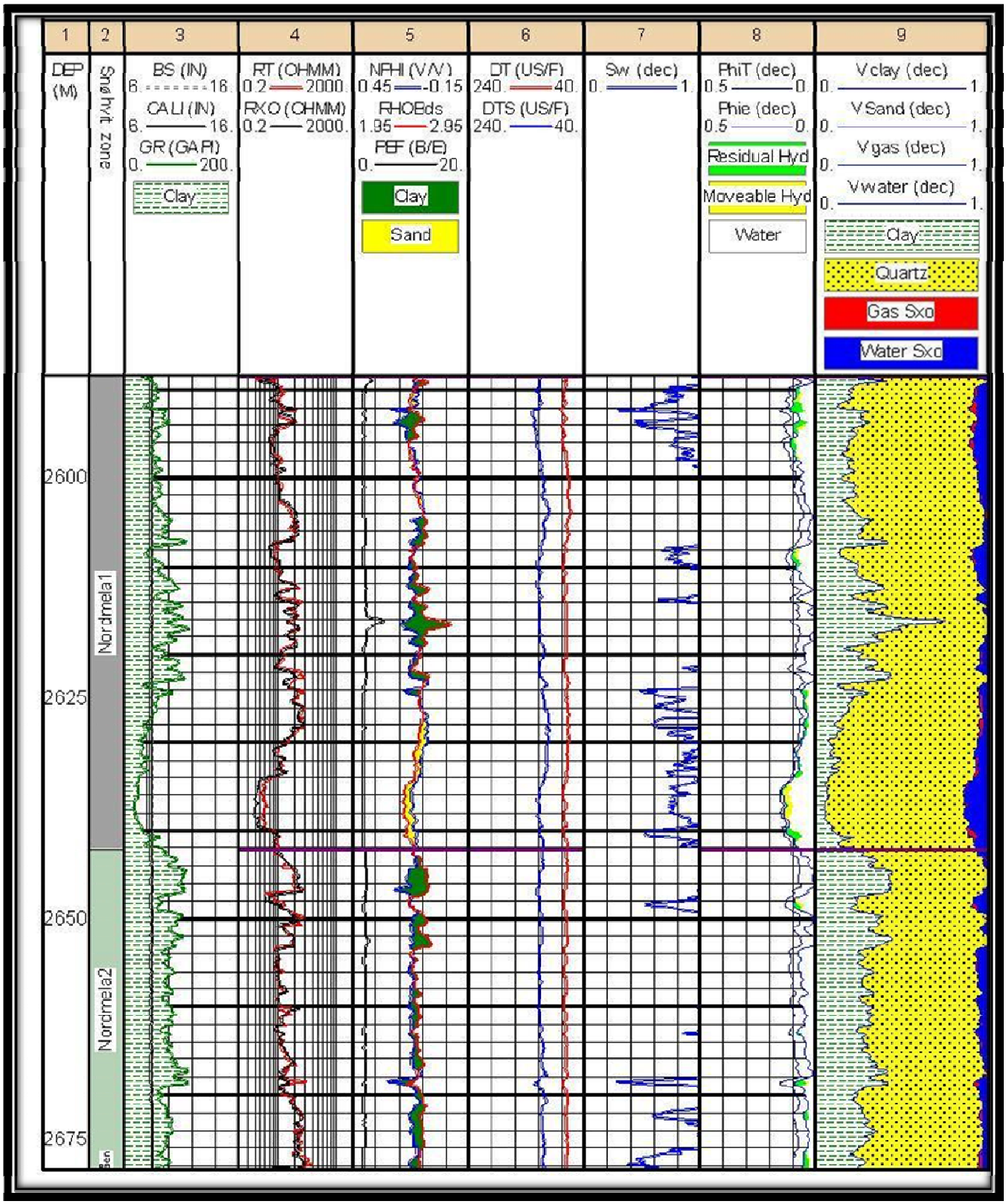

Figure 4.2. CPI plot Nordmela formation, 1:500 scale.

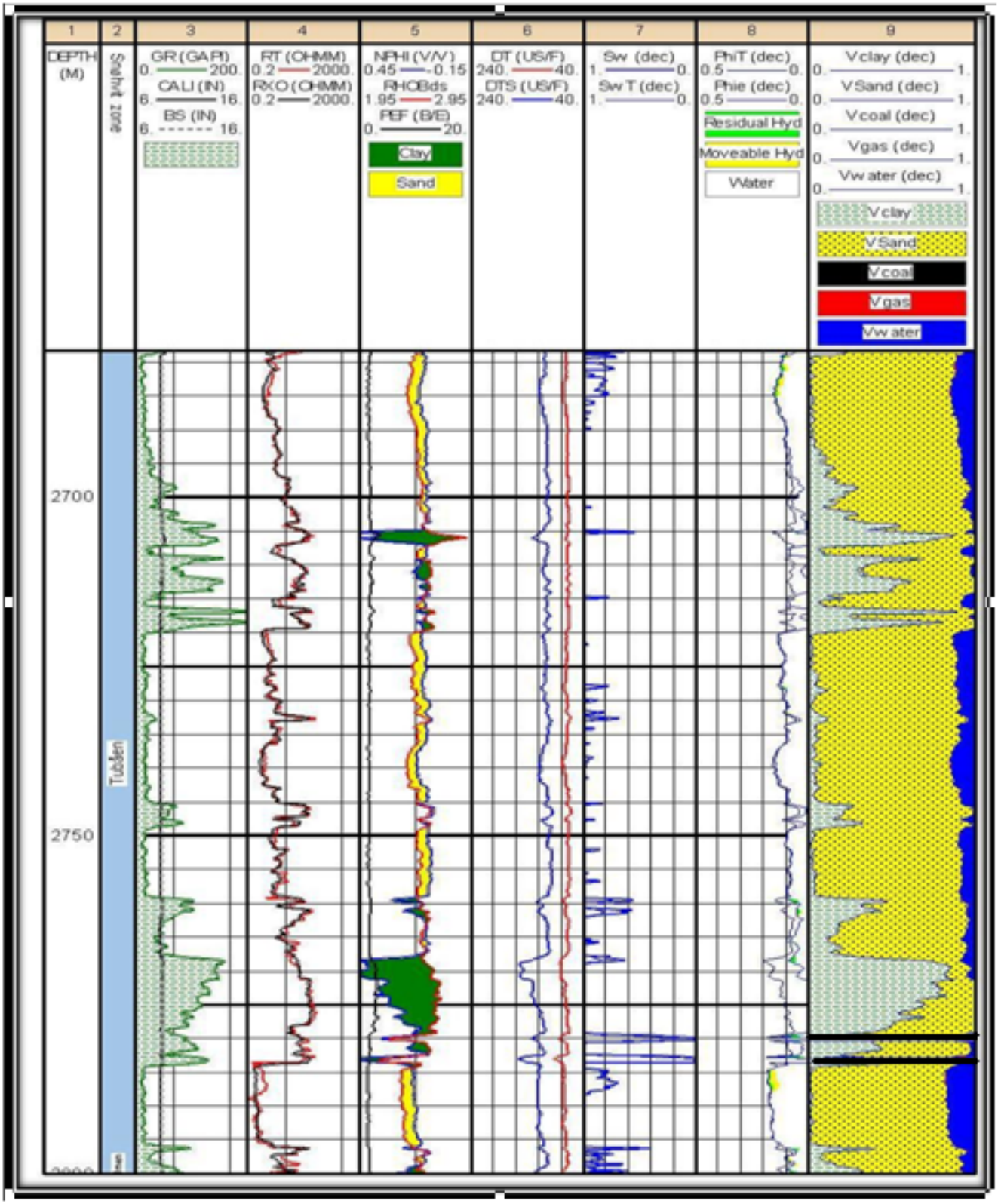

Figure 4.3. CPI plot Tubåen formation, 1:500 scale.

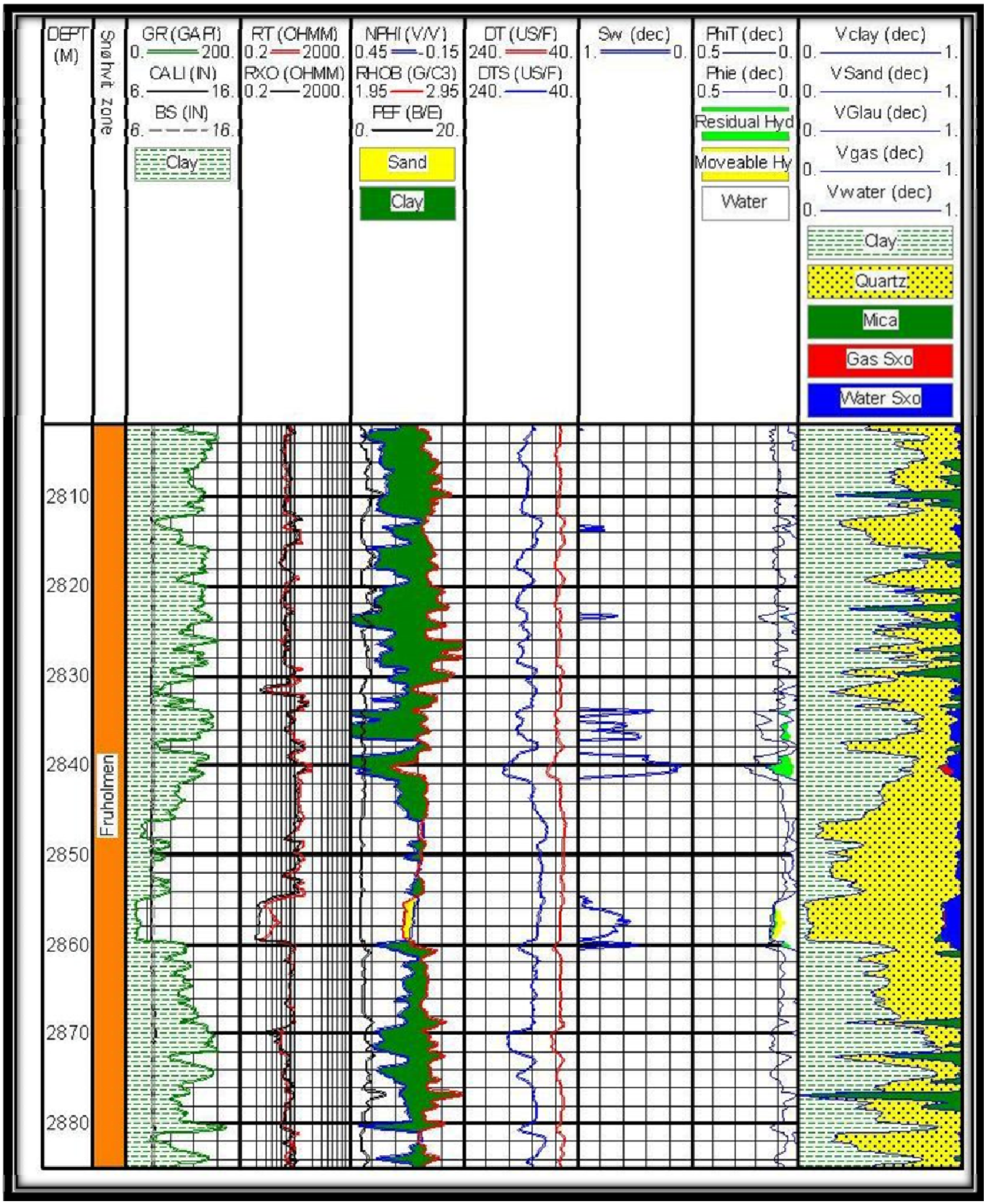

Figure 4.4. CPI plot Fruholmen formation, 1:500 scale.

4.2. Dynamic elastic rock properties

The mechanical properties of formations and dynamic elastic constants of subsurface rocks can derived from the measurement of elastic wave velocities and density of the rock. Sonic logging and waveform analysis provide the means for obtaining continuous measurements of compressional and shear velocities. These data, in conjunction with a bulk density measurement, permit the in-situ measurement and calculation of the mechanical properties of the rock. The elastic moudli relationships, in terms of elastic wave velocities (or transit times) and bulk density can be calculated from following equations.

$$\mu = \frac{\frac{1}{2}\left(\frac{\Delta t_s}{\Delta t_c}\right)^2 - 1}{\left(\frac{\Delta t_s}{\Delta t_c}\right)^2 - 1} \tag{4.6}$$

In this equation μ is the Poisson's ratio, Δt_s is shear wave travel time and Δt_c is compressional wave travel time.

$$G = \frac{\rho_b}{\Delta t_s^2} * a \tag{4.7}$$

Where G is the shear modulus (psi) and ρ_b is the bulk density (gr/cc) and a is the constant coefficient which is equal to 1.34*10 10.

$$E = 2G(1 + \mu) \tag{4.8}$$

In this equation, E is the Young modulus (psi).

$$K_B = \rho_b \left(\frac{1}{\Delta t_c^2} - \frac{4}{3\Delta t_s^2}\right) * a \tag{4.9}$$

Where, K_B is bulk modulus and is defined as the ratio of volumetric deformation per applied force.

$$C_B = \frac{1}{K_B} \tag{4.10}$$

In which, C_B is the bulk compressibility and represents the change in volume pf the formation due to the change in the applied force.

$$K_R = \rho_{gr} \left(\frac{1}{\Delta t_{mc}^2} - \frac{4}{3\Delta t_{ms}^2}\right) * a \tag{4.11}$$

K_R is the rock modulus and can be related to the rock compressibility as follows.

$$C_R = \frac{1}{K_R} \tag{4.12}$$

In order to take the account of the effect of pore pressure on the rock framework the Alpha constant is defined as follows.

$$\alpha = 1 - C_R / C_B \tag{4.13}$$

Alpha tends to zero for a dense formation where the porosity is very low.

The standard practice is to use measured values of compressional travel time (Δt_c) and shear travel time Δt_s. If shear travel time cannot be measured (i.e., in soft formations or unconsolidated framework), predictions based on Poisson's Ratio and elastic moduli are not reliable. However Δt_s data may be replaced with synthetic shear travel times calculated from lithological models, using compressional travel times and bulk density that have been corrected for hydrocarbon effect. It should be noted that even though the hydrocarbon corrections are applied for the lithological model inputs for synthetic Δt_s computations, hydrocarbon corrections are not made when the raw data are used for the elastic properties calculations. In this thesis, a numerical MATLAB code is developed based on above mentioned equations to calculate the different dynamic elastic rock moudli from sonic and density log values for Well 7121/4-F-2 H drilled in Snøhvit felid and Well 7122/7-3 from Goliat field. The MATLAB code is attached in Appendix A. The calculated Poisson's ratio, bulk, shear and Young moudli, bulk compressibility and Biot elastic constant are shown in Appendix B for Well 7121/4-F-2 H and Well 7122/7-3.

4.3. Stress analysis

By combination of dynamic elastic properties with inputs of pore pressure, overburden pressure, mud weight and volume of clay, the stresses within the formation and around the well bore can be calculated. Considering the rectangular element of the formation, the triaxial stresses can be written as follows:

$$\sigma_x = mP_o + \alpha P_p(1-m)$$

$$\sigma_y = mP_o + \alpha P_p(1-m)$$

$$\sigma_z = P_o$$

Where

P_o= Overburden pressure

P_p= Pore Pressure

$$m = \frac{\mu}{1-\mu}$$

If the segment of rock is considered around the well bore the stresses should be defined in vertical, radial and tangential directions. In a cylindrical coordinates the stress components should be calculated as follows:

$$\sigma_r = P_m$$ Radial stress

$$\sigma_\theta = 3\sigma_x - \sigma_y - P_m$$ Tangential stress

$$\sigma_z = P_o + 2\mu(\sigma_x - \sigma_y)$$ Vertical stress

To obtain the effective stress deforming the rock framework it is necessary to subtract the opposing force offered by the fluid inside the system thus effective stresses should be calculated according to the following the following equations.

$$\sigma_{reff} = P_m - \alpha P_p$$ Effective radial stress

$$\sigma_{\theta eff} = 3\sigma_x - \sigma_y - P_m - \alpha P_p$$ Effective tangential stress

$$\sigma_{zeff} = P_o + 2\mu(\sigma_x - \sigma_y) - \alpha P_p$$ Effective vertical stress

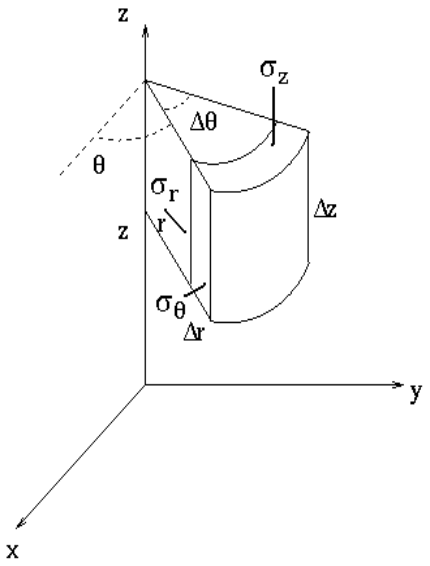

Figure 4.5. Stress components for rock segment in radial coordinate

4.4. Mohr-Coulomb failure criterion

The Mohr-Coulomb Failure Criterion was used in the sand strength analysis program and is described extensively in chapter two based on uniaxial and triaxial compressional strength of laboratory core analysis. In this section, the application of well logs is shown to use the Mohr-Coulomb failure for sand production. In order to link the petrophysical logs and failure criterion, the uniaxial compressional strength is defined as following correlation for sedimentary rocks by Deer and Miller (1966).

$$UCS = 0.008EV_{cl} + 0.0045E(1 - V_{cl})$$ Uniaxial Compressive Strength

The initial shear stress in the Mohr-Coulomb failure model is estimated form the following relation.

$$\tau_i = \frac{0.025UCS}{10^6 C_B}$$ Initial Shear strength

The critical well bore pressure is calculated based on below equation.

$$P_C = \frac{1.5\sigma_x - 0.5\sigma_y - 0.5\alpha P_p\left(\frac{1-2\mu}{1-\mu}\right) - 1.732\tau_i}{1 - 0.5\alpha\left(\frac{1-2\mu}{1-\mu}\right)}$$ Critical Wellbore pressure

This pressure shows the maximum well bore pressure in which the production of hydrocarbon can be continued without sand production. Accordingly the pressure drop equal to $\Delta P=P_o-P_c$ is the maximum draw down pressure that well can be operated without sand failure and sand production. The negative values of P_c show the well will not affected by sand production at any draw down pressure and production rate. The MATLAB code for calculation of critical well bore pressure versus depth for different formations of the studied wells is developed and attached in Appendix A. The Mohr-Coulomb circle and related failure line for each formation and depth based on the well logs also can be computed from this MATLAB code.

4.5. Case study

The application of the presented failure model and generated MATLAB code for the two wells from Snøhvit and Goliat fields is shown in this section. The critical well bore pressures versus depth are calculated and are shown in Figures 4.6 and 4.7 for the two studied wells in Snøhvit and Goliat fields, respectively. From Figure 4.6, it is possible to conclude that the critical well bore pressures are negative for all depths. One can infer from this figure that the rock failure is not probable based on the used field parameter, well log data and failure criterion. This is means at any draw down pressure and well bore production rate the sand production is not occurring. In contrast to the well 7121/4-F-2 H in Snøhvit field the critical well bore pressure for well 7122/7-3 in Goliat field is positive at any depth indicating the problem of sand production for whole interval. In this case, the value of critical well bore pressure suggests the maximum pressure of well at which the production can be performed without the risk of sand failure and sand production. The difference of the critical well bore pressure at any depth from the formation pore pressure refers the allowable draw down pressure that can be imposed for the production without sand production.

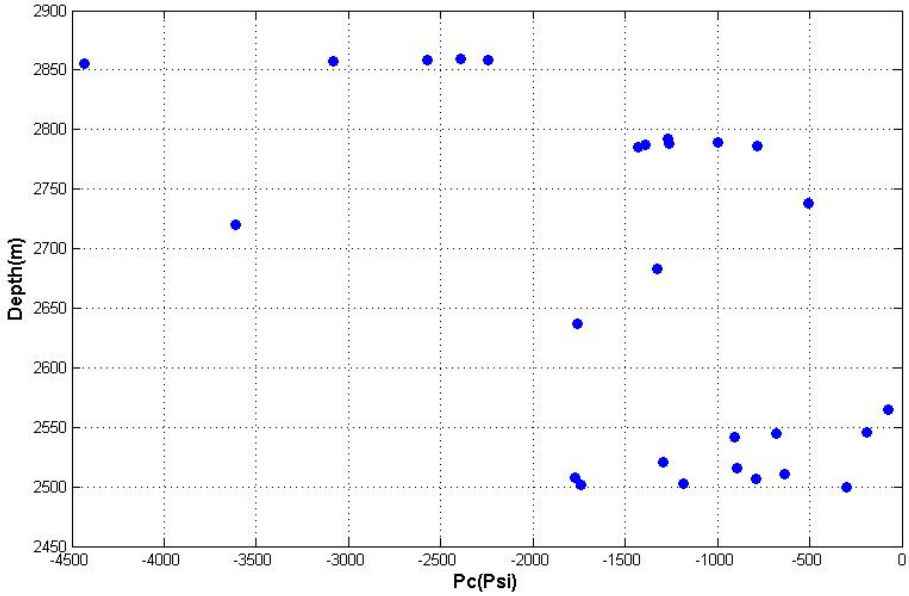

Figure 4.6. Critical well bore pressure versus depth for well 7121/4-F-2 H in Snøhvit field

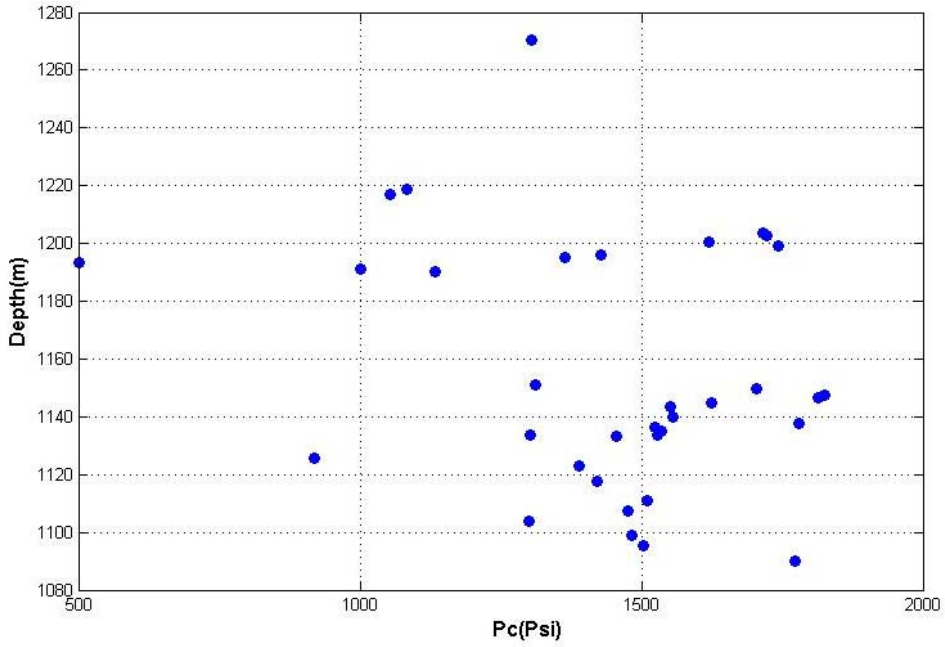

Figure 4.7. Critical well bore pressure versus depth for Well 7122/7-3 in Goliat field

The Mohr-coulomb circle and failure line for Tubåen formation and depth of 1137 m is shown in Figure 4.8. In this figure the compressional-shear stress relation for situation at which the pressure of well is set as 2190 psi is illustrated also. The critical well bore pressure at this depth is around 1784 psi; the formation pore pressure and mud pressure also are equal to 1817 psi and 2222 psi respectively. The figure shows the condition that the difference between the well bore pressure and formation pressure exceeds the maximum allowable pressure difference which should be estimated from the difference of critical well bore pressure from pore pressure. Accordingly the failure condition circle will intersect the Mohr-column circle and failure line envelope.

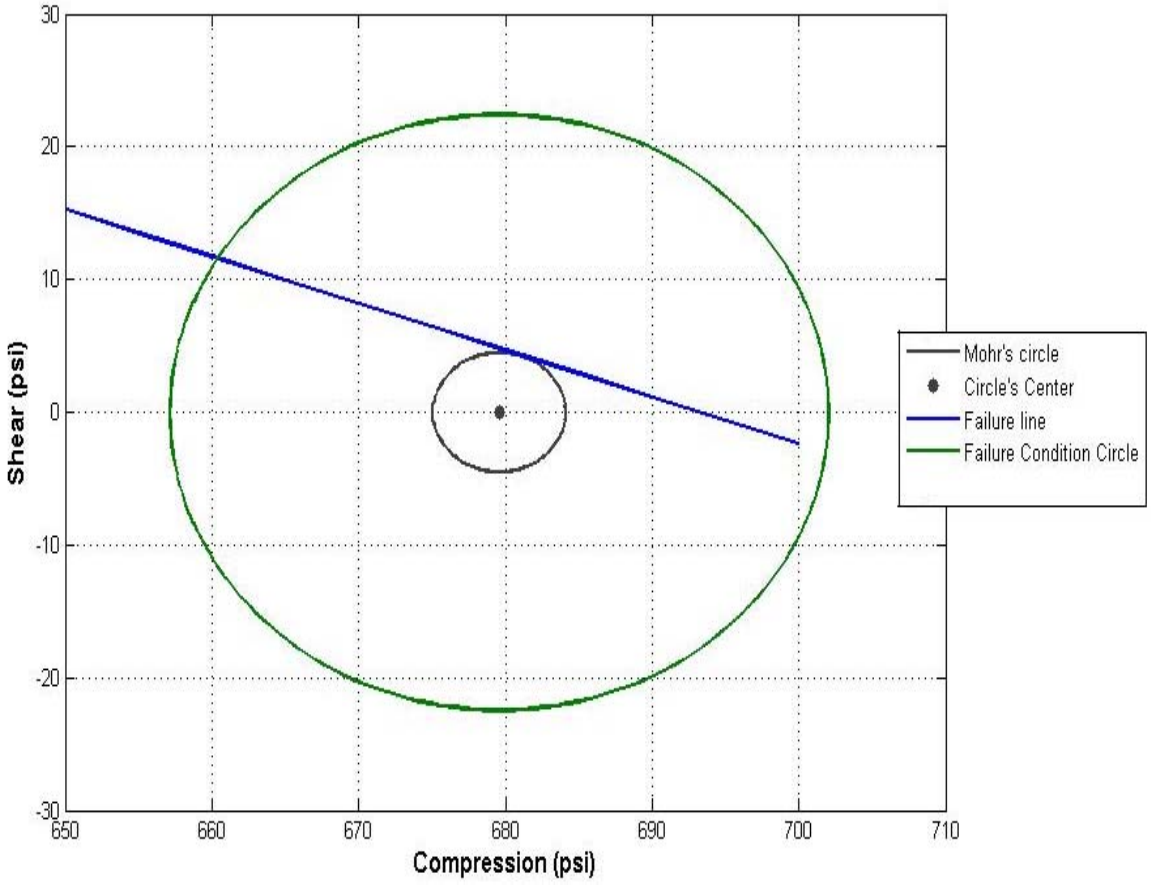

Figure 4.8.Failure condition, Mohr-Coulomb circle and failure line

depth 1137 m for well 7122/7-3 in Goliat field

The different behavior of sand production at two these wells can be linked to the packing of sand grains and cementation. In fact for the well 7121/4-F-2 H in Snøhvit field, the sandstone framework is intact due to the high depth and considerable overburden pressure. Consequently the porosity of the formations in this well is less comparing to the porosity of the corresponding formations in Well 7122/7-3 drilled in Goliat field. For well 7121/4-F-2 H in Snøhvit field, the porosity of the Tubåen formation is varying between 8% up to the 18% based on the evaluated logs in this work, while for the Well 7122/7-3, the range of porosity for the Tubåen formation is around 23% shown in Figure 4.9.

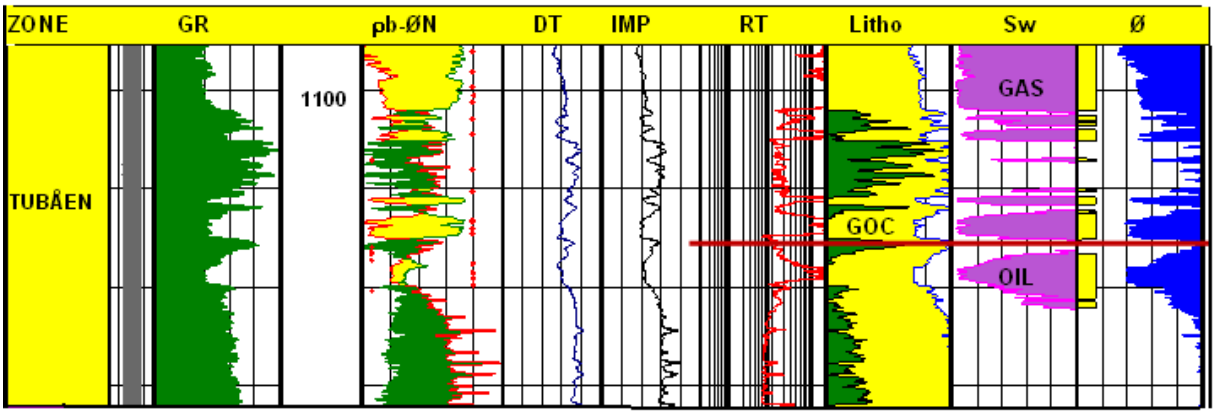

Figure 4.9. Petrophysical evaluation of Tubåen formation Well 7122/7-3

The compaction of Tubåen formation in Snøhvit field can be clearly seen from the compressional and shear travel time values measured by the sonic log. The measured compressional and shear travel times and calculated rock elastic modulus based on the petrophysical data for the two wells are shown in Figure 4.10 and 4.11 for the Tubåen formation in the well 7121/4-F-2 H and Well 7122/7-3, respectively. It is obvious that the range of rock modulus for the Tubåen formation in well 7121/4-F-2 H is higher than the rock modulus for the same formation in Well 7122/7-3. This indicates the Tubåen formation is more compact in Snøhvit field compared to the Goliat field; hence the sand production problem is not occurring in Snøhvit field in contrast to the Goliat field. The other possible reason may be linked to the presence of gas in Tubåen formation for the Well 7122/7-3 in Goliat field which has an important effect on the sonic log values and calculated dynamic rock elastic moudli. The presence of gas, oil and water in Well 7122/7-3 results to the diversity of sonic travel times and rock elastic parameters compared to the corresponding data for the well 7121/4-F-2 H where the formation fluid is only water.

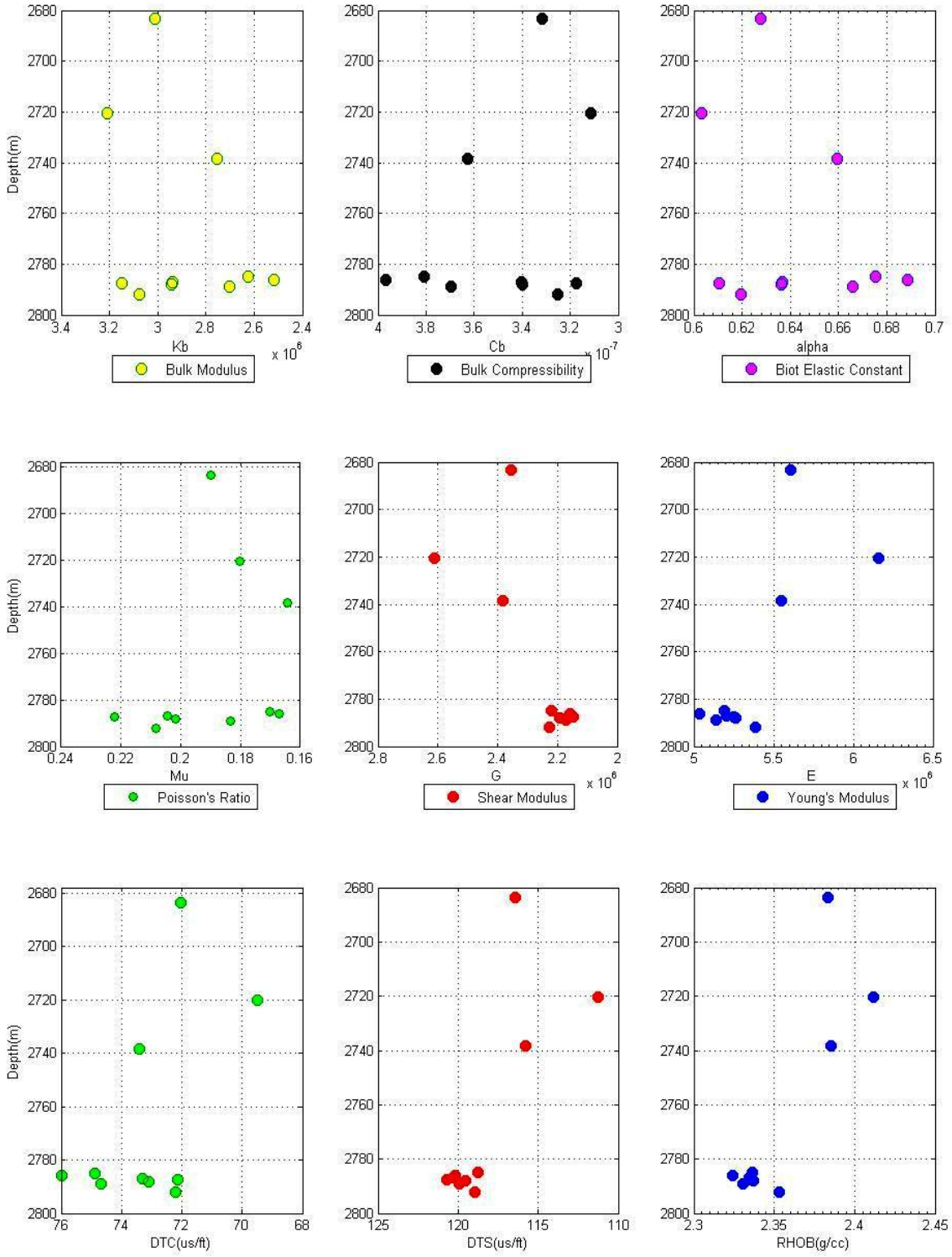

Figure 4.10. Elastic properties of Tubåen formation. (well 7121/4-F-2 H)

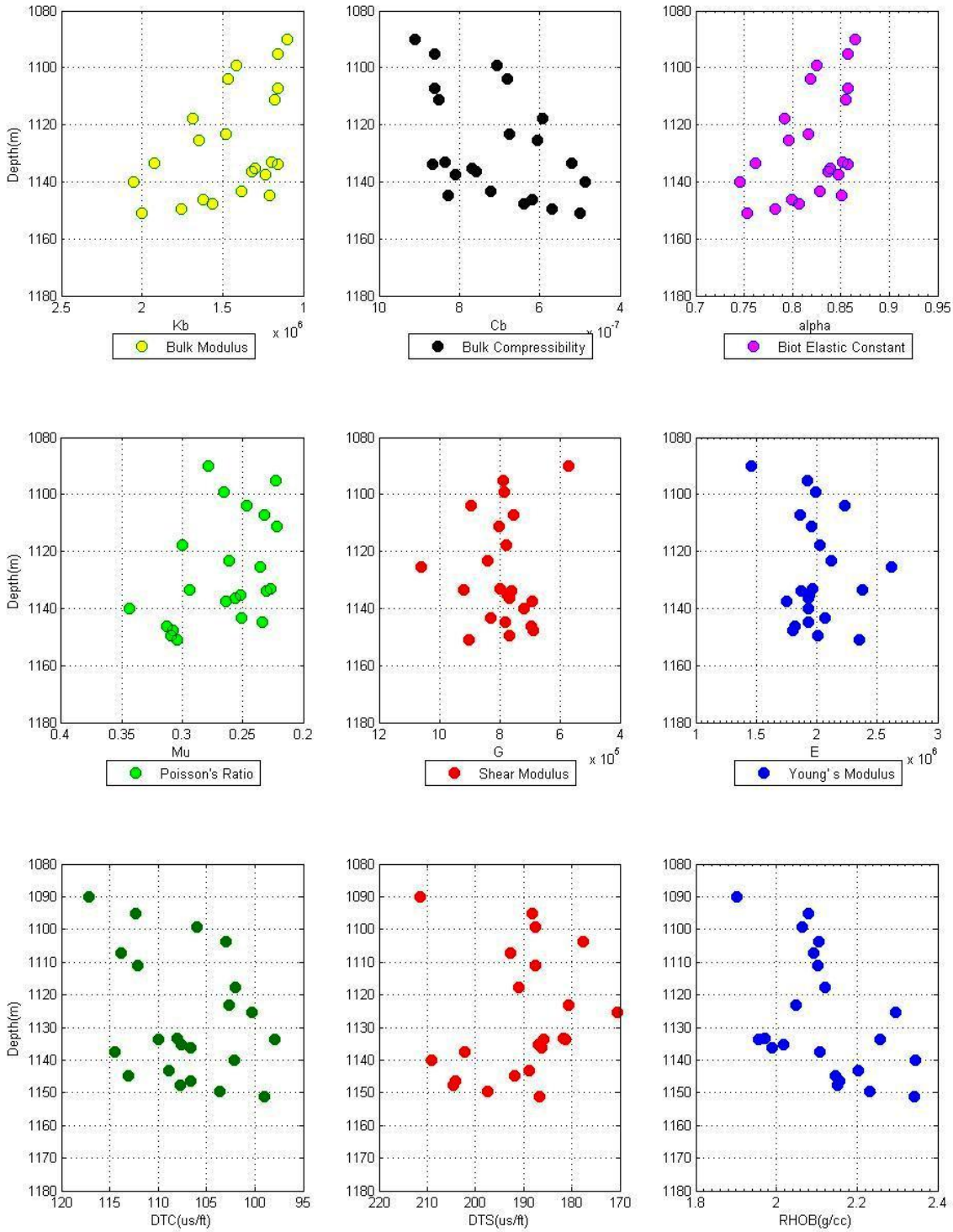

Figure 4.11. Elastic properties of Tubåen formation. (well 7122/7-3)

.

CHAPTER V
Final Remarks

In this thesis research the petrophysical evaluation of well 7121/4-F-2 H drilled in Snøhvit field is discussed using Interactive Petrophysics version 3.4 from Schlumberger. A numerical MATLAB code is also developed and explained to demonstrate the application of well logs and failure model for prediction of sand production and calculation of critical well bore pressure. Based on the petrophysical evaluation and developed MATLAB code the following consolations and recommendations are demonstrated.

5.1. Conclusions

1. The lithology, water and hydrocarbon saturations and porosity of different formations for well 7121/4-F-2 H drilled in Snøhvit are estimated based on the proposed petrophysical evaluation. These parameters are essential input data for prediction of rock failure from well logs.
2. A numerical MATLAB code has been developed using Mohr-Coulomb failure model and calculated rock elastic parameters to predict the critical well bore pressure at which sand production is less probable.
3. The difference of the critical well bore pressure at any depth from the formation pore pressure refers the allowable draw down pressure that can be imposed for the production without sand production. The negative values of P_c show the well will not affected by sand production at any draw down pressure and production rate.
4. Two sets of well log data from Snøhvit and Goliat fields are used to show the applicability of the generated code.
5. It is interesting to see that critical well bore pressure for the Tubåen formation in Snøhvit field is negative indicting the low possibility of sand production while in the Goliat field, it is positive for the same formation. The risk of sand production in Goliat field has been observed during production and confirms the validity of the method and program.
6. The different behavior of the two case studies can be linked to the packing of sand grains and cementation due to the burial depth and considerable overburden pressure. The compaction of Tubåen formation in Snøhvit field is seen from the log data. The presence of gas, oil and water in Goliat field and Well 7122/7-3 results to the diversity of sonic travel

times and the rock elastic parameters compared to the corresponding data for the well 7121/4-F-2 H and Snøhvit field where the formation fluid is only water.

5.2. Recommendations

1. In this thesis, Mohr-coulomb linear failure model is coupled to the elastic rock parameters calculated from well log data and sand failure situation is predicted. It is necessary to calibrate the log data and model to the uniaxial and triaxial rock strength laboratory results. The certainty of the discussed model is highly dependent to the linear assumption of failure envelope model hence the prediction of sand production based on non-linear failure model is recommended.
2. The sanding problem can be happened in production wells as well as injection wells. The dynamic of reservoir parameters strongly affect the failure model and prediction of sanding problem onset. Parallel computing and coupling of failure model and reservoir rock and fluid behaviors should be implemented for field development planning in enhanced oil recovery methods such as CO2 injection. In particular, the CO2 flooding can cause the swelling of residual hydrocarbons and increasing the pore pressure. In another point of view the CO2 will react to the reservoir calcite minerals and results to the fine detachment. Both phenomena will affect on sanding problem onset.

References

Addis, M.A. Hanssen, T.H. Yassir, N., Willoughby, D.R., Enever, J. (1998) "A comparison of leak-off and extended leak-off test data for stress estimation". SPE/ISRM 47235. In: Proc. Eurock '98, vol. 1, Trondheim, pp. 131–140.

Angelov P.V., (2009) "4D seismic reservoir characterization integrated with geo-mechanical modeling", Ph.D. Thesis, Delft University of Technology, Delft, The Netherlands.

Bishop, A.W. (1959) "The principle of effective stress". Teknisk Ukeblad 39, 859–863.

Boutéca, M., Guéguen, Y. (1999) "Mechanical properties of rocks: Pore pressure and scale effects". Oil & Gas Sci. Techn.-Rev. IFP 54, 703–714.

Bratli, R. K. and Risnes, R. (1979) "Stability and Failure of Sand Arches" paper SPE 8427 presented at the 54th Annual Fall Technical Conference and Exhibition of the Society of Petroleum Engineers of AIME held in Las Vegas, NV.

Brudy, M. (1998) "Determination of the state of stress by analysis of drilling-induced fractures-results from the northern North Sea". SPE/ISRM 47236. In: Proc. Eurock '98, Vol. 1, Trondheim, pp. 141–149.

Brudy, M., Zoback, M.D., Fuchs, K., Rummel, F., Baumgärtner, J. (1997) "Estimation of the complete stress tensor to 8 km depth in the KTB scientific drill holes: Implications for crustal strength". J. Geophysics. Res. 102, 18453–18475.

Breckels, I.M., van Eekelen, H.A.M. (1982) "Relationship between horizontal stress and depth in sedimentary basins". J. Pet. Tech. 34 (9), 2191–2199.

Cleary, M. P., Melvan, J. J. and Kohlhaas, C. A. (1979) "The Effect of Confining Stress and Fluid Properties on Arch Stability in Unconsolidated Sands", paper SPE 8426 presented at the 54th Annual Fall Technical Conference and Exhibition of the Society of Petroleum Engineers of AIME held in Las Vegas, NV, 23-26 September,.

Crawford, B.R., Gaillot, P.J. and Alramahi, B. (2010) "Petrophysical Methodology for Predicting Compressive Strength in Siliciclastic "sandstone-to-shale" Rocks" ARMA 10-1965th U.S.-Canada Rock Mechanics Symposium, held in Salt Lake City, UT June 27–30.

Desroches, J., Kurkjian, A.L. (1999) "Applications of wireline stress measurements". SPE Reservoir Evaluation 2(5), 451–461.

Detournay, E., Cheng, A.H.-D. (1988) "Poroelastic response of a borehole in a non-hydrostatic stress field". Int. J. Rock Mech. Min. Sci. & Geomech. Abstr. 25, 171–182.

Tiab, D., and Donaldson, E.C. (2004) "Petrophysics"2nd edition, Elsevier.

EI-Sayed, A-A. H (1991) "Maximum Allowable Production Rates from Open Hole Horizontal Wells", paper SPE 21383 presented at the SPE Middle East Oil Show held in Bahrain, 16-19 November

Farquhar, R.A., Somerville, J.M., Smart, B.G.D. (1994) "Porosity as a geomechanical indicator: An application of core and log data and rock mechanics" SPE 28853. In: Proc. European Petr. Conf., London, pp. 481–489.

Fjær, E., Ruistuen, H. (2002) "Impact of the intermediate principal stress on the strength of heterogeneous rock". J. Geophysics. Res. 107 (B2), 2032.

Fjaer, A., R.M. Holt, P. Horsrud, A. M. Raaen and R. Risnes, (2008), "Petroleum Related Rock Mechanics",2nd edition, Elsevier.

Kuhlman, R.D., Heemstra, T.R., Ray, T.G., Lin, P., Charlez, P.A. (1993) "Field tests of downhole extensometer used to obtain formation in-situ stress data". SPE 25905. In: Proc. SPE Rocky Mountain Regional/Low Permeability Res. Symp., Denver, pp. 625–634.

Kunze, K.R., Steiger, R.P. (1992) "Accurate in-situ stress measurements during drilling operations". SPE 24593. In: Proc. 67th Ann. Techn. Conf. & Exh., Washington DC, pp. 491–499.

Mase, G. T. and Mase, G. E. (1999) "Continuum Mechanics for Engineers". CRC Press.

Mulders, F. M. M. (2003)"Modeling of stress development and fault slip in and around a producing gas reservoir". Ph.D. Thesis, Delft University of Technology.

Nur, A. (1998) "Critical porosity: a key to relating physical properties to porosity in rocks". *The Leading Edge*, 17: 357-362.

Papamichos, E., Brignoli, M., Santarelli, F.J. (1997) "An experimental and theoretical study of a partially saturated collapsible rock". Mech. Cohes.-Frict. Mater. 2, 251–278.

Perkins, T. K. and Weingarten, J. S. (1988) "Stability and Failure of Spherical Cavities in Unconsolidated Sand and Weakly Consolidated Rock", paper SPE 18244 presented at the Annual Technical Conference and Exhibition of the Society of Petroleum Engineers, 2-5 October.

Plumb, R.A., Hickman, S.H. (1985) "Stress-induced borehole elongation: A comparison between the four-arm dipmeter and the borehole televiewer in the Auburn geothermal well". J. Geophysics. Res. 90B, 5513–5521.

Postler, D.P. (1997) "Pressure integrity test interpretation" SPE/IADC 37589. In: Proc. 1997 SPE/IADC Drilling ,Conf., Amsterdam, pp. 169–183.

Raaen, A.M., Brudy, M. (2001) "Pump-in/flowback tests reduce the estimate of horizontal in-situ stress significantly". SPE 71367. In: Proc. 2001 SPE Ann. Techn. Conf. & Exh., New Orleans.

Raaen, A.M., Horsrud, P., Kjørholt, H., Økland, D. (2006) "Improved routine estimation of the minimum horizontal stress component from extended leak-off tests". Int. J. Rock Mech. & Min. Sci. 43, 37–48.

Ranalli, G. (1995) "Rheology of the Earth" Chapman and Hal.

Risnes, R. and Bratli, R. K. (1981) "Sand Stress Around a Wellbore", paper SPE 9650 presented at the Middle East Oil Technical Conference of the Society of Petroleum Engineers held in Manama, Bahrain, 9-12 March.

Santana, C. and Bai, M. (2010) "Deriving Rock Mechanical Properties Using Resistivity Log Data" ARMA 10-173 Salt Lake City, UT

Snøhvit LNG project PDO support documentation geological evaluation in geology, geophysics & petrophysics, Statoil Report No. RA-SNØ-00126.

Spencer, A. J. M. (2004)"Continuum Mechanics", Dover Publications.

Tan, H.C., McGowen, J.M., Soliman, M.Y. (1990) "Field application of minifracture analysis to improve fracturing treatment design", SPE Production Eng. 5 (2), 125–132.

Thiercelin, M.J., Plumb, R.A., Desroches, J., Bixenman, P.W., Jonas, J.K., Davie, W.R. (1996) "A new wireline tool for in-situ stress measurements", SPE Formation Evaluation 11 (1), 19–25.

Tigrek, S. (2004) "Seismic Evidence of Tectonic Stresses: Implications for basin reconstruction", Ph.D. thesis, Delft University of Technology.

Tippie, D.B. and Kohlhaas, C.A (1973) "Effect of Flow Rate on Stability of Unconsolidated Producing Sands" paper SPE 4533 presented at the 48th Annual Fall Meeting of the Society of Petroleum Engineers of AIME held in Las Vegas, Nevada, 30 September - 3 October,.

Vaziri, H. H. (1995) "Analytical and Numerical Procedures for Analysis of Flow-Induced Cavitation in Porous Media", *Computers & Structures* 54, No. 2, 223.

Wærum G.O. and Skillingstad P. (2008) "Petrophysical Evaluation of Snøhvit Well 7121/4-F-2 H" Statoil Report No. 07Y97*103272

YI, X. (2003) "Numerical and analytical modeling of sanding onset prediction". Ph.D. Thesis, Texas A&M University.

Zhang, J., Wong, T.-f., Davis, D.M. (1990) "Micromechanics of pressure-induced grain crushing in porous rocks", J. Geophysics. Res. 95, 341–352.

http://www.npd.no/

Appendix A

In this appendix, MATLAB codes that were used for calculation of dynamic elastic properties, critical well bore pressure and Mohr-Coulomb failure envelope are presented.

A1. MATLAB code for calculation of dynamic elastic properties

```
Clear;
clc;
%=========================================================================
% Input Data
%=========================================================================
DATA=textread('71214-F-TUBÅEN.txt');

CTR=length(DATA(:,1));
G=zeros(CTR,1);
E=zeros(CTR,1);
Kb=zeros(CTR,1);
Cb=zeros(CTR,1);
Kr=zeros(CTR,1);
Cr=zeros(CTR,1);
alpha=zeros(CTR,1);
m=zeros(CTR,1);
Mu=zeros(CTR,1);

dTms=88;        %us/ft
dTmc=50;        %us/ft

a=1.34e10;      %gr/cm3
```

```
Rhogr=2.65;
%=========================================================================
for i=1:CTR
    %Caclulate Poisson's Ratio
    Mu(i)=(0.5*(DATA(i,3)/DATA(i,2))^2-1)/((DATA(i,3)/DATA(i,2))^2-1);

%Calculate Shear Modulus
   G(i)=DATA(i,4)*a/DATA(i,3)^2;

%Calculate Young's Modulus
    E(i)=2*G(i)*(1+Mu(i));

%Calculate Bulk Modulus
    Kb(i)=DATA(i,4)*(1/DATA(i,2)^2-4/(3*DATA(i,3)^2))*a;

%Calculate Bulk Compressibility
    Cb(i)=1/Kb(i);

% Calculate Kr
    Kr(i)=Rhogr*(1/dTmc^2-4/(3*dTms^2))*a;

%Calculate Rock Compressibility
    Cr(i)=1/Kr(i);

%Calculate Degree of Influence of Pore Pressure on the Rock Framework
    alpha(i)=1-Cr(i)/Cb(i);
```

```
%Calculate  m
   m(i)=Mu(i)/(1-Mu(i));
end
createfigure(DATA(:,2),DATA(:,1),DATA(:,3),DATA(:,4))
createfigure1(Mu,DATA(:,1),G,E)
createfigure2(Kb,DATA(:,1),Cb,alpha)
```

-MatLab code for create figure:

```
function createfigure(X1, Y1, X2, X3)
%CREATEFIGURE1(X1,Y1,X2,X3)
%  X1:  vector of x data
%  Y1:  vector of y data
%  X2:  vector of x data
%  X3:  vector of x data
%  Auto-generated by MATLAB on 23-May-2011 23:50:47
% Create figure
figure1 = figure;
% Create subplot
subplot1 = subplot(1,3,1,'Parent',figure1,'YDir','reverse','XDir','reverse');
box('on');
hold('all');

% Create plot
plot(X1,Y1,'Parent',subplot1,'Color',[0 0.498 0]);grid
% Create xlabel
xlabel('DTC(us/ft)');
```

```
% Create ylabel
ylabel('Depth(m)');
% Create subplot
subplot2 = subplot(1,3,2,'Parent',figure1,'YDir','reverse','XDir','reverse');
box('on');
hold('all');
% Create plot
plot(X2,Y1,'Parent',subplot2,'Color',[1 0 0]);grid
% Create xlabel
xlabel('DTS(us/ft)');
% Create subplot
subplot3 = subplot(1,3,3,'Parent',figure1,'YDir','reverse',...
    'XMinorTick','on');
box('on');
hold('all');
% Create plot
plot(X3,Y1,'Parent',subplot3);grid
% Create xlabel
xlabel('RHOB(g/cc)');
```

-MatLab code for create figure1:

```
function createfigure1(X1, Y1, X2, X3)
%CREATEFIGURE1(X1,Y1,X2,X3)
%  X1:  vector of x data
%  Y1:  vector of y data
%  X2:  vector of x data
```

```
%  X3:  vector of x data
%  Auto-generated by MATLAB on 23-May-2011 23:50:47
% Create figure
figure1 = figure;
% Create subplot
subplot1 = subplot(1,3,1,'Parent',figure1,'YDir','reverse','XDir','reverse');
box('on');
hold('all');
% Create plot
plot(X1,Y1,'Parent',subplot1,'Color',[0 0.498 0]);grid
% Create xlabel
xlabel('Mu');
% Create ylabel
ylabel('Depth(m)');
% Create subplot
subplot2 = subplot(1,3,2,'Parent',figure1,'YDir','reverse','XDir','reverse');
box('on');
hold('all');
% Create plot
plot(X2,Y1,'Parent',subplot2,'Color',[1 0 0]);grid
% Create xlabel
xlabel('G');
% Create subplot
subplot3 = subplot(1,3,3,'Parent',figure1,'YDir','reverse',...
    'XMinorTick','on');
box('on');
hold('all');
```

```
% Create plot
plot(X3,Y1,'Parent',subplot3);grid
% Create xlabel
xlabel('E');
```

-MatLab code for create figure2:

```
function createfigure2(X1, Y1, X2, X3)
%CREATEFIGURE2(X1,Y1,X2,X3)
%  X1:  vector of x data
%  Y1:  vector of y data
%  X2:  vector of x data
%  X3:  vector of x data
%  Auto-generated by MATLAB on 23-May-2011 23:50:47
% Create figure
figure2 = figure;
% Create subplot
subplot1 = subplot(1,3,1,'Parent',figure2,'YDir','reverse','XDir','reverse');
box('on');
hold('all');
% Create plot
plot(X1,Y1,'Parent',subplot1,'Color',[0 0.498 0]);grid
% Create xlabel
xlabel('Kb');
% Create ylabel
ylabel('Depth(m)');
% Create subplot
```

```
subplot2 = subplot(1,3,2,'Parent',figure2,'YDir','reverse','XDir','reverse');
box('on');
hold('all');
% Create plot
plot(X2,Y1,'Parent',subplot2,'Color',[1 0 0]);grid
% Create xlabel
xlabel('Cb');
% Create subplot
subplot3 = subplot(1,3,3,'Parent',figure2,'YDir','reverse',...
    'XMinorTick','on');
box('on');
hold('all');
% Create plot
plot(X3,Y1,'Parent',subplot3);grid
% Create xlabel
xlabel('alpha');
```

A.2. MATLAB code for calculation of critical well bore pressure

```
Clear;
clc;
%=========================================================================
% Input Data
%=========================================================================
DATA=textread('PC.F.txt');

TVD=DATA(:,1);
MD=DATA(:,2);
```

```
RHOB=DATA(:,3);

DTC=DATA(:,4);

DTS=DATA(:,5);

Po=DATA(:,6);

Pp=DATA(:,7);

Pm=DATA(:,8);

Vcl=DATA(:,9);


CTR=length(DATA(:,1));


G=zeros(CTR,1);

E=zeros(CTR,1);

Kb=zeros(CTR,1);

Cb=zeros(CTR,1);

Kr=zeros(CTR,1);

Cr=zeros(CTR,1);

alpha=zeros(CTR,1);

m=zeros(CTR,1);

Mu=zeros(CTR,1);

Sx=zeros(CTR,1);

Sy=zeros(CTR,1);

Sr=zeros(CTR,1);

St=zeros(CTR,1);

Sreff=zeros(CTR,1);

Steff=zeros(CTR,1);

UCS=zeros(CTR,1);

Tui=zeros(CTR,1);
```

```
Num=zeros(CTR,1);
Denum=zeros(CTR,1);
Pc=zeros(CTR,1);

dTms=88;        %us/ft
dTmc=50;        %us/ft
a=1.34e10;      %gr/cm3
Rhogr=2.65;
%==========================================================================
for i=1:CTR
    %Caclulate Poisson's Ratio
    Mu(i)=(0.5*(DTS(i)/DTC(i))^2-1)/((DTS(i)/DTC(i))^2-1);

%Calculate Shear Modulus
   G(i)=RHOB(i)*a/DTS(i)^2;

%Calculate Young's Modulus
    E(i)=2*G(i)*(1+Mu(i));

%Calculate Bulk Modulus
    Kb(i)=RHOB(i)*(1/DTC(i)^2-4/(3*DTS(i)^2))*a;

%Calculate Bulk Compressibility
    Cb(i)=1/Kb(i);
% Calculate Kr
    Kr=Rhogr*(1/dTmc^2-4/(3*dTms^2))*a;
%Calculate Rock Compressibility
```

```
    Cr=1/Kr;
%Calculate Degree of Influence of Pore Pressure on the Rock Framework
    alpha(i)=1-Cr/Cb(i);
%Calculate Stresses(Sigx-y-z)
    m(i)=Mu(i)/(1-Mu(i));


    Sx(i)=m(i)*Po(i)+alpha(i)*Pp(i)*(1-m(i));
    Sy(i)=Sx(i);


    Sr(i)=Pm(i);
    St(i)=3*Sx(i)-Sy(i)-Sr(i);


    Sreff(i)=Sr(i)-alpha(i)*Pp(i);
    Steff(i)=St(i)-alpha(i)*Pp(i);
  % Calculate of Uniaxial Compressive Strength(UCS), Intial Shear Strength(Tui), Critical Wellbore Pressure (Pc)
    UCS(i)=0.008*E(i)*Vcl(i)+0.0045*E(i)*(1-Vcl(i));
    Tui(i)=0.025*UCS(i)/(1E6*Cb(i));
    Num(i)=1.5*Sx(i)-0.5*Sy(i)-0.5*alpha(i)*Pp(i)*(1-2*Mu(i))/(1-Mu(i))-1.732*Tui(i);
    Denum(i)=1-0.5*alpha(i)*(1-2*Mu(i))/(1-Mu(i));
    Pc(i)=Num(i)/Denum(i);


end
createfigure(DTC,MD,DTS,RHOB)
createfigure1(Mu,MD,G,E)
createfigure2(Kb,MD,Cb,alpha)
figure;scatter(Pc,MD);
xlabel('Pc(Psi)');
```

```
ylabel('Depth(m)');
```

A.3. MATLAB code for plotting Mohr's circle, failure line and elastic parameters for specified depth

```
Clear;

clc;

%=========================================================================

% Input Data

%=========================================================================

dTs=202;        %us/ft

dTc=114;         %us/ft

dTms=88;         %us/ft

dTmc=50;         %us/ft

a=1.34e10;       % gr/cm3

Rhob=2.1;       % gr/cm3

Rhogr=2.65;     % gr/cm3

Vcl=0;          % V/V

Po=3410;        %psi

Pp=1817;        %psi

Pm=1900;        %psi

%=========================================================================

%Caclulate Poisson's Ratio

Mu=(0.5*(dTs/dTc)^2-1)/((dTs/dTc)^2-1);


%Calculate Shear Modulus

G=Rhob*a/dTs^2;

%Calculate Young's Modulus

E=2*G*(1+Mu);
```

```
%Calculate Bulk Modulus

Kb=Rhob*(1/dTc^2-4/(3*dTs^2))*a;


%Calculate Bulk Compressibility

Cb=1/Kb;


% Calculate Kr

Kr=Rhogr*(1/dTmc^2-4/(3*dTms^2))*a;


%Calculate Rock Compressibility

Cr=1/Kr;


%Calculate Degree of Influence of Pore Pressure on the Rock Framework

alpha=1-(Cr/Cb);


%Calculate Sigx-y-z

m=Mu/(1-Mu);


Sigx=m*Po+alpha*Pp*(1-m);

Sigy=m*Po+alpha*Pp*(1-m);

Sigz=Po;


%Calculate  Radial, Tangential, and Vertical stress

Sigr=Pm;

SigT=3*Sigx-Sigy-Pm;

Sigzr=Po+2*Mu*(Sigx-Sigy);
```

```
%Calculate  Effective Radial, Tangential, and Vertical stress
Sreff=Sigr-alpha*Pp;
STeff=SigT-alpha*Pp;
Szeff=Sigzr-alpha*Pp;

%Calculate UCS
UCS=0.008*E*Vcl+0.0045*E*(1-Vcl);
Tui=0.025*UCS/(1E6*Cb);
% Calculate SigP
Max_shear=0.5*(STeff-Sreff);
mean_normal=0.5*(STeff+Sreff);
err=1;
%First guess
phi=pi/10;
while err>1e-8
   F=Tui*cos(phi)+(mean_normal)*sin(phi)-abs(Max_shear);
   dF=-Tui*sin(phi)+mean_normal*cos(phi);
   phin=phi-F/dF;
   err=abs(1-phin/phi);
   phi=phin;
end
deg=180*phi/pi;
beta=deg/2+45;
% Calculate Tui,Pc,

Num=1.5*Sigx-0.5*Sigy-0.5*alpha*Pp*(1-2*Mu)/(1-Mu)-1.732*Tui;
```

```
Denum=1-0.5*alpha*(1-2*Mu)/(1-Mu);

Pc=Num/Denum;


% Mohr's Circle

theta = (0:180) *pi/180;

Ns = mean_normal +abs(Max_shear)*cos(2*theta);

Ss = abs(Max_shear)*sin(2*theta);


% Plot Mohr's Circle

plot(Ns,Ss,'k-','Color',[.25 .25 .25],'LineWidth',1.5 );

hold on;

plot(mean_normal,0,'k.','MarkerSize',18,'Color',[.25 .25 .25])

plot(0,0,'k.','MarkerSize',16,'Color',[.25 .25 .25])

grid on;


%Plot the Failure line

hold on;

x = 0:100:1000;

y = Tui + tan(phi)*x;

plot(x,y)

hold off;
```

Appendix B. Dynamic Elastic Properties of Formations for both Wells

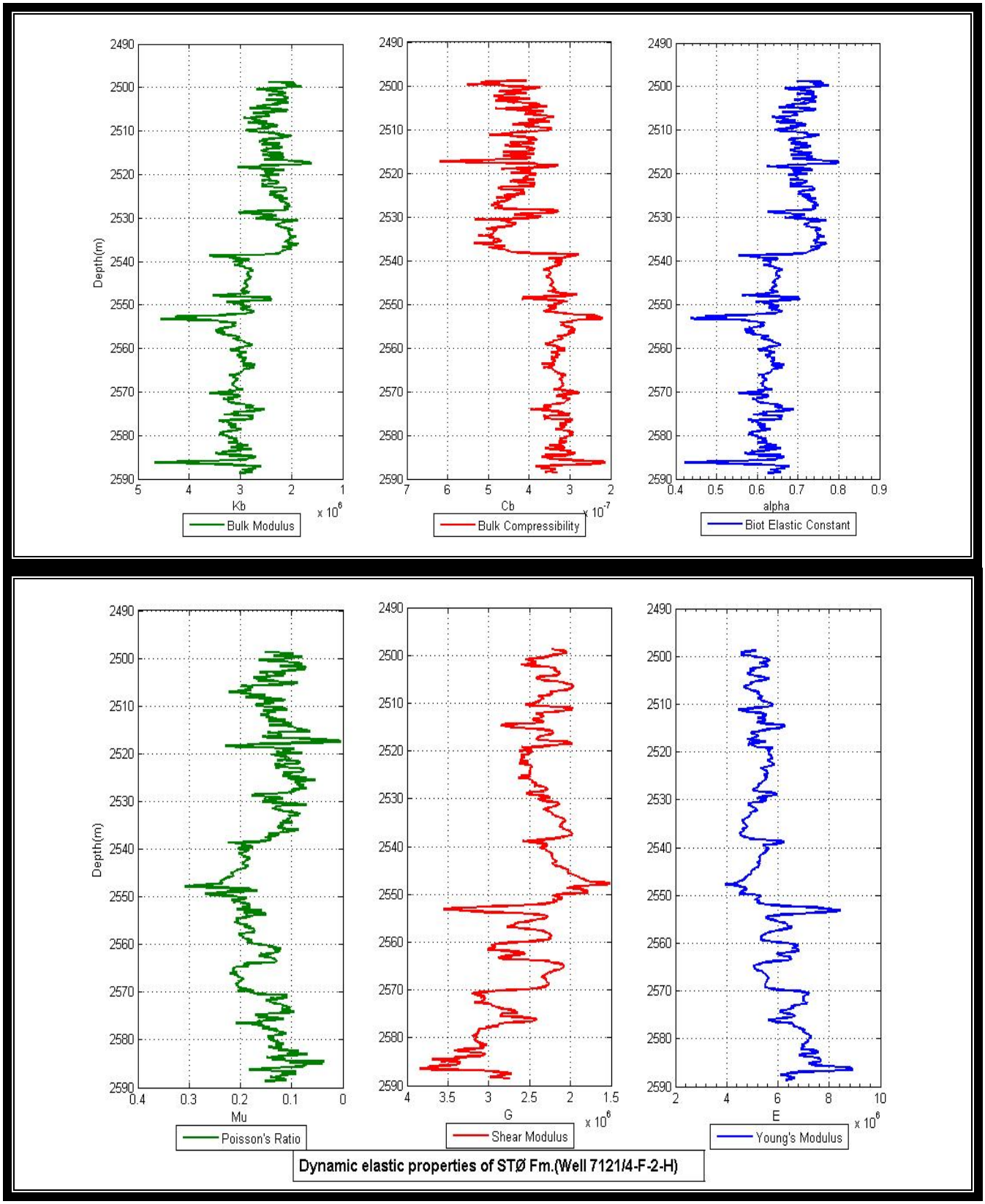

Figure B.1. Dynamic elastic properties of STØ Fm.

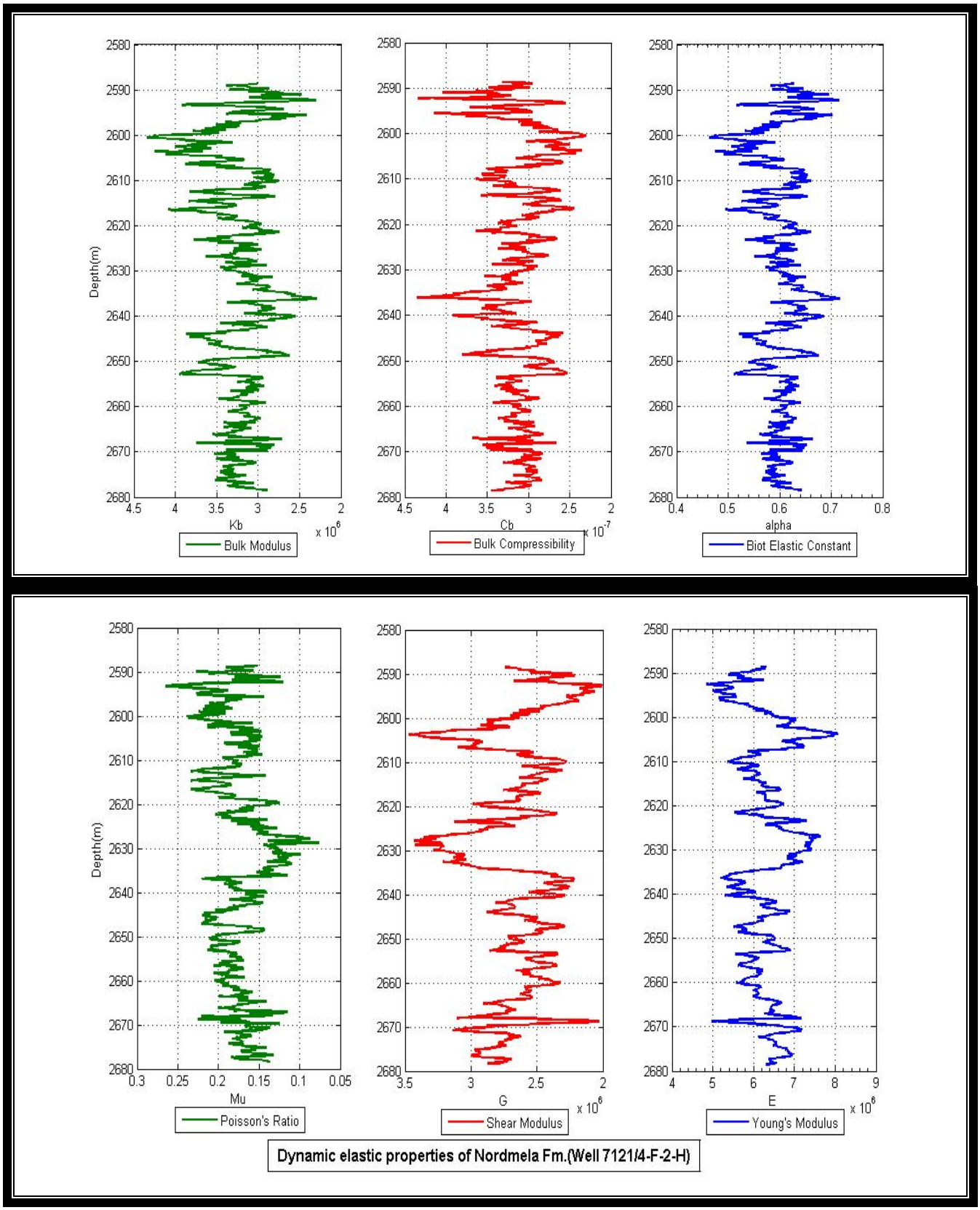

Figure B.2. Dynamic elastic properties of Nordmela Fm.

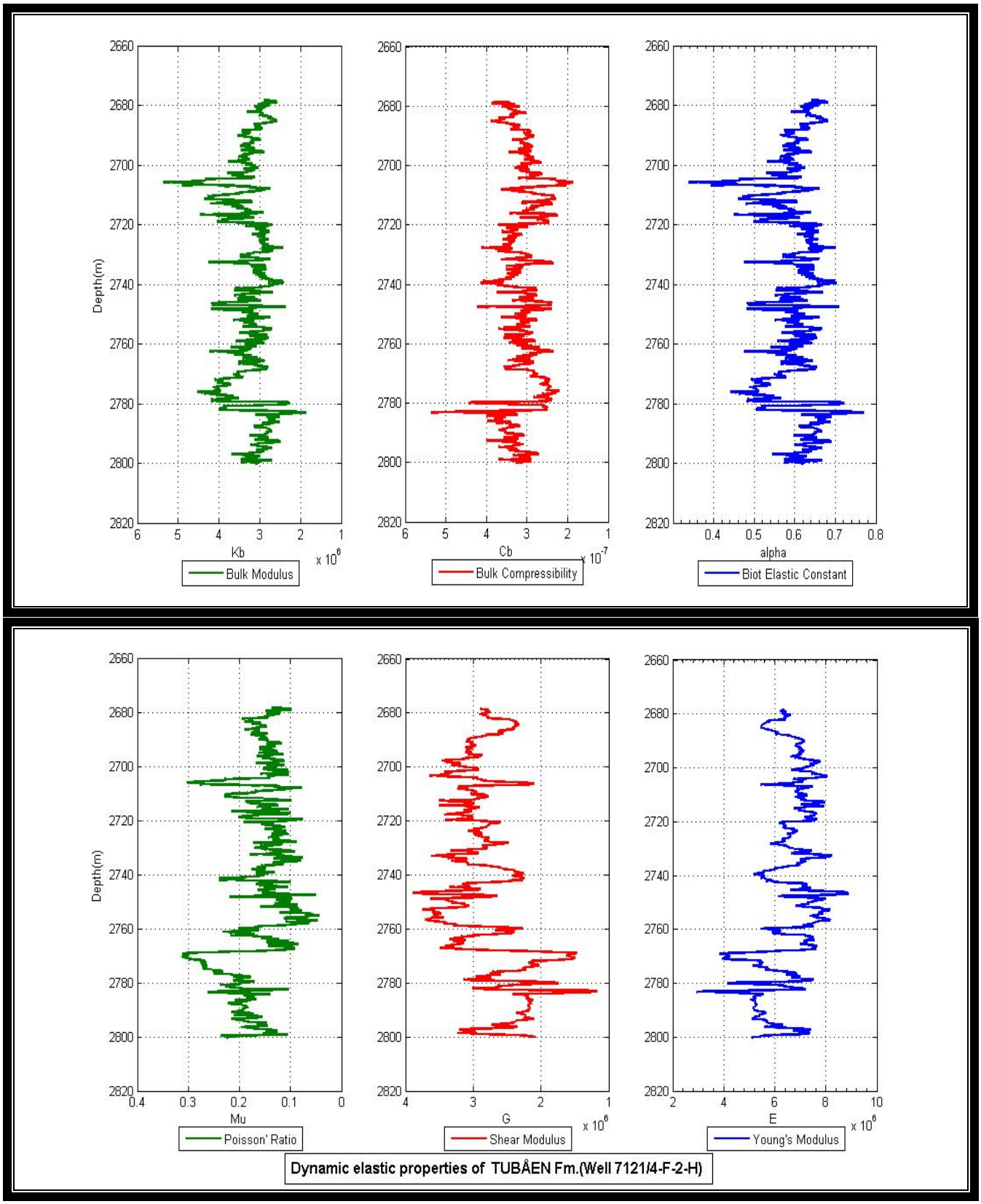

Figure B.3. Dynamic elastic properties of Tubåen Fm.

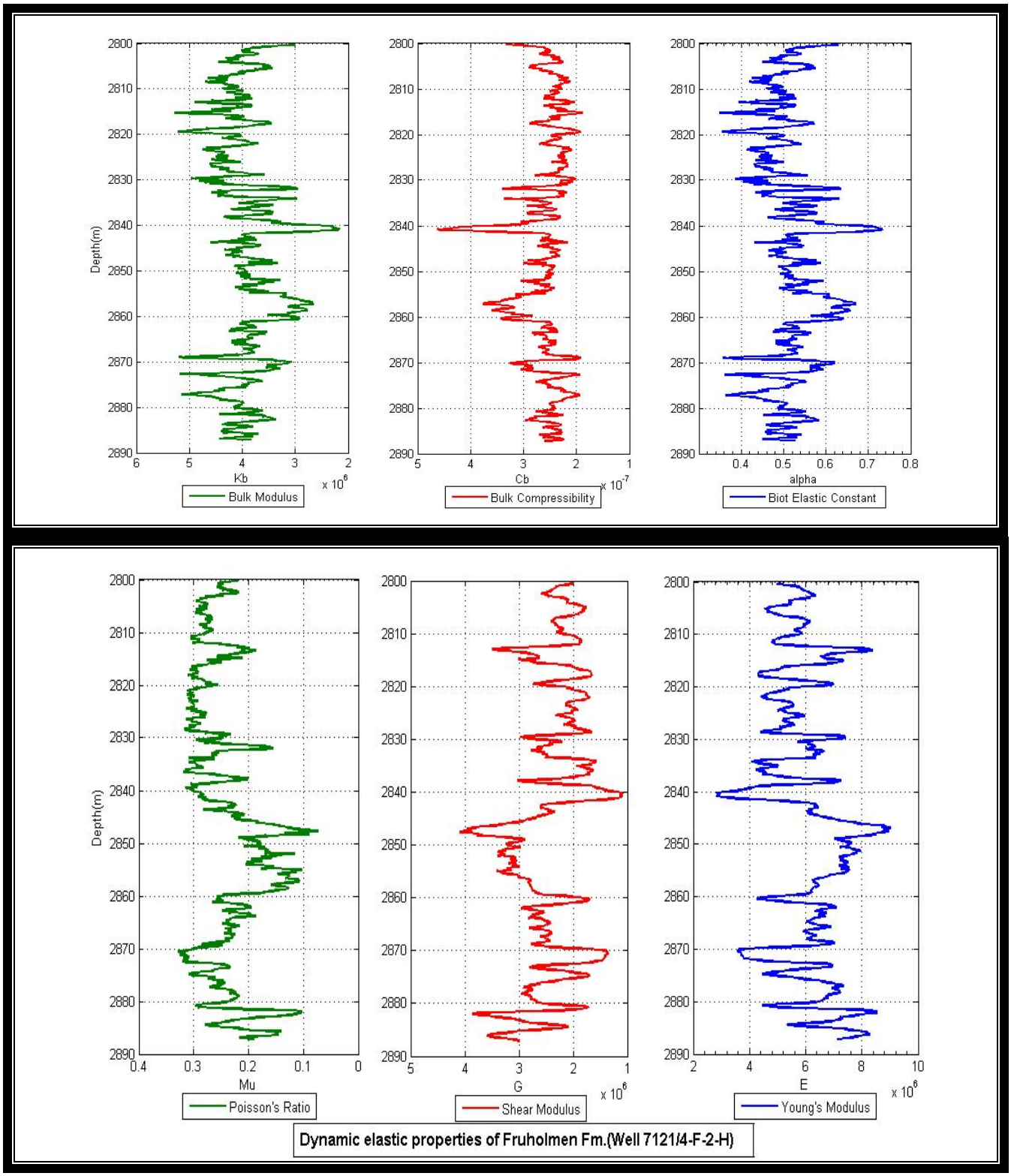

Figure B.4. Dynamic elastic properties of Fruholmen Fm.

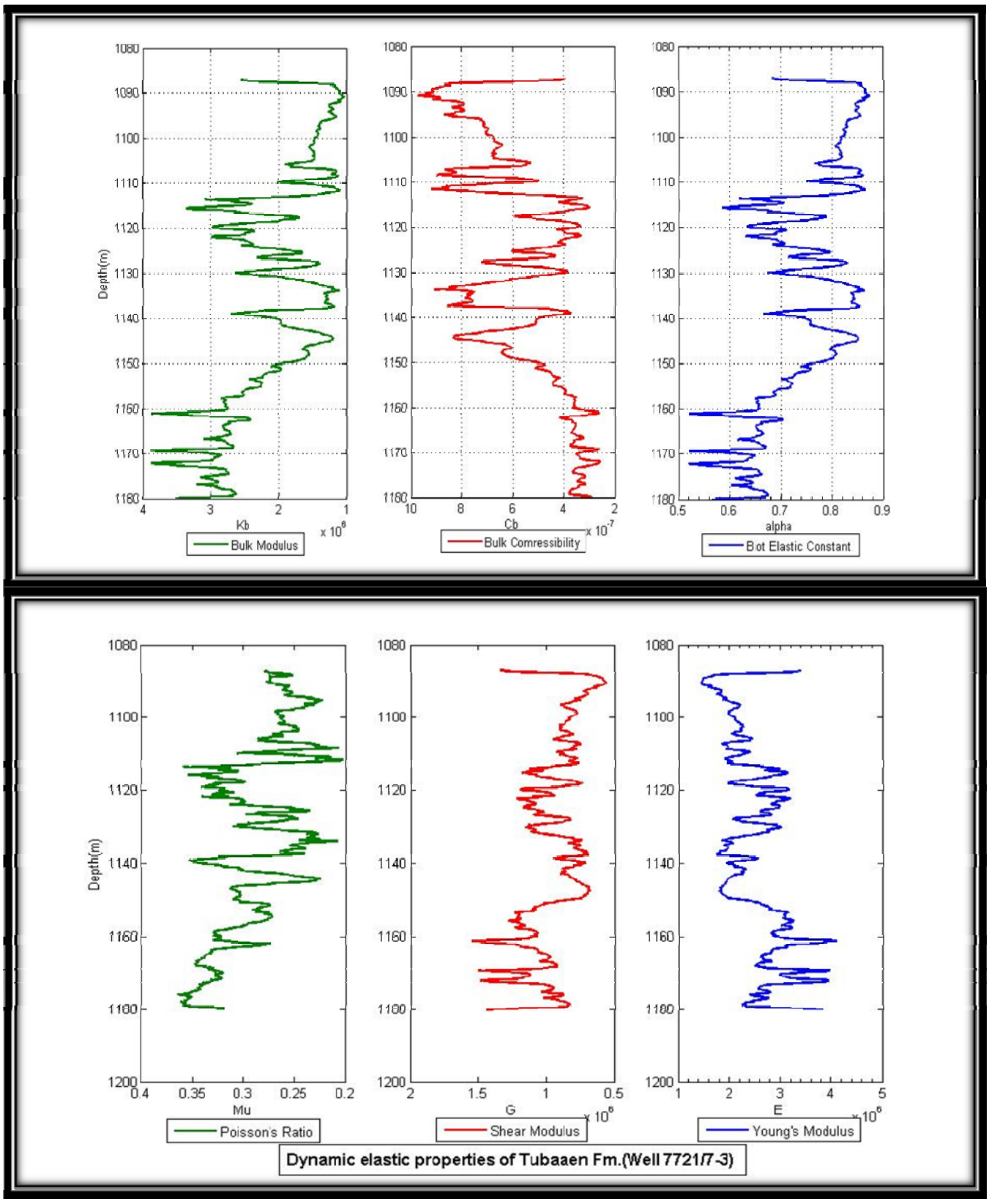

Figure B.5. Dynamic elastic properties of Tubåen Fm.

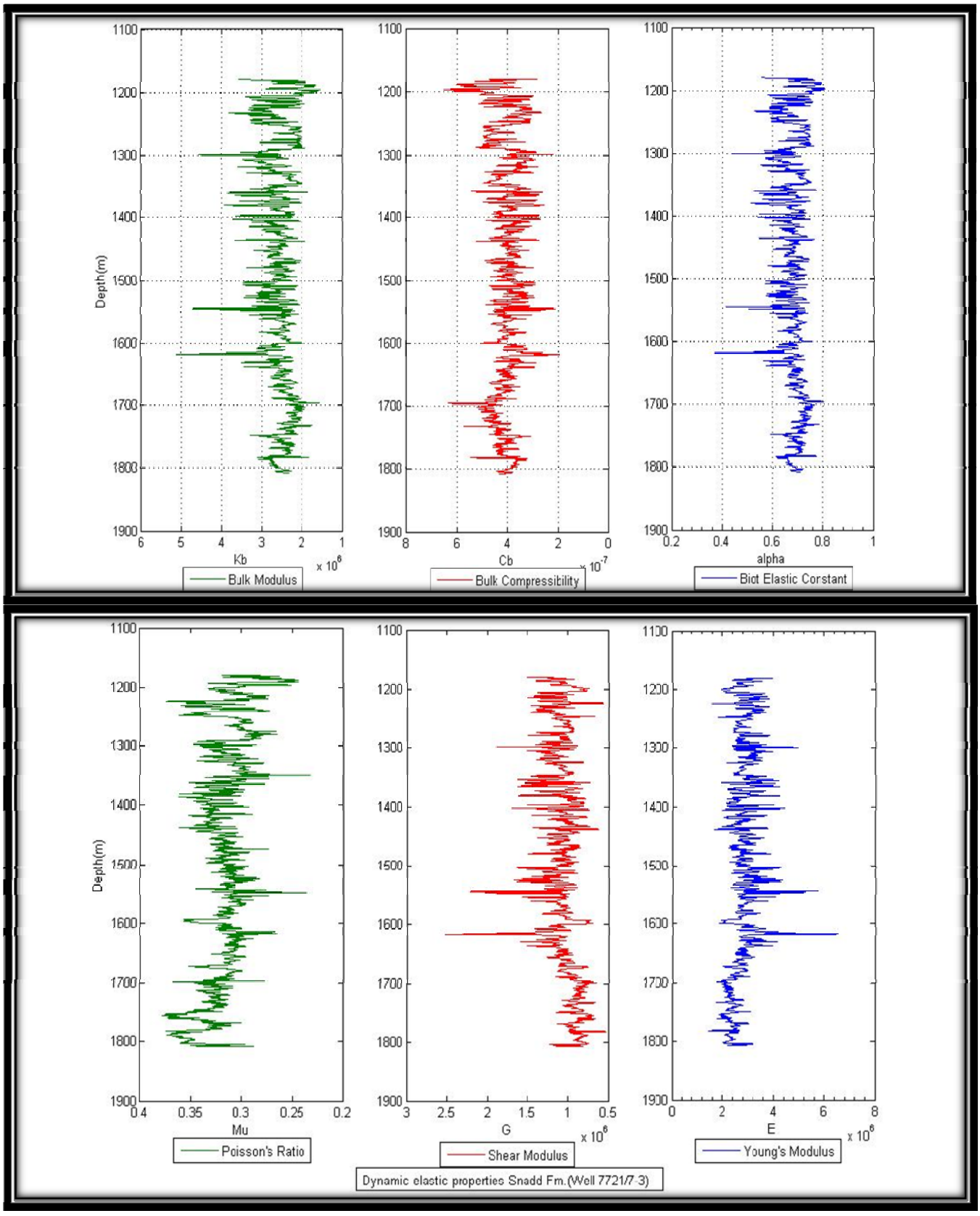

Figure B.6. Dynamic elastic properties of Snadd Fm.

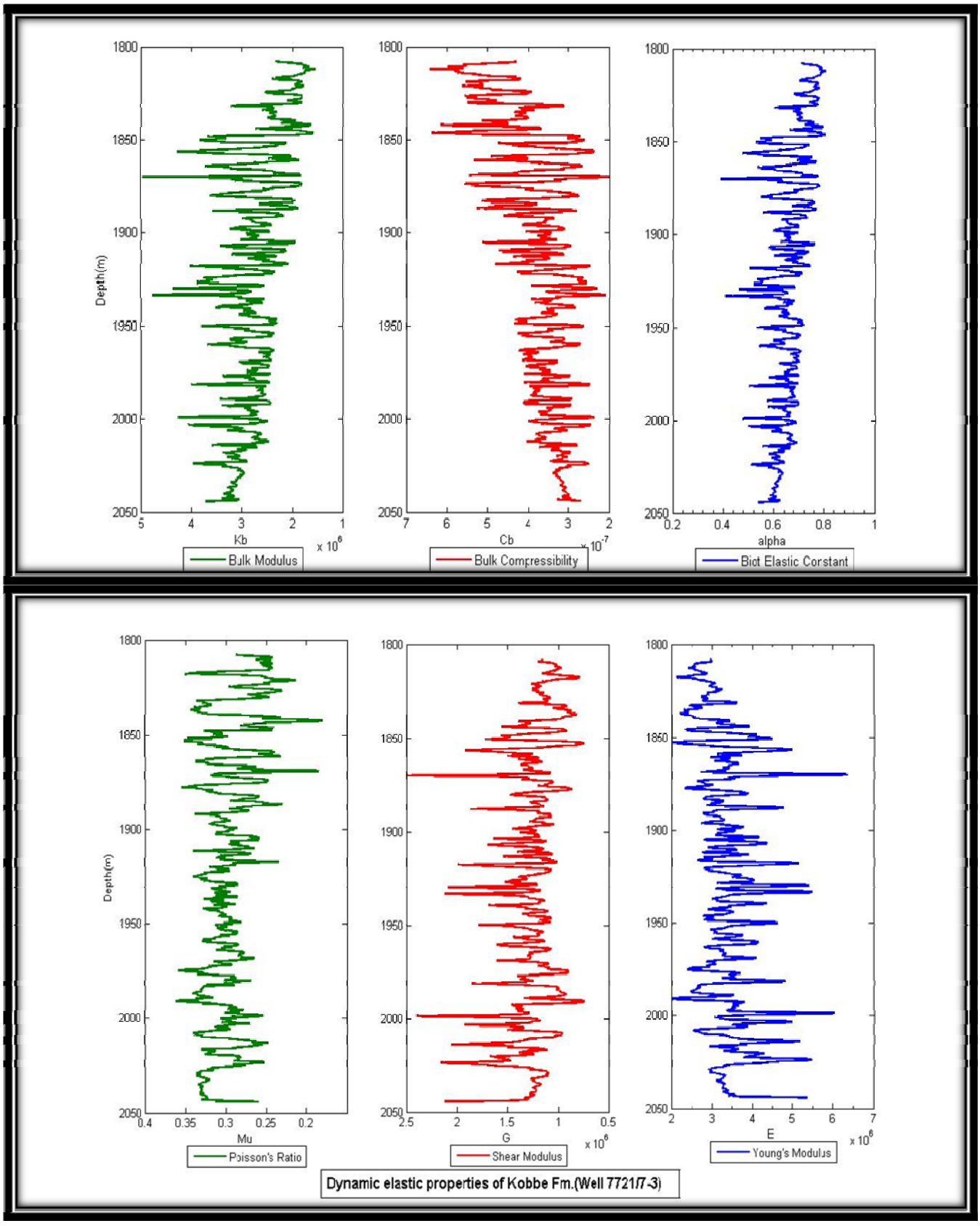

Figure B.7. Dynamic elastic properties of Kobbe Fm.

Appendix C

In this Appendix the data were used to calculate critical well bore pressure are presented in Tables C.1 and C2.

Table C.1. Used data for calculation of Pc in MATLAB for well 7122/7-3

TVD	MD	RHOB	DTC	DTS	Po	Pp	Pm	Vcl
1107.18	1107.22	2.093	113.8215	192.8141	3297.147	1799.24	2143.572	0.2459
1111.07	1111.11	2.103	112.0794	187.5476	3324.539	1799.811	2078.336	0.006
1090.07	1090.1	1.9005	117.1058	211.457	2947.631	1789.658	2110.849	0
1095.24	1095.27	2.0794	112.3377	188.1843	3240.396	1797.773	2120.806	0
1099.08	1099.12	2.063	105.9475	187.5763	3226.111	1797.469	2128.191	0
1103.77	1103.81	2.106	103.0164	177.7332	3307.408	1799.142	2136.928	0
1117.67	1117.71	2.1197	102.0535	190.9267	3370.845	1800.574	2163.422	0.1649
1125.47	1125.5	2.2966	100.2789	170.4608	3677.647	1802.467	2178.094	0.188
1123.06	1123.1	2.0492	102.7139	180.7206	3274.448	1802.997	2183.456	0
1133.18	1133.21	1.9704	107.9853	181.6842	3176.904	1804.303	2193.34	0
1135.07	1135.11	2.0174	107.6518	187.0118	3258.108	1803.684	2196.64	0
1136.29	1136.32	1.988	106.6647	186.2863	3214.078	1803.296	2198.936	0
1143.25	1143.29	2.2037	108.8812	188.7932	3584.631	1802.881	2213.285	0.0325
1144.76	1144.8	2.1475	113.0535	191.774	3497.828	1802.467	2213.823	0
1146.36	1146.4	2.1575	106.5889	204.1652	3519.027	1802.997	2209.701	0
1147.65	1147.69	2.1506	107.7616	204.5308	3511.72	1804.303	2219.266	0
1149.55	1149.59	2.232	103.6773	197.414	3650.672	1803.684	2222.611	0
1151.06	1151.1	2.3431	98.9981	186.6261	3837.422	1803.296	2225.626	0.1515
1133.46	1133.51	2.2578	97.9787	181.3472	3641.183	1816.698	2287.455	0.0204
1137.46	1137.51	2.1076	114.4859	202.1381	3410.948	1817.838	2222.461	0.003
1133.65	1133.7	1.9547	109.9285	185.7521	3152.898	1818.242	2224.922	0
1190.16	1190.21	2.2129	97.3308	170.8587	3747.295	1826.102	2227.886	0.0657
1191.25	1191.31	2.2303	96.5207	167.9193	3780.219	1828.798	2306.719	0.1097
1195.26	1195.31	2.1656	98.2881	177.6229	3682.913	1829.252	2310.586	0.01817
1196.15	1196.2	2.1758	102.6351	178.0959	3703.015	1831.731	2312.19	0
1193.47	1193.52	2.4614	86.9743	172.7978	4179.694	1833.296	2317.287	0.2242
1199.16	1199.21	2.1226	103.6278	194.2021	3621.563	1835.399	2311.091	0
1200.36	1200.42	2.1758	98.7428	189.2801	3716.048	1836.226	2320.573	0
1202.56	1202.62	2.1979	98.7174	194.9381	3760.672	1837.714	2324.887	0
1203.65	1203.7	2.2424	98.9398	194.2648	3840.291	1841.066	2326.9	0
1217.06	1217.11	2.2706	92.2556	168.2104	3931.909	1842.709	2353.449	0
1218.61	1218.67	2.2448	94.5858	170.2703	3892.182	1791.371	2210.854	0.069
1270.23	1270.3	2.2834	96.8497	181.1315	4126.817	1793.685	2456.35	0.2333
1139.94	1139.93	2.3455	102.1311	209.1034	3804.243	1957.686	2206.484	0.4747

Table C.2. Used data for calculation of Pc in MATLAB for well 7121/4-F-2 H

TVD	MD	RHOB	DTC	DTS	Po	Pp	Pm	Vcl
2405.24	2499.4	2.3287	80.2383	123.4861	7062.24	3915.932	4375.98	0.4085
2407.11	2501.5	2.3561	75.5367	114.0898	7116.475	3956.992	4383.852	0.4813
2407.92	2502.4	2.3393	77.5805	116.9597	7119.607	3909.924	4385.328	0.4766
2411.32	2506.2	2.3476	78.6333	125.9347	7132.585	3911.983	4391.52	0.5676
2412.83	2507.9	2.3752	75.009	119.5821	7138.295	3914.433	4394.27	0.5231
2415.52	2510.9	2.3304	79.2251	124.0753	7148.791	3915.329	4399.169	0.5233
2419.72	2515.6	2.3497	76.4302	117.8177	7165.325	3925.611	4406.818	0.3001
2423.92	2520.3	2.4217	74.435	113.9978	7181.569	4085.546	4414.467	0.1841
2442.69	2541.3	2.3742	73.3229	118.9752	7254.331	3955.862	4448.651	0.1418
2445.99	2545	2.3807	75.3453	125.3017	7267.295	3961.206	4454.661	0.2968
2446.89	2546	2.3744	75.8659	128.3129	7270.928	3962.664	4456.3	0.2255
2463.55	2564.7	2.366	74.5449	123.0757	7335.243	3989.644	4486.642	0.0302
2527.58	2636.7	2.3991	72.6036	120.2084	7592.277	4086.081	4603.254	0.4051
2569.31	2683.5	2.3833	72.043	116.4525	7760.239	4153.542	4679.253	0.2097
2602.3	2720.3	2.4115	69.4938	111.2603	7893.086	4206.873	4739.334	0.5451
2618.52	2738.4	2.3854	73.3906	115.7933	7956.804	4229.335	4768.874	0.0325
2660.58	2784.9	2.3366	74.8729	118.7841	8124.293	4293.449	4845.475	0.5846
2661.58	2786	2.3239	75.9749	120.1735	8127.851	4295.063	4847.296	0.4725
2662.49	2787	2.3347	73.3191	120.3009	8131.425	4296.531	4848.953	0.5136
2662.95	2787.5	2.3355	72.1412	120.709	8132.953	4297.274	4849.791	0.4495
2663.41	2788	2.3369	73.0873	119.5565	8134.483	4298.016	4850.629	0.4362
2664.32	2789	2.3309	74.6859	119.9355	8138.039	4299.485	4852.286	0.4606
2667.05	2792	2.3528	72.2049	118.962	8148.31	4303.89	4857.258	0.3506
2725.31	2855.7	2.4228	66.5525	103.414	8386.434	4393.993	4963.361	0.408
2726.97	2857.5	2.4376	69.6476	107.9685	8392.816	4396.669	4966.385	0.3755
2727.8	2858.4	2.4181	70.6955	108.3832	8395.99	4398.008	4967.896	0.3492
2728.17	2858.8	2.4216	70.6352	110.2896	8397.575	4398.604	4968.57	0.2859
2728.54	2859.2	2.4153	69.6785	110.8989	8398.631	4399.201	4969.244	0.2854